| | |
|---|---|
| **Titre:**<br>Title: | The Myelin-Weighted Connectome: A Multiplex Approach to Characterize Brain Function and Structure |
| **Auteur:**<br>Author: | Tomi Boshkovski |
| **Date:** | 2021 |
| **Type:** | Mémoire ou thèse / Dissertation or Thesis |
| **Référence:**<br>Citation: | Boshkovski, T. (2021). The Myelin-Weighted Connectome: A Multiplex Approach to Characterize Brain Function and Structure [Thèse de doctorat, Polytechnique Montréal]. PolyPublie. https://publications.polymtl.ca/6324/ |

| | |
|---|---|
| **URL de PolyPublie:**<br>PolyPublie URL: | https://publications.polymtl.ca/6324/ |
| **Directeurs de recherche:**<br>Advisors: | Nikola Stikov |
| **Programme:**<br>Program: | Génie biomédical |

**POLYTECHNIQUE MONTRÉAL**
affiliée à l'Université de Montréal

# The myelin-weighted connectome: A multiplex approach to characterize brain function and structure

**TOMI BOSHKOVSKI**
Institut de génie biomédical

Thèse présentée en vue de l'obtention du diplôme de *Philosophiæ Doctor*

Génie biomédical

Avril 2021

**POLYTECHNIQUE MONTRÉAL**
affiliée à l'Université de Montréal

Cette thèse intitulée :

# The myelin-weighted connectome: A multiplex approach to characterize brain function and structure

présentée par **Tomi BOSHKOVSKI**
en vue de l'obtention du diplôme de *Philosophiæ Doctor*
a été dûment acceptée par le jury d'examen constitué de :

**Julien COHEN-ADAD**, président
**Nikola STIKOV**, membre et directeur de recherche
**Benjamin DE LEENER**, membre
**Alessandro DADUCCI**, membre externe

# DEDICATION

*To Dushko and Dusica…*

# ACKNOWLEDGEMENTS

It has been four years and eight months since I came to Poly and started this journey. Every journey is full with ups and downs, but what is important are the people who walk together with you and make every moment so special and worth remembering. There are not enough words that can help me now, to express my deepest gratitude, appreciation and thank you to all the people that were part of this journey of mine.

First, I would like to thank my PhD advisor Professor Nikola Stikov. He is a mentor that one can wish for. He is an excellent researcher, engineer, and the best teacher. He is always very patient and knows how to get out the best from you. He is a passionate open-science advocate and a well known science communication promoter. Thanks to him, I got involved in open-science and science communication. Also, he made it possible for me to work together with the best scientists in the world. I am eternally grateful for everything that I have learnt from him, for his valuable advice, and for all the opportunities he has provided me.

Then, I would also like to thank the co-director of my lab, Professor Julien Cohen-Adad for always providing me with a continuous scientific and technical support for my project. He is a great researcher, MR engineer, and programmer from whom I have also learnt a lot. Also, thanks to him I got my first-ever MRI scan.

Collaborations are essential to a PhD thesis, and I was very fortunate to collaborate with world class researchers. In particular, I am very thankful to Jennifer Campbell, for sharing her expertise in diffusion MRI and for helping me on the interactive course on diffusion MRI, Matteo Mancini, for all of the valuable discussions and help on my research. I would also like to thank Professor Bratislav Misic, for sharing his expertise in connectomics, Professor Stephane Lehericy, for providing me with data for my research and for his clinical insights on Parkinson's disease, and my master's supervisor Professor Ljupco Kocarev, for the long discussions on graph theory.

I would particularly want to thank my colleagues and very close friends, Agah Karakuzu and Atef Badji. I am deeply indebted to them for always being there for me, listening to my problems, both technical and personal, and making the days in Montreal more memorable. In addition, I would like to thank the rest of the members of NeuroPoly: Tanguy, Gabriel, Harris, Lucas, Ryan, Charley, Dominique, Sara, Angel, Maxime, Anne, Alexa, Nicolas, Christian, Nibardo and Alexandru, for the great discussions and their help.

Moreover, I would also like to express my deepest appreciation to a special person for me,

Steph. I would like to thank her for always being there supporting me, and embracing this project with me. Also, for tolerating me during my low moments.

I wouldn’t have started this journey without the love and support from my family, especially my parents, Zoran and Svetlana. I would love to thank them for all the love, support and the encouragement to pursue my dreams.

Finally, I would like to thank the most important person in my life, my brother ("my son") Dule. You were the reason and my motivation for this journey. I apologize for the past couple of years that I was not always able to physically be there with you, but I know that our bond kept us going, even though we were 7,128 kilometers away from each other.

# RÉSUMÉ

L'intégrité de la myéline joue un rôle important dans la fiabilité de la transmission du signal le long des axones d'un neurone à l'autre. Il existe de nombreuses maladies neurologiques qui affectent la myéline et perturbent la transmission normale du signal, provoquant une grande variété de symptômes différents. Un moyen efficace de modéliser et de mieux comprendre non seulement la pathologie, mais aussi le bon fonctionnement du cerveau, consiste à utiliser la l'étude des connectomes soit la connectomique. La connectomique offre un moyen unique de modéliser le cerveau comme un réseau de régions interconnectées. Il est très courant d'attribuer des pondérations aux connexions qui pourraient représenter une propriété microstructurale sous-jacente. Cependant, les métriques bien établies qui sont utilisées pour pondérer le connectome (comme par exemple les mesures dérivées de la diffusion, l'anisotropie fractionnaire (FA) et le nombre de streamlines) manquent de spécificité. Par conséquent, les connectomes pondérés avec les métriques standard dérivées de la diffusion peuvent ne pas être en mesure de capturer pleinement les changements sous-jacents causés par une pathologie spécifique.

L'objectif principal de cette thèse était de faire progresser le modèle de connectivité cérébrale avec des informations sur la myéline. Pour ce faire, le connectome structurel a été complété par une mesure IRM quantitative sensible à la myéline. Le connectome a été construit à partir du tractogramme reconstruit à partir de données IRM de diffusion multi-shell. Ensuite, en utilisant les informations sur la myéline extraites du taux de relaxation longitudinale (R1), un poids a été attribué à chaque connexion dans le connectome. Afin d'évaluer la valeur ajoutée du connectome pondéré en myéline, il a été comparé à l'un des connectomes standard pondéré avec un certain nombre de streamlines. Il a été observé que le connectome pondéré par la myéline diffère des connectomes standard. Les résultats de la comparaison ont montré que le connectome pondéré par la myéline ne suivait pas la même distribution de degré de nœud (node degree) et présentait une structure modulaire différente. En utilisant une analyse basée sur les rangs, il a été montré que le R1 pouvait mieux séparer les régions responsables des fonctions d'ordre supérieur des régions responsables des fonctions d'ordre inférieur. Cette étude a été publiée dans le journal Network Neuroscience.

Après avoir établi le connectome pondéré en myéline sur des individus sains, il a été utilisé pour étudier les altérations de la teneur en myéline chez les personnes atteintes de la maladie de Parkinson. Afin d'identifier une modification de la teneur en myéline, les connectomes pondérés en myéline des individus atteints de la maladie de Parkinson ont été comparés aux

connectomes pondérés en myéline d'individus sains de même âge. Le résultat de l'analyse a montré que la plupart des connexions identifiées avec l'altération de la teneur en myéline provenaient des noyaux gris centraux, en particulier des noyaux de la Substance noire, considérée comme une région épicentrale de la maladie de Parkinson. De plus, afin d'évaluer la progression de la maladie et identifier d'autres épicentres potentiels de la maladie, nous avons effectué une analyse en anneau (ring analysis) des régions sous-corticales et du tronc cérébral. Cette analyse a montré que la Substance noire, l'Amygdale, l'Hippocampe, le Noyau basal de Meynert et le Mésencéphale étaient des régions qui présentaient une diminution significative de la teneur en myéline le long des connexions qui en émergeaient. Enfin, nous avons identifié un modèle de connectivité multivariée de connexions qui coïncident au maximum avec le score clinique évaluant la motricité. Ce travail a été soumis au journal Movement Disorders.

Enfin, en utilisant le connectome pondéré en myéline, nous avons étudié les altérations de myélinisation de la substance blanche qui est d'apparence normale chez les patients atteints de sclérose en plaques (MS). Pour cela, toutes les connexions qui traversaient ou se terminaient par une lésion ont été écartées de l'analyse. Dans cette étude, le connectome a été pondéré avec la FA comme mesure standard dérivée de la diffusion, et pondéré par le rapport de transfert de magnétisation (MTR) comme mesure sensible à la myéline. En utilisant une analyse statistique multivariée, nous avons pu identifier plus de connexions qui ont montré une diminution de la myéline dans le groupe MS par rapport aux connexions identifiées avec le connectome pondéré en FA. La plupart des connexions affectées identifiées étaient communes pour les deux connectomes, mais environ 1/5 de ces connexions étaient uniques pour le connectome pondéré par la myéline. Ces travaux ont été présentés lors de la 27$^{e}$ réunion annuelle de la Société internationale de résonance magnétique en médecine (ISMRM).

L'impact de ce projet est de renforcer l'importance de l'utilisation du connectome pondéré en myéline pour évaluer différentes maladies neurodégénératives. Le connectome pondéré par la myéline a la capacité d'offrir une information plus complète de la microstructure cérébrale et de sa relation avec la fonction cérébrale. De plus, cela pourrait également conduire au développement de nouveaux biomarqueurs capables de capturer les changements microstructuraux précoces causés par des pathologies qui affectent la teneur en myéline.

# ABSTRACT

Myelin plays an important part in how reliably the signal is transmitted along the axons from one neuron to another. There are many neurological diseases that affect the myelin content and disturb the normal transmission of the signal, therefore cause a wide variety of different symptoms. A convenient way to better understand not just pathology, but also how the brain works, is to use connectomics. Connectomics provides a unique way to model the brain as a network of interconnected regions. It is very common to assign weights to the connections that could represent some underlying microstructural property. However, the well-established metrics which are used to weight the connectome (such as the diffusion-derived measures fractional anisotropy (FA) and number of streamlines), lack specificity. Therefore, the connectomes weighted with the standard diffusion-derived metrics may not be able to fully capture the underlying changes caused by specific pathology.

The main objective of this PhD was to advance the model of brain connectivity with information about myelin. In order to do that, the structural connectome was complemented with a quantitative MRI measure sensitive to myelin. The connectome was built from the tractogram reconstructed using multi-shell diffusion MRI data. Then, using the information about the myelin extracted from the longitudinal relaxation rate (R1) a weight was assigned to each connection in the connectome. In order to evaluate the added value of the myelin-weighted connectome, it was compared to one of the standard connectomes weighed with the number of streamlines. It was observed that the myelin weighted connectome differs from the standard connectomes. The results of the comparison showed that the myelin-weighted connectome did not follow the same node degree distribution and exhibited a different modular structure. Using a rank-based analysis it was shown that R1 could better divide the regions responsible for higher-order functions from the regions responsible for low-order functions. This work was published in the Network Neuroscience journal.

After establishing the myelin-weighted connectome on healthy individuals, it was used to study the alterations of myelin content in individuals with Parkinson's disease. In order to identify alteration in the myelin content, the myelin-weighted connectomes of the Parkinson's disease individuals were compared with the myelin-weighted connectomes of age-matched healthy individuals. The result from the analysis showed that most of the identified connections with alteration of the myelin content were emerging from the basal ganglia, in particular from the Subtantia Nigra, which is considered to be an epicentral region for Parkinson. Additionally, to evaluate the disease progression and identify other potential epicenters of the

disease, we performed a ring analysis of the subcortical and brainstem regions. This analysis showed that the Substantia Nigra, Amygdala, Hippocampus, Nucleus basalis of Meynert, and the Midbrain were the regions that showed a significant decrease of the myelin content along the connections emerging from them. Lastly, we identifed a multivariate connectivity pattern of connections that maximally covary with the motor clinical score. This work was submitted to the journal of Movement Disorders.

Finally, using the myelin-weighted connectome we investigated the alterations of myelin content in the normal appearing white matter in patients with multiple sclerosis (MS). For this, all of the connections passing through or ending in a lesion were discarded from the analysis. In this study, the connectome was weighted with FA as a standard diffusion-derived measure and magnetization transfer ratio (MTR) as a myelin sensitive measure. Using multivariate statistical analysis, we were able to identify more connections that showed decreased myelin in the MS group compared with the connections identified with the FA-weighted connectome. Most of the identified affected connections were common for both connectomes, however approximately 1/5 of these connections were unique for the myelin-weighted connectome. This work was presented at the 27th annual meeting of the International Society for Magnetic Resonance in Medicine (ISMRM).

The impact of this project is to bolster the importance of using the myelin-weighted connectome to evaluate different neurodegenerative diseases. The myelin-weighted connectome has the capacity to offer a more comprehensive understanding of brain microstructure and the white matter myeloarchitecture. Moreover, it could also potentially lead to the development of new biomarkers that can capture the early microstructural changes caused by pathologies that affect the myelin content.

# TABLE OF CONTENTS

# LIST OF TABLES

# LIST OF FIGURES

# LIST OF SYMBOLS AND ACRONYMS

| | |
|---|---|
| AD | Alzheimer’s disease |
| ADC | Apparent diffusion coefficient |
| CSF | Cerebral spinal fluid |
| DWI | Diffusion-weighted imaging |
| DTI | Diffusion tensor imaging |
| EEG | Electroencephalography |
| FA | Fractional anisotropy |
| fMRI | Functional magnetic resonance imaging |
| ihMT | Inhomogeneous magnetization transfer |
| IR | Inversion recovery |
| MD | Mean diffusivity |
| MEG | Magnetoencephalography |
| MP2RAGE | Magnetization Prepared 2 Rapid Acquisition Gradient Echoes |
| MRI | Magnetic resonance imaging |
| MS | Multiple sclerosis |
| MT | Magnetizaton transfer |
| MTR | Magnetization transfer ratio |
| MTsat | Magnetization transfer saturation |
| MWF | Myelin water fraction |
| NODDI | Neurite orientation dispersion and density imaging |
| NOS | Number of streamlines |
| NMR | Nuclear magnetic resonance |
| PD | Parkinson’s disease |
| qMRI | Quantitative magnetic resonance imaging |
| qMT | Quantitative magnetization transfer |
| QSM | Quantitative susceptibility mapping |
| R1 | Longitudinal relaxation rate |
| RF | Radiofrequency |
| SWI | Susceptibility-weighted imaging |
| T1 | Longitudinal relaxation time |
| T2 | Transverse relaxation time |
| TE | Echo time |
| VFA | Variable flip angle |

# LIST OF APPENDICES

# CHAPTER 1 INTRODUCTION

One of the primary motivations for studying the brain is to develop a more comprehensive understanding of how the microstructure gives rise to its function. This task is non-trivial as obtaining *in vivo* information on brain activity is inherently difficult. Vast advances in this endeavor have been made possible through magnetic resonance imaging (MRI). Magnetic resonance imaging, and diffusion MRI in particular, have been shown to be excellent tools for non-invasively probing brain tissue microstructure (Le Bihan et al., 1986).

MRI is particularly useful for the study of neurodegenerative diseases, for which we have yet to understand the underlying causes and the details of disease progression. A lack of knowledge of the fundamental underpinnings of a disease makes it all the more difficult to effectively assess and treat it. Magnetic resonance imaging has already shown great promise in the study of several neurodegenerative diseases, including Alzheimer's disease (AD) (Jack Jr, Bernstein, et al., 2008; Vemuri and Jack, 2010), Parkinson's disease (PD) (Mahlknecht et al., 2010; Stern et al., 1989), and multiple sclerosis (MS)(Hemond and Bakshi, 2018).

The field of connectomics aims to investigate the mechanics of such diseases in the brain by integrating MRI with network theory. The framework for envisioning the brain as a network was first introduced in 2005 (Sporns, Tononi, et al., 2005). In this model neural elements and their interconnected pathways are represented as a collection of nodes and edges, respectively. The nodes and edges of the network are defined via information extracted from MRI analysis. The structural connectome is traditionally reconstructed using diffusion-based tractography. Once the connections have been defined, weights can be added in an effort to more accurately represent the network structure. Standard weights include diffusion metrics such as the number of streamlines (NOS) and fractional anisotropy (FA)(Yeh, Jones, et al., 2020).

While it has become standard practice to use diffusion MRI to establish the structural connectome, this approach is not without its limitations. Indeed, it may be difficult to reliably establish the nodes and edges of a network(Yeh, Jones, et al., 2020). A variety of atlases are available for brain parcellation. Moreover, fiber tracking results may vary with the particular tractography algorithm that is chosen(Jones, 2010a; Yeh, Jones, et al., 2020). The most appropriate choice of connection weight is one of ongoing discussion. The NOS, for example, does not relate to any valid biological metric. While FA is capable of measuring biologically meaningful tissue properties, it lacks specificity. Changes in FA may result from any number of influences, including tissue geometry, fiber density, axonal loss, or demyelination(Jones, Knösche, et al., 2013).

In order to mitigate some of the effects of these limitations, the well-established diffusion-weighted connectome may be improved upon by supplementing it with a measure that is more specific to the underlying tissue microstructure. The myelin surrounding axons is a material that has been implicated in a number of neurodegenerative diseases, including AD, PD, and MS. Hence, employing myelin-sensitive metrics as weights to the connectome may provide an additional source of biologically relevant information when establishing the structural connectome. Therefore, the main objective of this PhD project was to advance the structural connectome with a myelin-sensitive measure and investigate the alterations of the myelin content in Parkinson's disease and multiple sclerosis.

The thesis is organised into 8 chapters. In Chapter 2 we will give a critical review of the literature. First, we will provide details on the brain anatomy, with a focus on the myelin. Then, we will follow with the basic principles of MRI and quantitative MRI for myelin imaging. Next, we will dive into the secrets of diffusion MRI and tractography, and we will finish with a review on the connectomics. Chapter 3 explains the methodology, while Chapters 4, 5, and 6 present the published results to establish the myelin-weighted connectome framework and to study the myelin content alterations in neurodegenerative and neuroinflammatory diseases, Parkinson's disease and Multiple Sclerosis, respectively.

# CHAPTER 2 LITERATURE REVIEW

## 2.1 Brain Anatomy

### 2.1.1 The brain on macroscopic scale

The brain is an amazingly complex organ that controls all functions in our body, processes the information perceived from the outside world, and responds with specific action. On a macroscopic level the brain can be divided into 3 main parts: the cerebrum, cerebellum and the brainstem. The cerebrum and the cerebellum are involved in processing of higher-order functions (movement, speech, hearing, vision, learning, emotions, etc.) (Jawabri and Sharma, 2019; Rapoport et al., 2000), while the brainstem is responsible for automatic functions such as breathing, heart rate, and body temperature. (Basinger and Hogg, 2020).

The cerebrum forms the largest aspect of the brain and can be divided into the left and right hemispheres. It can be further divided into four lobes: frontal, occipital, parietal, and temporal. The frontal lobes are the largest and encompass brain regions that are responsible for a myriad of functions (Stuss and Alexander, 2000). The prefrontal cortex is highly involved in tasks related to memory, behavior, and speech. The primary motor cortex and precentral gyrus are charged with producing movement in various parts of the body (Volkmar and Volkmar, 2013). Eye and head movements, as well as proprioception, are also controlled by the premotor cortex. The occipital lobe can be found on the posterior aspect of the brain. It is primarily responsible for receiving and processing visual information. The integration of somatosensory and visual information is the role of the parietal lobe. The temporal lobe is mainly important for speech and language processing, and memory.

### 2.1.2 Neurons and glial cells

On the cellular (microscopic) level the brain is composed of two types of cells: neurons and glia, each with their own function. Neurons serve as the basic functional component of the brain. The brain is made up of 86 billion interconnected neurons (Azevedo et al., 2009) that work together to perform all required neuronal functions. Each neuron is composed of four different elements: a cell body (also known as soma), dendrites, an axon, and axon terminals (Figure 2.1). The cell nucleus, along with organelles required for cellular function, is located within the cell body and synthesizes all the neural proteins and neurotransmitters that transmit the signal from one neuron to another (Lodish et al., 2000a). Branches, known as dendrites, extend from the cell body. They are covered with dendritic spines that aid in interneuronal communication by receiving signals from other neurons (Lodish et al., 2000b). The axon also protrudes from the cell body and aids in the neuron-to-neuron transmission of information. To ensure fast and reliable communication between neurons, the axons are wrapped in a fatty substance called myelin that acts as an insulator to improve signal conduction. The signal travels down the axon until it reaches the synaptic knob. The signal is then transported across the synapse by neurotransmitters. Along the axons, between two myelin sheaths there are small unmyelinated parts of the axon known as nodes of Ranvier. At this domain are concentrated the voltage-gated ion channels that create an electrical impulse by changing the concentration of the ions in the axon(Lubetzki et al., 2020).

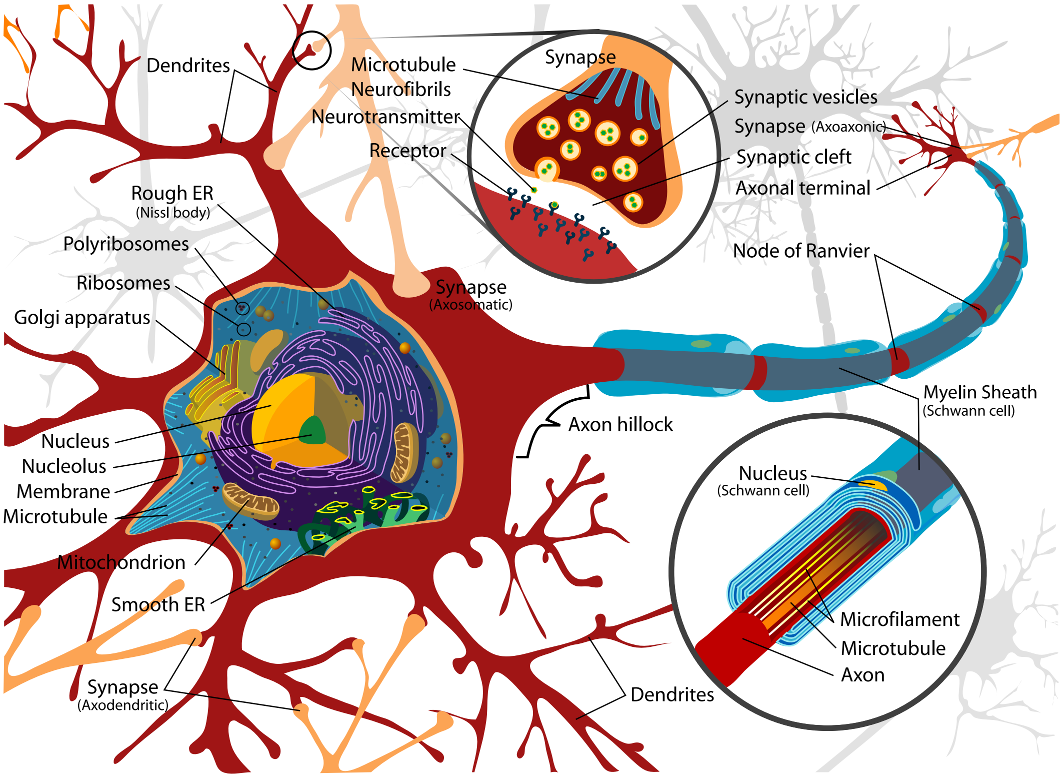

Figure 2.1 Structure of a neuron.

Glial cells are considered non-neuronal cells in that they do not take part in the production or conduction of electrical impulses. Instead, they play a supportive role for neurons by providing nutrition, producing myelin, and maintaining homeostasis. Glial cells are smaller than neurons, but they are far more numerous. They do have processes that extend from the cell body, but these do not include axons or dendrites. While they are not directly involved in signal transmission, they do work to preserve the ionic environment of nerve cells and regulate the rate at which signals propagate. Moreover, they also play a role in modulating neurotransmitter uptake. For example, the oligodendrocytes are glial cells that are responsible for the production of the myelin sheath that wraps around the axons. They are usually connected to tens of axons providing them with myelin insulation (Jäkel and Dimou, 2017).

Grey matter is largely composed of neuronal cell bodies and dendrites, as well as glial cells. White matter, though, primarily consists of the myelinated neuronal axons. All of these components combine to form a vast interconnected network of neural elements on multiple scales. It is no small feat, then, to disentangle the inner workings of the brain. To understand the brain structure and function, different imaging modalities can be employed to create a noninvasive *in vivo* map of the brain. Some of the most commonly used neuroimaging techniques are based on MRI.

## 2.2 Fundamentals of MRI

### 2.2.1 MR Physics

Magnetic resonance imaging is a powerful technique that is used to non-invasively form cross-sectional images of the inside of the body. Compared to other imaging modalities, such as computed tomography (CT), MRI does not have any side effects and provides images with a high level of detail. The basis of MRI as an imaging technique comes from the fundamentals of nuclear magnetic resonance (NMR), which is a technique that probes the magnetic properties of atoms. The NMR phenomenon was concurrently discovered in 1946 by Bloch (Bloch, 1946) and Purcell (Purcell et al., 1946), who were probing the magnetic properties of nuclei by examining their absorption and induction in the presence of an oscillating magnetic field.

NMR focuses on protons, subatomic particles with a mass and positive charge that possess a quantum mechanical property known as spin. Using classical mechanics, one can model protons as magnetic moments that precess around an axis, but we commonly refer to them as spins. Only atoms with an odd number of protons and/or neutrons are characterized by an intrinsic angular momentum (spin) and an intrinsic magnetic moment. The intrinsic magnetic moment $\boldsymbol{\mu}$ is characterized by the charge and mass of the nuclei, as well as its angular momentum (eq. 2.1) (Nishimura, 2010). The ratio between the charge of the nuclei and its mass is characterized by a constant known as the gyromagnetic ratio ($\gamma$):

$$\boldsymbol{\mu} = \frac{q}{2m}\boldsymbol{L} = \gamma\boldsymbol{L} = 2\pi\bar{\gamma}\boldsymbol{L} \tag{2.1}$$

The gyromagnetic ratio is a physical constant of proportionality that is nuclei specific. For example, the gyromagnetic ratio for the $^1H$ nuclei is $\gamma = 2.675 \times 10^8 s^{-1} T^{-1}$ or $\bar{\gamma} = 42.58 \frac{MHz}{T}$ (Brown et al., 2014).

When an ensemble of spins is exposed to an external strong magnetic field ($\boldsymbol{B_0}$) (Figure 2.3a), the magnetic moments of spins tend to align with the direction of the external magnetic field (Nishimura, 2010). There are two possible orientations that the spins may take when exposed to an external magnetic field $\boldsymbol{B_0}$: parallel and antiparallel. The spins' magnetic moments couple with the external magnetic field, producing a torque on the spins that causes them to precess at an angle $\phi$ around $\boldsymbol{B_0}$ (Brown et al., 2014). The frequency of precession is known as the Larmor frequency and is given by:

$$\omega_0 = \gamma B_0 \tag{2.2}$$

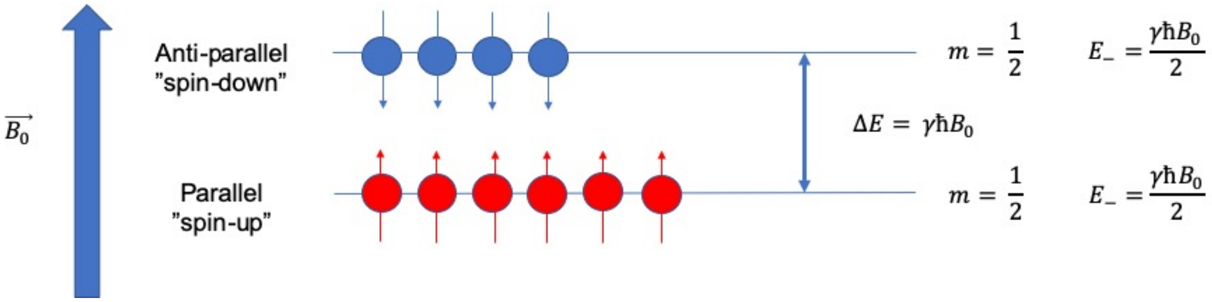

Figure 2.2 Energy levels of the half-integer spins in an external magnetic field ($\boldsymbol{B_0}$). When the external magnetic field B0 is switched on the spins of the specific medium that is being imaged are aligning with the magnetic field. The balls colored red are in the same direction with B0 (aligned parallel), while the blue colored balls are aligned antiparallel with B0. The energy difference between the parallel and antiparallel states is proportional with the magnitude of the main magnetic field.

An excess number of spins will be oriented in the same direction as the $\boldsymbol{B_0}$ because the parallel energy level is more stable (Figure 2.2). Therefore, these excess spins will define the net nuclear magnetization, which is the vector sum of all nuclear spin contributions per unit volume (Nishimura, 2010), i.e., the total magnetic dipole per unit volume:

$$\boldsymbol{M} = \frac{1}{V} \sum \boldsymbol{\mu} \tag{2.3}$$

For an ensemble of N spins per unit volume, in a static magnetic filed $\boldsymbol{B_0}$, the net magnetization at equilibrium is given with the equation

$$\boldsymbol{M_0} = \frac{N\gamma^2\hbar^2 s(s+1)}{3kT}\boldsymbol{B_0} \tag{2.4}$$

where $\hbar$ is the reduced Planck constant ($\hbar = \frac{h}{2\pi}$), s is the spin quantum number, k is the Boltzmann constant and T is the temperature. In NMR we are most interested in components with a half-integer spin (ex. $\pm\frac{1}{2}, \pm\frac{3}{2}, \pm\frac{5}{2}$ etc.). The nuclei with half-integer spins that NMR focuses on are: $^{1}H, ^{13}C, ^{23}Na$, and $^{31}P$.

As it is very hard to measure the magnetization of the spins when they are in the longitudinal (z) plane, we need to tip (or rotate) the magnetization into the transverse (x-y) plane to measure it. To do this, an external time-varying radiofrequency (RF) field ($\boldsymbol{B_1}$) is applied perpendicular to $\boldsymbol{B_0}$, tuned to the precession frequency of the spins. Because this RF field is tuned to the Larmor frequency of the spins, some of the spins will absorb the energy and will start precessing around $\boldsymbol{B_0}$. The magnetization vector will be offset from the z-axis at an angle proportional to the amplitude of $\boldsymbol{B_1}$ (Brown et al., 2014). This angle is known as the flip angle.

The interaction between the net magnetization and the magnetic field can be best explained using the Bloch equation(Bloch, 1946):

$$\frac{d\boldsymbol{M}}{dt} = \boldsymbol{M} \times \gamma\boldsymbol{B} - \frac{M_0 - M_z}{T_1} - \frac{M_{xy}}{T_2} \tag{2.5}$$

where $\boldsymbol{B}$ is the total magnetic field ($\boldsymbol{B} = \boldsymbol{B_0} + \boldsymbol{B_1}$), $M_0$ is the magnetization at equilibrium, $M_z$ is the magnetization that is parallel with the main magnetic field $\boldsymbol{B_0}$ (also known as longitudinal magnetization), $M_{xy}$ is the magnetization that is perpendicular to $\boldsymbol{B_0}$ (also know as transverse magnetization), $T1$ and $T2$ are constants that are specific to the object. The first part of equation 2.5 ($\boldsymbol{M} \times \gamma\boldsymbol{B}$) describes the precession of the magnetization around the main magnetic field, $\boldsymbol{B_0}$, also known as the torque of the magnetization. The second part of the equation describes the process known as relaxation (Hore, 2015). This process starts when the RF field is switched off. As the RF field is not perturbing the main magnetic field anymore, the spins start to return to their equilibrium state once the RF field has been removed. There are two mechanisms contributing to relaxation: transitions between energy levels (longitudinal (T1) or "spin-lattice" (Brown et al., 2014; Hore, 2015; Nishimura, 2010) relaxation) and loss of phase coherence (dephasing) of the magnetization in the trans-

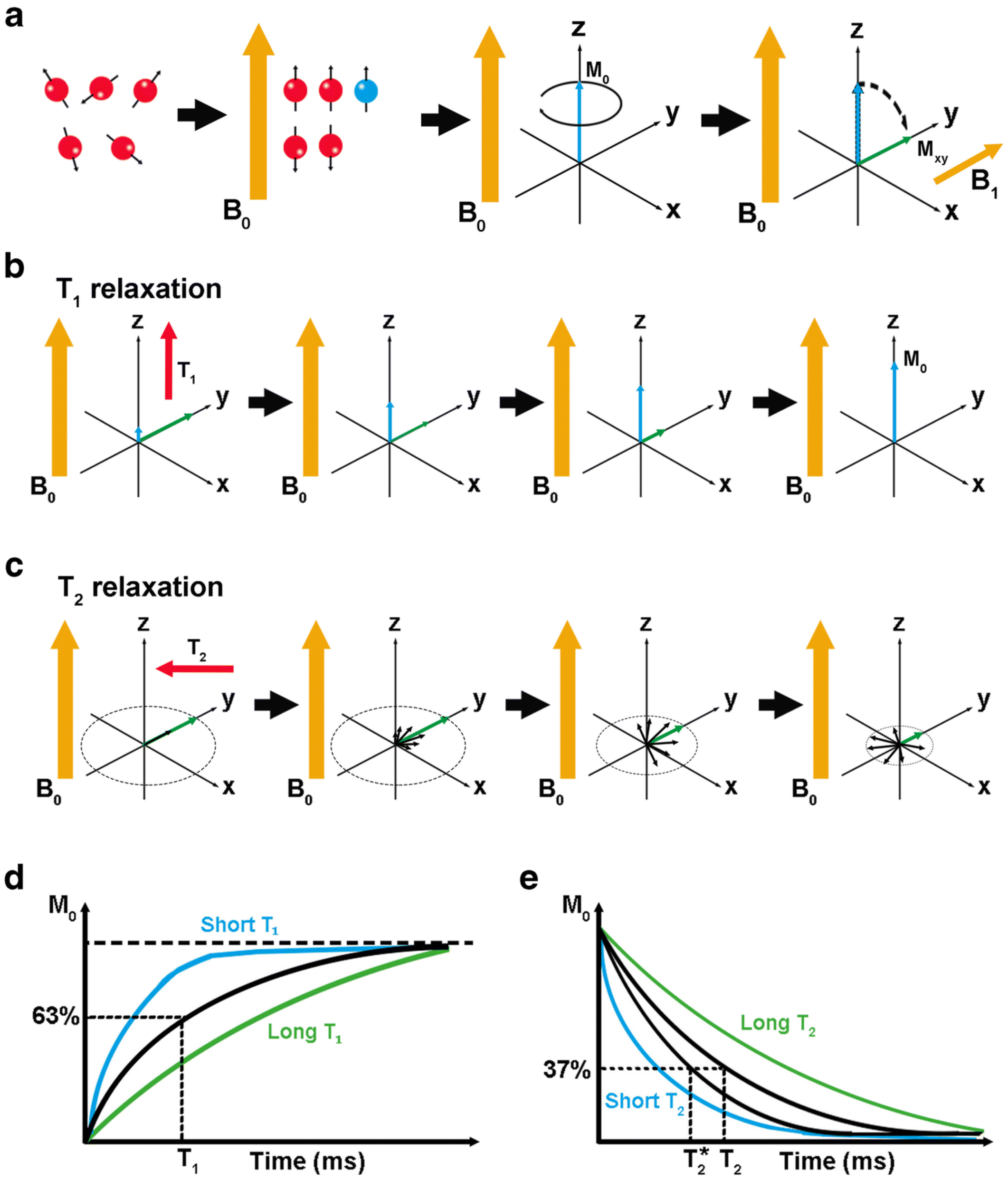

Figure 2.3 The basic principles of MRI. a) The process of excitation or alignment of the spins due to the presence of an external magnetic field $\boldsymbol{B_0}$ as well as the process of excitation due to radiofrequency (RF) pulse $\boldsymbol{B_0}$ that tips the magnetization (green arrow) to the x-y plane. b) and c) Represent the process of relaxation, i.e., the return of the magnetization to the z axis. This process begins when the $\boldsymbol{B_1}$ field is switched off. d) and e) Graphs of the T1 and T2 relaxations over time. At time t=T1, the net magnetization reaches 63% of the initial magnetization M0, while at time t=T2 the transverse magnetization dephases to 37% of the initial magnetization $\boldsymbol{M_0}$. The green and blue exponential curves represent tissues with long T1 and T2 and short T1 and T2 respectively. Reprinted from (Mastrogiacomo et al., 2019)

.

verse (xy) plane (transverse (T2) or "spin-spin" relaxation (Brown et al., 2014; Hore, 2015; Nishimura, 2010)).

Both relaxation mechanisms contribute to the return of the magnetization to the equilibrium state. This process of relaxation forms the basis of all MRI, from structural modalities such as T1- or T2-weighted imaging to more quantitative modalities such as diffusion-weighted imaging.

## 2.3 Myelin imaging

MRI can provide insight into myelin production, damage, and repair. Historically, efforts to directly image myelin have been largely unsuccessful. This is due to the fact that the MR signal of nonaqueous protons in myelin decays to zero before it can be registered. Early attempts to directly image myelin *in vivo* included ultrashort echo time (TE) imaging (Waldman et al., 2003) and $^{31}$P spectroscopy (Kilby et al., 1991). One shortcoming of ultrashort TE imaging is that it is difficult to extract the contaminating signal from water. $^{31}$P spectroscopy suffered from issues related to the quantitative signal characterization from phosphatidylcholine head groups. As a result, most current imaging techniques that aim to investigate the properties of myelin do so indirectly.

### 2.3.1 Myelin water fraction

An alternative technique for imaging myelin content is the myelin water fraction (MWF). This method utilizes the T2w image contrast to detect the presence of myelin within tissue. T2 relaxation is characterized by the exchange of protons and molecules. Since the lipid bilayer in myelin limits the movement of protons because of its hydrophobic properties (Barkovich, 2000; Miot-Noirault et al., 1997), lower intensity values in T2w images indicate that larger myelin content is present. MWF exploits this by focusing on the water contained within the myelin sheath, which has a much shorter T2 relaxation time compared with the water in other neural tissue. This difference in T2 relaxation times can be exploited to determine the MWF (Mackay et al., 1994). Since the myelin water is expected to comprise 40% of the myelin volume fraction, MWF can be used to infer information regarding myelin content across the brain or within a given tissue of interest (Lee, Hyun, et al., 2020). Improvements to this method have been proposed in order to improve image quality to make it more amenable for clinical use (Prasloski et al., 2012).

### 2.3.2 Magnetization transfer imaging

The most commonly used MR technique for assessing myelin content *in vivo* is magnetization transfer (MT) imaging. The simplest form of this method is based on the two-pool model of protons. The primary source of the proton MR signal is free water protons. These protons are very mobile and are able to move rapidly. The freedom of motion enables these protons to have T2 relaxation times greater than 10ms, which is long enough for spatial encoding gradients to be applied between excitation and acquisition of the signal before it fully decays. The collection of these protons is referred to as the free water pool. In contrast, protons associated with the macromolecules and membranes in tissues are much more restricted in their movements. As a result, these protons are characterized by very short T2 relaxation times (less than 1ms) and therefore cannot be measured directly by conventional MRI techniques (Henkelman, Stanisz, et al., 2001). This group of protons is known as the bound pool. As proton exchange occurs between the free and bound pools, it is possible for the spin state of the macromolecular protons to influence the spin state of the free water protons. This phenomenon can be manipulated to generate a specific MR contrast that can be used to extract information about the myelin content in tissue. The bound macromolecular protons can be targeted specifically by saturating them with an off-resonance RF pulse. Since these spins have a much broader lineshape than those of free water protons, they are much more sensitive to off-resonance irradiation (Henkelman, Stanisz, et al., 2001). The aforementioned proton exchange between the free and bound pools enables the saturation of the macromolecular spins to be transferred to the free water spins, where it can then be measured as MRI signal. The most common method for quantifying the magnitude of the MT effect is the magnetization transfer ratio (MTR). This is achieved by acquiring one set of images with an MT pulse and one set without. The MTR is then defined per voxel as follows:

$$MTR = \frac{S_0 - S_{MT}}{S_0} \tag{2.6}$$

where $S_0$ represents the magnitude of tissue signal without an MT pulse and $S_{MT}$ is the magnitude of tissue signal after the application of an MT pulse. While MTR has been shown to correlate with myelin content (Schmierer, Scaravilli, et al., 2004), it is also known to be affected by variations in T1 and B1 (Schmierer, Scaravilli, et al., 2004). Thus, magnetization transfer saturation (MTsat) was introduced to correct for both of these effects (Helms et al., 2008). Despite these improvements, MTsat still depends on the particular protocol used and therefore will always require calibration.

To estimate MT measures that are independent of protocols and scanners, multiple MT images must be acquired for a range of RF amplitudes and off-resonance frequencies. This technique, known as quantitative magnetization transfer (qMT), aims to sensitize MT images to various parts of the macromolucular spectrum (Henkelman, Huang, et al., 1993). The measurements obtained from these images can then be fitted to a model to estimate metrics such as the ratio of the relative size of the bound pool to the free pool, the relaxation parameters of the bound and free pool, as well as the exchange rate between the pools. One drawback of this technique is the long acquisition times that are required to obtain enough measurements to accurately fit the models (Heath et al., 2018). Efforts to mitigate this issue have been proposed by developing simpler models that require fewer measurements to be acquired (Yarnykh, 2012).

One final MT technique to consider is inhomogeneous magetization transfer (ihMT), which aims to improve the specificity to myelin when compared with conventional MT acquisitions (Varma et al., 2015). Typical MT effects that result from the transfer of protons between at least one pool of magnetization is characterized by a broad dipolar line shape. This line represents the summation of multiple individual lines that have different offset frequencies. It is difficult to differentiate between the spin components of these lines using RF excitation or saturation because they oscillate rapidly between frequencies. Nonetheless, conventional MT modeling assumes that the lines undergo this rapid exchange, and they are referred to as homogeneously broadened lines. Magnetization in large membranes, such as the myelin sheath, however, is considered to be inhomogeneously broadened because the lipids and proteins of the membrane lack the freedom of movement required for homogeneous broadening. By targeting the exchange of inhomogeneously broadened magnetization within the homogeneous broadening of traditional MT, it is possible to acquire a signal that is much more specific to myelin content (Mchinda et al., 2018).

### 2.3.3 Quantitative susceptibility mapping

The local MR signal is also impacted by the magnetic susceptibility of a given tissue. Spins located near a tissue or material with paramagnetic properties will precess at a frequency that is slightly higher than that of the main magnetic field. Conversely, spins that are next to a diamagnetic tissue or material will precess at a slightly lower frequency (Heath et al., 2018). This will result in different phase accumulations for tissues with different susceptibility values. T2$^*$, also known as the effective T2, is largely the result of inhomogeneities that are present within the main magnetic field. Such inhomogeneities include intrinsic defects of the magnet or susceptibility-induced distortions that result from tissue or other materials. Therefore, the $T2^*$-weighted signal is used to highlight these shifts in local magnetic fields. Susceptibility weighted imaging (SWI) can be employed to augment the contrast of different susceptibility values between tissues by incorporating and filtering both phase and magnitude information. The resultant SW images provide information regarding the relative differences in susceptibility values between tissues. The aim of quantitative susceptibility mapping (QSM), however, is to obtain quantitative measures of the susceptibility shifts of tissues. Myelin has been shown to have diamagnetic properties and is thought to be the largest component of white matter. Myelin susceptibility is thus thought to be the dominant source of $T2^*$ contrast in white matter (Li, Yao, et al., 2009). As such, several studies have demonstrated the usefulness of susceptibility as a marker for white matter in the brain (Argyridis et al., 2014; Li, Wu, et al., 2014; Lodygensky et al., 2012).

### 2.3.4 T1 relaxation

Some of the earliest attempts at evaluating the spatial distribution of myelin in the brain made use of tissue relaxation times (Crooks et al., 1987). These techniques rely on the fact that these relaxation times are directly related to changes between the interactions of free water molecules with the macromolecules composing tissues. A myelin-related contrast can be obtained from T1 maps by taking advantage of the fact that the degree of brightness of white matter in these maps is linked to the spatial distribution of myelin-bound phospholipids (Dobbing and Sands, 1973; Koenig, 1991). While multiple methods exist for generating T1 maps, inversion recovery is considered the gold standard. In this approach, a series of T1w images are acquired for different inversion times. T1 values are then estimated by fitting an exponential growth curve to the data. The quantitative nature of the resultant T1 maps allows for the identification of a more substantial relationship between signal changes and the underlying tissue microstructure. Multiple studies have used T1 mapping techniques to demonstrate a correlation between T1 and myelin. T1 was shown to be associated with myelin content in a study focusing on the characterization of cortical lesions in MS (Tardif et al., 2011). Schmierer et al. (Schmierer, Wheeler-Kingshott, et al., 2008) found that T1 showed a strong correlation with myelin content in unfixed postmortem brain of patients with MS. T1 was also identified as a marker for myelin content in a study of focal epilepsy comparing normal to pathological resections of the neocortex (Reeves et al., 2016). It should be noted that T1 may be biased by axon diameter (Harkins et al., 2016). In fact, studies have shown that the relaxation rate 1/T1 correlates with axon size both *ex vivo* and *in vivo* (Harkins et al., 2016). While each of the aforementioned studies make use of different MRI metrics to indirectly measure the myelin content, a recent meta-analysis study investigating the relationship between different MRI myelin-sensitive metrics and underlying histology found that the MRI-based myelin sensitive metrics are comparable in terms of their relationship with histology as a ground truth (Mancini, Karakuzu, et al., 2020). For example, the study shows that there is not a significant difference between the MTR and T1 (zscore=0.47, p-value=1).

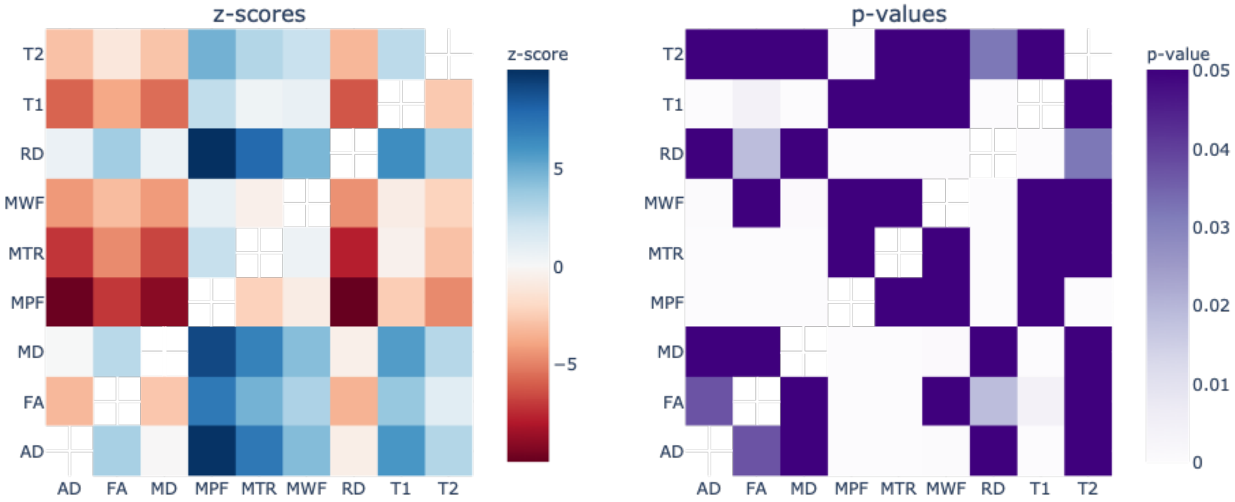

Figure 2.4 . Results from the repeated measures meta-regression published in Mancini et al., 2020 (Mancini, Karakuzu, et al., 2020). The heatmaps represent the results (left: z-scores; right: p-values) of all the pairwise comparisons for MRI-based myelin measures reported in the systematic review, using the coefficient of determination (R2) between MRI and histology as the metric of interest. Interestingly, MTR and T1 are not statistically different (z-score=0.47; p-value=1).

## 2.4 Diffusion MRI

Almost two centuries ago, botanist Robert Brown was following one of his research routines, observing the pollen grains in water under a microscope. After repeating this over and over again, he was fascinated by the movement of the pollen grains. He was struck by the thought that their movements may be dependent on the medium in which they resided. Using different substances, he drew the conclusion that the random motion of the pollen was somehow related to life. Although this realization was raised by Brown, hence the term Brownian motion, he was not able to describe the physics underlying it. Decades later, this issue was addressed by two brilliant scientists, Adolf Fick (Fick, 1995) and Albert Einstein (Einstein, 1956). Today, we have two main classes for diffusion: i) self-diffusion and ii) chemical diffusion. The first one refers to the spontaneous mixing of the particles in the absence of a concentration gradient, whereas the latter one defines the motion of the particles in the presence of a medium with varying concentration levels. Using specialized MRI techniques, motion of the self-diffusing water molecules can be sensitized to the MRI gradients, which makes the self-diffusion of crucial significance in this context. The following section moves on to explain the physics behind this phenomenon. The effect of the water molecule motion on the MRI signal was recognized by Hahn (Hahn, 1950) in 1950, and by Carr and Purcell (Carr and Purcell, 1954) in 1954. Two years later, in 1956, Torrey incorporated this effect into the Bloch equation, creating the Bloch-Torrey Equation (Torrey, 1956):

$$\frac{\partial \mathbf{M}}{\partial t} = \gamma(\mathbf{M} \times B_0) + \frac{M_x}{T_2} + \frac{M_y}{T_2} + \frac{M_0 - M_z}{T_1} + D\nabla^2 M \tag{2.7}$$

The first part, i.e., the first 4 elements of the equation, is the well known Bloch equation (eq. 2.5) that we have discussed in section 2.2, while the second part describes the diffusion effect, where D is the diffusion coefficient.

The Brownian motion can be mathematically described as a stochastic process (Einstein, 1956). The key component in the description is the conditional probability $P(r|r', t)$, stating that the particles at position $r$ at time zero will move to another position $r'$ after some time t according to:

$$\frac{\partial P(r \mid r', t)}{\partial t} = D\nabla^2 \partial P(r|r', t) \tag{2.8}$$

where $\nabla$ (gradient) operates only on the $r'$.

Given the initial condition $P(r|r', 0) = \delta(r' - r)$, the solution of Eq. 2.8 is a Gaussian distribution

$$\partial P(r|r', t) = (4\pi Dt)^{-\frac{3}{2}} \exp \frac{(r' - r)^2}{4Dt} \tag{2.9}$$

The expression Eq. 2.9 is also known as a Gaussian propagator. The mean displacement that the particle will accumulate is zero. However, when the mean squared displacement of the particle is considered, the equation is expressed as:

$$< (r' - r)^2 >= 6Dt \tag{2.10}$$

The larger the diffusion coefficient $D$, the greater the distance the Brownian particle will travel on average during the same diffusion time.

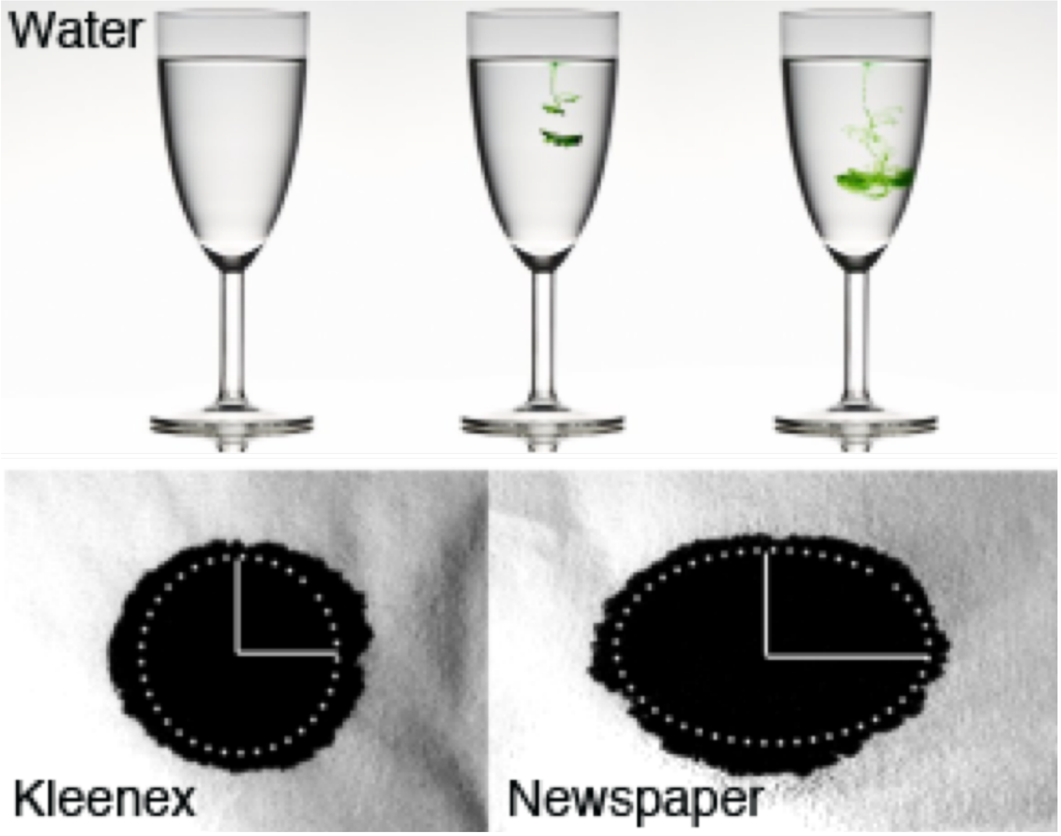

Figure 2.5 Diffusion of ink in different mediums. The diffusion of the ink molecules in water and kleenex is not restricted, meaning that the ink molecules can go in any direction with equal probability. On the other hand the diffusion of the ink molecules on a newspaper is restricted by the microfibers of the newspaper, and therefore the molecules will have a preferential direction of diffusion parallel to the microfibers. Image reproduced from ISMRM blog (Duval et al., 2016)

In regularly arranged bodily structures, such as the axons in the white matter, water molecules diffuse faster along the long axis of those structures, and diffuse more slowly along the orthogonal direction due to the presence of structural obstacles, such as myelin for axons and extracellular collagenous tissue for muscle fibers. Diffusion is described as isotropic if the probability of a particle to diffuse in any direction is the same. However, in the presence of obstacles, this movement is restricted in a preferential direction, resulting in anisotropic diffusion. In the context of Eq. 2.10, an isotropic case can be described by D in any direction $r$, whereas under anisotropic conditions, D depends on the direction of $r$. All of these diffusive properties of particles can be exploited to extract quantitative measures from diffusion MRI.

### 2.4.1 MRI pulse sequences for imaging diffusion

The very first MR-based application of sensitizing the diffusion of water molecules in tissue was carried out by Stejskal and Tanner in 1965 (Stejskal and Tanner, 1965). This was enabled by a smart modification of Hahn's standard spin echo sequence (Hahn, 1950). In addition to excitation and refocusing RF pulses, two magnetic field gradients were placed before and after the refocusing pulse (Figure 2.6). Note that each time a magnetic field gradient is applied, a phase dispersion is induced on the spins, which has a location dependent differential impact among the spins (Figure 2.6). This is the reason behind the application of the first gradient, to induce a controlled phase dispersion. The role of the second gradient, on the other hand, was to remove this intentionally induced phase dispersion. This means that if there are not any other factors influencing the signal, alternating the distance between these gradients would not cause any changes in the echo signal. However, in practice, the diffusion effect manifests itself in this interval and causes a decay in the signal, as previously described by Hahn in 1953. In their Single Pulsed-Field Gradient (s-PFG) Spin Echo sequence, Stejskal and Tanner (Stejskal and Tanner, 1965) explained the relation between the signal loss and the sequence parameters, enabling the practical application of diffusion imaging.

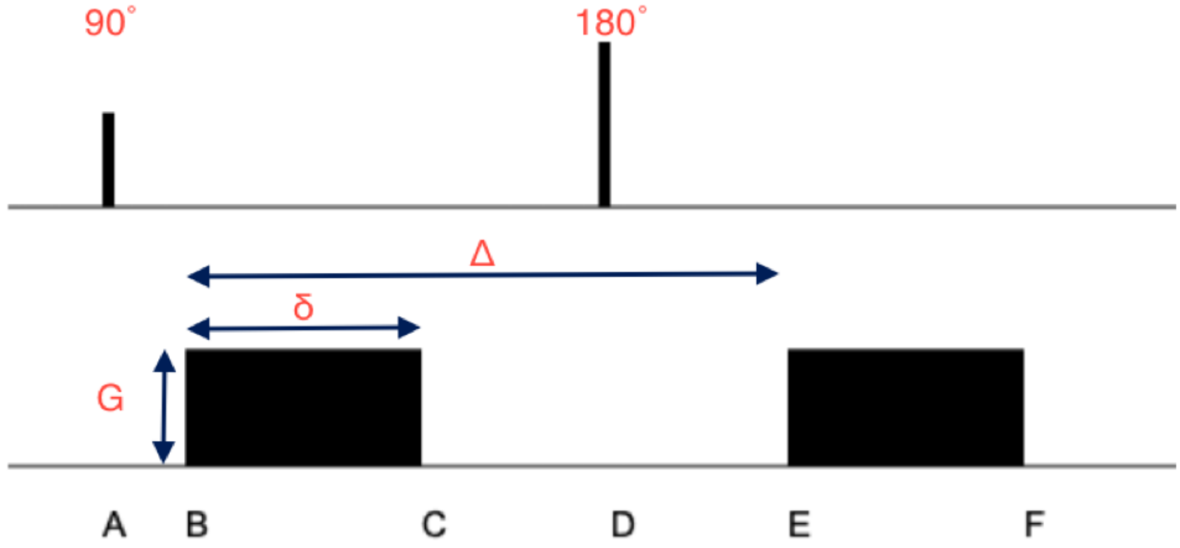

Figure 2.6 Timeline for encoding the diffusion of the water molecules in MRI. Just after being excited, the position of each molecule is tagged based on the phase of its spins, by applying gradient #A (parameterized by its strength $G$ and duration $\delta$). During a time $\Delta$, the spins move (due to Brownian motion or convection). The longer the time $\Delta$ is, the further the molecules can move. A second and identical gradient is applied to quantify this displacement through a signal loss in the MR response.

Upon the application of the first gradient (second line, first block, Figure 2.6), spins dephase according to the encoding length defined by:

$$\lambda^{-1} = q = \gamma g \delta \tag{2.11}$$

where $\gamma$ is the gyromagnetic ratio, g is the gradient amplitude and $\delta$ is the duration of the gradient. During the time $\Delta$ (Figure 2.6), the spins will diffuse with a diffusion length of $l_d = \sqrt{2D\Delta}$, where D is the diffusion coefficient. After the application of a 180° RF pulse, the spins will refocus. While the second gradient will cancel out the dephasing induced by the first gradient, a complete rephasing will be prevented by additional attenuation due to diffusion driven spin drifts. The eventual echo signal is actually an average of an ensemble in which each phase term is weighted by the probability for the spin to start at position $r_0$ and to move to the position r, which is defined by:

$$E(q,\tau) = \frac{S(q,\Delta)}{S(0,\Delta)} = \int P(r) \int P(r|r_0 \exp -q(r - r_0) dr dr_0 \tag{2.12}$$

The echo signal is normalized to $E(0,\Delta)$ to remove the attenuation of the signal due to the $T_2$ relaxation. The solution for the signal equation is:

$$E(q,\tau) = \exp -q^2(\Delta - \frac{\delta}{3})D = \exp -(\gamma g \delta)^2(\Delta - \frac{\delta}{3})D = \exp -bD \tag{2.13}$$

where $b = q^2(\Delta - \frac{\delta}{3})$ is the function of diffusion weighting gradients, also known as b-value (Le Bihan et al., 1986).

By changing the parameters of diffusion weighting (the gradient direction, strength, the diffusion time and the duration of the gradients), one can achieve different contrasts. This contrast mechanism is different than conventional relaxation-weighted MRI. Instead of a sole dependence on the relaxation mechanism, image maps reflect the weighting of diffusion (diffusion-weighted images) (Campbell and Pike, 2019). For example, increasing the diffusion time $\Delta$ allows the spins to diffuse more, which in turn increases the attenuation of the signal. A similar effect can be also achieved by increasing the gradient strength. Manipulating the parameters in this way makes it possible to generate a diffusion-weighted signal that can then be analyzed with the aim of depicting the most likely pathways for the diffusion of particles in the imaged object.

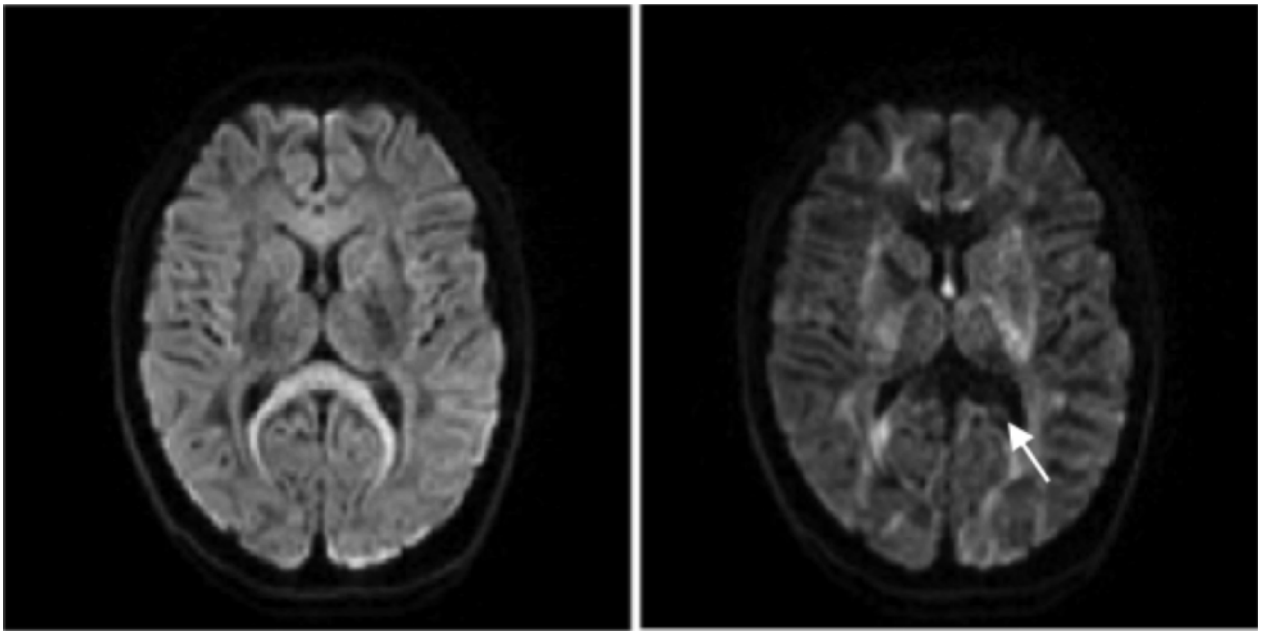

Figure 2.7 DWI obtained with different gradient directions. Axial DW image obtained using gradient only along the z axis (image left) and only along the x axis (image right). The signal drops when the direction of the water molecules is parallel with the gradient direction (hypointensisty in the splenium of corpus callosum, image right). On the other hand the signal increases when the direction of the diffusion of the water molecules is perpendicular to the gradient direction (hyperintensity in the corpus callosum image left). Image reproduced from ISMRM blog.

### 2.4.2 Diffusion modeling

To extract useful microstructural information from the signal obtained from a diffusion-weighted sequence, diffusion models are often necessary (Jelescu and Budde, 2017). Diffusion-weighted imaging is a powerful tool for probing tissue microstructure because the diffusion length, or time required for water molecules to diffuse $5-50\mu m$, is on the same order as the microstructural features of interest ($1-10\mu m$), though this probing is largely indirect due to the featureless character of the signal.

In an effort to address this issue, a range of different diffusion models have been proposed (Jelescu and Budde, 2017; Novikov et al., 2018), which are often divided into two primary classes: signal representation models and biophysical tissue models. The use of one type of model over the other depends upon the characteristics of the model, as well as the data to which the model is being applied. Signal representation models, or statistical models, aim to characterize the signal decay by fitting a continuous function to the diffusion-weighted data. A number of functions have been employed to represent the signal for diffusion analysis, with the cumulant expansion being one of the simplest, and most popular options (Jensen et al., 2005; Kiselev, 2010; Van Kampen, 2007). It can be expressed as a Taylor series as follows:

$$ln\frac{S}{S_0} = -b\mathbf{D} + \frac{1}{6}b^2\mathbf{D}^2\mathbf{K} + ... \tag{2.14}$$

where $b$ is the b-value, $D$ is the diffusivity, and $K$ is the kurtosis. Diffusion tensor imaging (DTI) (Basser, Mattiello, et al., 1994a), for example, can be used to model the signal by considering only the first order term of Eq. 2.14. The minimal amount of data required for this model is a single b-value (single shell) and 6 diffusion directions.

Thus far, physical representation of the diffusion and its measurement using MRI as a voxel-wise representation of the diffusion coefficient D has been mentioned. In clinical practice, this parameter is often replaced with the apparent diffusion coefficient (ADC) that considers diffusion and pseudo-diffusion processes to make an image free from T1 and $T2^*$ weightings (Jones, 2010b). In ADC imaging the signal decay due to the application of the pulse gradient is more directly ascribed to the amount of diffusion:

$$S(q,\tau) = e^{-\tau q^2 D} = \exp -bD \tag{2.15}$$

where D is the diffusion coefficient.

To model the diffusion properties of biological tissues, Basser et al. (Basser, Mattiello, et al., 1994b) proposed the use of a second order symmetric positive-definite tensor. The diffusion propagator in a homogeneous anisotropic environment can be well described by a Gaussian probability distribution function (Mori, 2007), establishing the DT model as follows:

$$P(r|r_0,t) = (4\pi t|\mathbf{D}|)^{-\frac{3}{2}} e^{-\frac{1}{4t}(r-r_0)^T\mathbf{D}^{-1}(r-r_0)} \tag{2.16}$$

where $|\mathbf{D}|$ is the determinant of the diffusion tensor $\mathbf{D}$. The diffusion tensor is a 3x3 symmetrical matrix characterizing the diffusion in three-dimensional (3D) space, represented as:

$$\mathbf{D} = \begin{pmatrix} D_{xx} & D_{xy} & D_{xz} \\ D_{yx} & D_{yy} & D_{yz} \\ D_{zx} & D_{zy} & D_{zz} \end{pmatrix}$$

where each element of the tensor corresponds to the diffusion coefficient obtained using gradients in multiple directions. Since $\mathbf{D}$ is symmetric, only 6 different diffusion coefficients are sufficient to reconstruct a tensor along with one non-weighted acquisition (b0 image)

(Basser, Mattiello, et al., 1994b):

$$\frac{S_i}{S_0} = e^{-\gamma^2 g^2 \delta^2 (\Delta - \frac{\delta}{3})\boldsymbol{D}} = e^{-b\boldsymbol{g}^T\boldsymbol{D}\boldsymbol{g}} \tag{2.17}$$

By using eigen analysis, one can compute the eigenvalues ($\lambda_1, \lambda_2, \lambda_3$) and eigenvectors ($e_1, e_2, e_3$). Different combinations of these outputs provide several scalar measures that, to some extent, characterize the tissue microstructure integrity. The diffusion tensor can be represented by an ellipsoid in 3D space determined by the eigenvector and eigenvalues of the tensor (Figure 2.8).

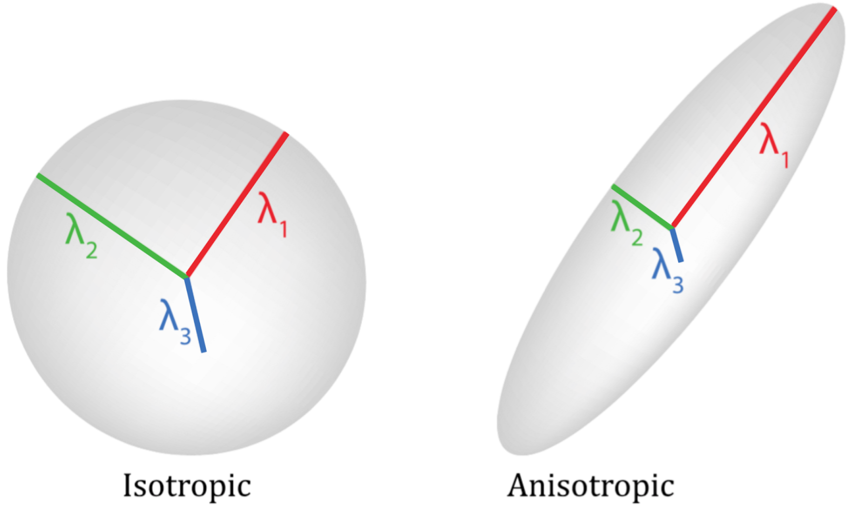

Figure 2.8 Representation of the 3D tensor in space. When the diffusion is isotropic it can be represented with a sphere in the 3D space, while, when the diffusion is anisotropic, then the diffusion is represented as an ellipsoid. Reprinted from (Tromp, n.d.).

Summation of the three eigenvalues produces the trace, which can be averaged to obtain mean diffusivity (MD). This scalar index appears low in the white and gray matter, whereas it increases in the regions where diffusion is less restricted, such as ventricles. Therefore, this measure is well-suited for applications such as the delineation of the regions affected by stroke as demonstrated by (van Gelderen et al., 1994):

$$MD = \frac{\lambda_1 + \lambda_2 + \lambda_3}{3} \tag{2.18}$$

One of the most commonly used scalar diffusion metrics is fractional anisotropy (FA). FA is defined as in Eq. 2.19 and ranges from 0 to 1, specifying what fraction of the diffusion directionality is restricted within a voxel. The FA is often considered as a metric that reflects the microstructural integrity (Jones, Knösche, et al., 2013), though this is still under debate. Many diffusion-based studies have reported that the FA is sensitive to the degree of myelination (Laule et al., 2007). However, it has to be noted here that in addition to myelin, the FA is influenced by multiple tissue properties, such as the axonal loss, the axon diameter, and the fiber packing (Jones, Knösche, et al., 2013). Other popular scalar measures derived from the diffusion tensor are the axial diffusivity (Eq. 2.20), which describes the diffusion parallel to the fibers, and radial diffusivity (Eq. 2.21, which describes the diffusion perpendicular to the fibers.

$$FA = \frac{\sqrt{(\lambda_1 - \lambda_2)^2 + (\lambda_2 - \lambda_3)^2 + (\lambda_3 - \lambda_1)^2}}{\sqrt{2(\lambda_1^2 + \lambda_2^2 + \lambda_3^2)}} \tag{2.19}$$

$$AD = \lambda_1 \tag{2.20}$$

$$RD = \frac{\lambda_2 + \lambda_3}{2} \tag{2.21}$$

A signal representation model is very generalizable as it makes no assumptions regarding the nature of the underlying tissue microstructure (Jelescu and Budde, 2017; Novikov et al., 2018). As a result, it is capable of providing sensitive biomarkers for many different types of tissue. While this type of model has been shown to be adept at detecting changes in tissue diffusivity, it is limited by a lack of specificity. The absence of assumptions regarding any particular type of microstructural element provides wide applicability in terms of use but makes it difficult to attribute any specific explanation to a change in diffusivity. If, for example, the model measures an increase in radial diffusivity, this could potentially be the result of axonal loss, edema, demyelination, or a number of other factors.

The second class of diffusion models take the biophysical properties of tissues into account (Jelescu and Budde, 2017). As these models aim to estimate intrinsic tissue properties, they are more independent of the acquisition sequence and parameters. The goal is to create a simplified version of the microstructural tissue environment that can then be analyzed. This means that such a model is tissue-specific. Biophysical models, unlike the aforementioned signal representation models, are then well-suited for identifying biomarkers that are specific for characterizing a particular type of microstructural change.

One widely used example of biophysical models is the multi-compartment model (Ferizi, 2014). In this model, it is assumed that the tissue is composed of various compartments which are defined for each specific microstructural change that may occur. Neurite orientation dispersion and density imaging (NODDI) is a popular 3 compartment model that can be applied to both white matter and grey matter (Zhang, Schneider, et al., 2012). The three

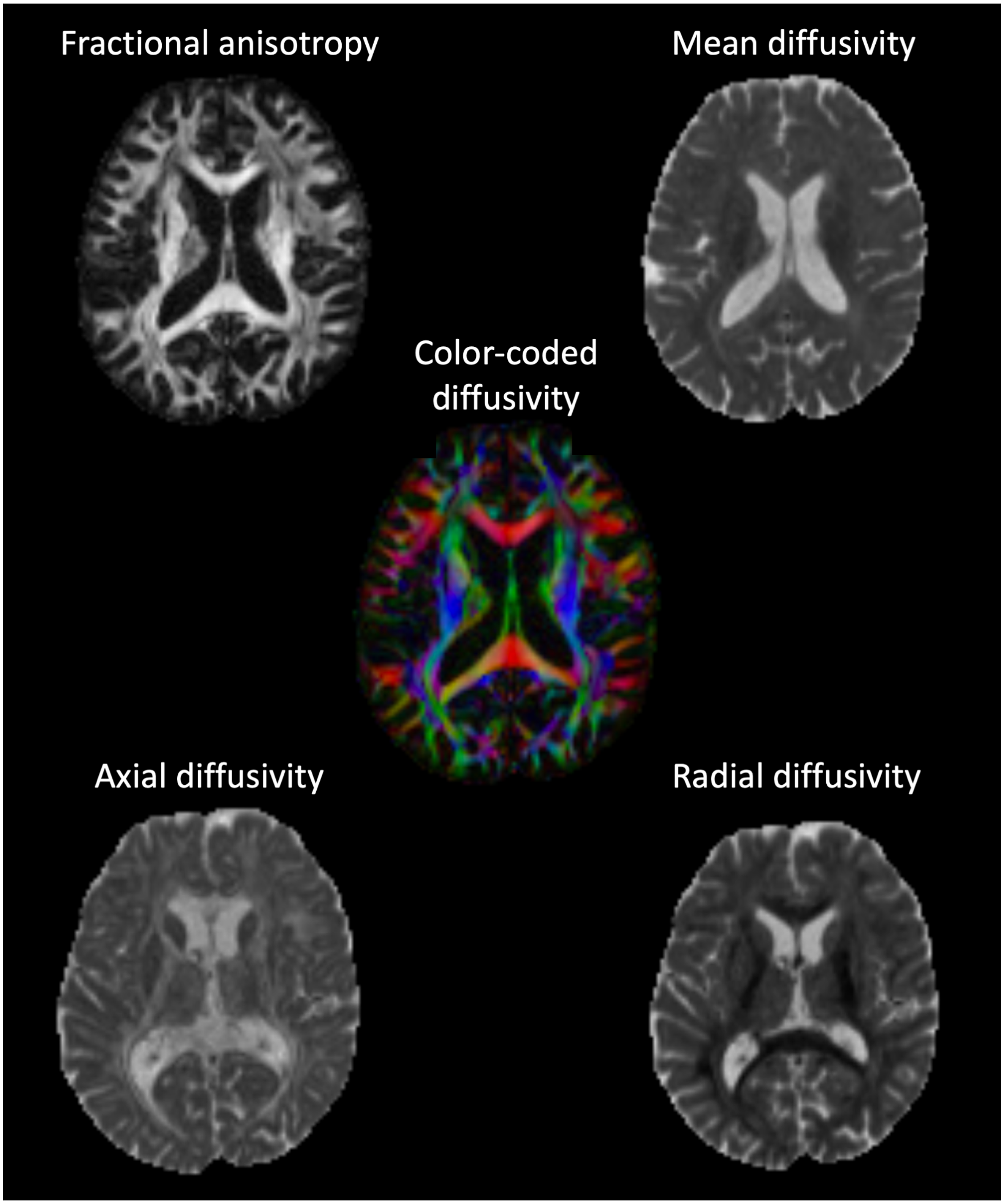

Figure 2.9 Scalar maps obtained with fitting the diffusion tensor from a set of DWI data.

compartments include an intra-axonal compartment, modeled as a collection of cylinders or sticks with an orientation distribution function, an extra-axonal compartment modeled as a Gaussian anisotropic space, and a third compartment for cerebral spinal fluid (CSF) that is modeled as a Gaussian isotropic space. These compartments are defined in such a way that their parameters can characterize specific diffusivity changes that may be attributed to a number of factors, such as axonal loss, inflammation, edema, or demyelination (By et al., 2017; Grussu et al., 2017).

## 2.5 Tractography and tractometry

As we have seen in one of the previous sections, diffusion MRI allows us to estimate the displacement of the water particles inside the brain. The diffusion of the water particles is restricted by neuronal structures. When there is a packing of axons that are parallel to each other, the water particles will be restricted in moving across those axons, but they will diffuse faster in a direction parallel to the axons (Moseley et al., 1990). Thus, by measuring diffusion along different orientations, it is possible to obtain information about the preferred orientation of the diffusion, which is assumed to correspond with the orientation of axonal fibers (Dell'Acqua and Tournier, 2017). Using this information about the directionality of the water particles in each voxel one can noninvasively estimate, on a macroscopic level, the anatomical connections that are connecting different parts of the brain (Sotiropoulos and Zalesky, 2019). The method that allows one to track the anatomical connections is known as fiber tracking, or tractography.

The simplest tractography models generate fiber trajectories, or streamlines, by linking together local fiber orientations that represent one predominant fiber orientation per voxel (Jeurissen, Descoteaux, et al., 2019). These local orientations are described by 3D vector fields. A streamline can then be represented mathematically as a 3D curve that is tangent to the vector field (Basser, Pajevic, et al., 2000). When a streamline is in alignment with, or is parallel to, the vector field, it can be characterized as follows:

$$\frac{d\mathbf{r}(s)}{ds} = \mathbf{v}[\mathbf{r}(s)] \tag{2.22}$$

where $\mathbf{v}$ is the 3D vector field and $\mathbf{r}(s)$ is the location along the streamline in which $\mathbf{r}$ is a function of the arc length $s$. This is a differential equation that can be solved through integration to give

$$\mathbf{r}(s) = \int_{s_0} \mathbf{v}[\mathbf{r}(s)]\, ds \tag{2.23}$$

where $\mathbf{r}(s_0) = \mathbf{r}_0$ represents the seed point, the starting point of the streamline. Fiber trajectories are then estimated by connecting local fiber orientations through an iterative integration process such as Euler integration (Conturo et al., 1999):

$$\mathbf{r}_{i+1} = \mathbf{r}_i + \mathbf{v}(\mathbf{r}_i)\Delta \tag{2.24}$$

where $\mathbf{r}_i$ is the location along the streamline, $\mathbf{v}(\mathbf{r}_i)$ is the local fiber orientation at that location, and $\Delta$ is the step size. As this is first-order integration, the local orientation is assumed to be constant at the scale of the step size. As a result, this method may not perform as well in highly curved regions as it will be much more prone to overshoots. This issue can be mitigated with higher-order integration techniques that consider variations in local orientation between $\mathbf{r}_i$ and $\mathbf{r}_{i+1}$ (Lazar and Alexander, 2003). Despite this improvement, the step-wise nature of these techniques still makes them susceptible to error propagation.

Integration methods, such as Euler or Runge–Kutta, necessitate that local fiber orientations be at spatial locations that do not coincide with the diffusion MRI voxel grid, so some type of interpolation will be required. Nearest-neighbor interpolation is the simplest approach (Mori, Crain, et al., 1999), but it is much more likely to accumulate errors. To reduce such errors, a smooth interpolation approach can be used in which contributions from all neighboring points are considered. The most common method is trilinear interpolation. This type of interpolation calculates local fiber orientation as a weighted sum of eight neighboring voxels (Conturo et al., 1999). Trilinear interpolation may be implemented either on the raw diffusion-weighted data (Jeurissen, Leemans, et al., 2011) or directly on the local fiber orientation data (Tournier, Calamante, et al., 2012b).

The collection of all fiber trajectories that is estimated by a tractography algorithm is referred to as a tractogram. Previous work has shown that tractograms can be very useful in many applications, such as neurosurgery (Costabile et al., 2019; Essayed et al., 2017; Fortin et al., 2012; Panesar et al., 2019; Vanderweyen et al., 2020), brain development (Cao et al., 2017; Dubois et al., 2014; Lebel et al., 2019), aging (Collin and Van Den Heuvel, 2013; Madden et al., 2009; Moseley, 2002), as well as neurological disorders, including, but limited to, MS (Kocevar et al., 2016; Sbardella et al., 2013), PD (Tan et al., 2015; Theisen et al., 2017), and schizophrenia (Goldsmith et al., 2018; Griffa et al., 2013). Tractography has become invaluable for the non-invasive delineation of white matter fiber pathways in the brain. It is routinely used to assess quantitative MRI parameters in white matter bundles. Such

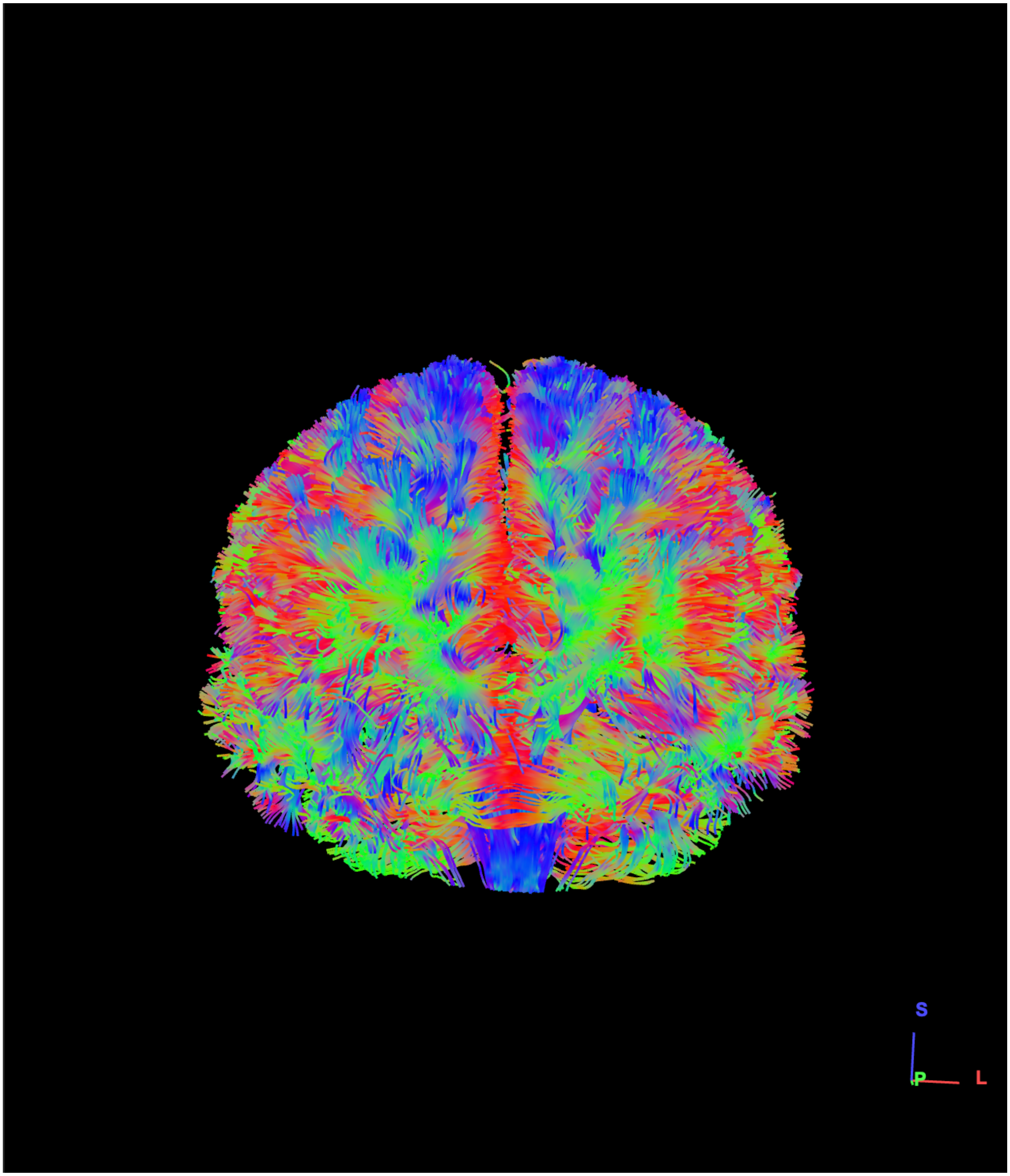

Figure 2.10 Whole brain tractogram. The streamlines are color coded by their directionality. Right-Left is color-coded red, Anterior-Posterior is color-coded green, Inferior-Superior is color-coded blue.

attributes, as well as the vast number of applications, make tractography a prominent method of choice for obtaining information about the physical connections that are responsible for transferring information between different regions of the brain (Jeurissen, Descoteaux, et al., 2019).

The utility of tractograms is limited, however. Given that any tractography technique involves multiple steps that may each contribute to the accuracy of the final tractogram, there are several potential sources of error. One of the most widely contested issues is that of local fiber orientation estimation. As a single white matter voxel may contain several thousand fibers, determining a single predominant fiber orientation will almost certainly fail to adequately capture the true fiber architecture. In essence, this means that various fiber configurations, such as crossing, kissing, fanning, or bending, may be represented by the same diffusion MRI measurements (Savadjiev et al., 2008). This, in turn, could lead to tracking errors, such as errors in trajectory accuracy (false positives) or premature termination (false negatives). In an effort to mitigate issues associated with intravoxel fiber orientations, a number of higher-order modeling approaches have been introduced, including $q$-ball imaging (Tuch, 2004) and CHARMED (Assaf et al., 2004). These methods aim to estimate the orientations of multiple fiber populations in a single voxel. They do so by using a continuous function of a sphere to characterize fiber orientations called the fiber orientation distribution function. This makes it possible to carry out fiber tracking for multiple types of fiber architecture.

Seed point selection is also a factor to consider in tractography. Consequently, whole-brain tracking in which seed points are deposited throughout the brain is the method of choice for initiating the tracking process. There are two main options for seed point placement: seeding from voxels near the gray matter-white matter interface (Li, Rilling, et al., 2012) or seeding from voxels located within the white matter (Huang et al., 2004). Seeding from the white matter ensures that all of the white matter will be probed. The disadvantage, however, is that some longer white matter bundles may be excessively defined by multiple seed points (Smith, Tournier, et al., 2013). While this is less of an issue for seed points close to the gray matter-white matter interface, tracking that is initiated at these locations cannot be guaranteed to encompass the entire white matter. Therefore, seed point selection must be carefully considered.

Finally, the choice of stopping criteria is also an important consideration for any tractography algorithm. Errors will continue to propagate as long as the algorithm continues, so it is imperative to identify locations along the streamline at which there is a high degree of uncertainty associated with the current path of that streamline. The two most widely used stopping criteria are local fiber orientation probability and curvature. FA is often employed as a measure of local fiber orientation probability (Toosy et al., 2004). The motivation for this choice is that areas with low FA values are more likely to be associated with less certainty in the principle diffusion direction. Thus, the next step in the streamline has greater potential for error. By stopping the algorithm when FA values drop below a certain threshold, it is possible to reduce the extent of error propagation within the tractogram. Likewise, the degree of streamline curvature can serve as a threshold for termination (Tournier, Mori, et al., 2011). Given the structure of many known white matter pathways, it is considered unlikely for a streamline to undergo a large bend on the scale of an imaging voxel. A maximum curvature threshold is therefore imposed for the angle between two successive steps. The streamline is terminated if an angle above this threshold is detected. Anatomically-constrained tractography (ACT) (Smith, Tournier, et al., 2012) aims to improve the accuracy of stopping criteria by using prior anatomical knowledge and/or structural information to make a more informed decision regarding tract termination. Rather than simply restricting streamlines to a specific region of interest, priors are constructed based on the biological properties of the underlying tissue as well as specific characteristics of the axons being studied. Streamlines are then considered valid if they meet the criteria outlined by the priors.

Though there are many different tractography algorithms, they can be classified into two main classes: deterministic and probabilistic. Deterministic tractography algorithms, in their simplest form, estimate the fiber trajectory by following the principal fiber orientation in each voxel (Schlaier et al., 2017). There are a number of factors that may hinder an accurate estimate of fiber orientation, such as artifacts and noise in the image (Jones, 2003). Probabilistic tractography, on the other hand, estimates a distribution of potential streamlines. For this approach a tract is characterized by the probability, or uncertainty, of its connection. This approach is useful for identifying connections in areas of the brain with high uncertainty. For places like this in which deterministic tractography might fail (prematurely terminate), probabilistic tractography will continue on, noting a lower probability for that particular connection. It is important to note, however, that since probabilistic tractography is built upon the same principles as deterministic, it is still susceptible to the same limitations.

The methods just discussed describes local tractography, i.e., it makes use of a step-wise integration process that follows local fiber orientations that are determined independently. As mentioned previously, due to an inability to differentiate between various types of complex fiber architectures, tractography approaches are limited in providing biologically meaningful tract representations. An alternative approach is to perform global tractography (Daducci, Dal Palu, et al., 2013; Fillard et al., 2009; Kreher et al., 2008; Reisert et al., 2009), which attempts to overcome the propagation of local inaccuracies. This method aims to estimate all trajectories simultaneously by identifying a configuration that best represents the diffusion MRI measurements (Reisert et al., 2009). In order to do this, a forward model must be defined to associate some contribution to the streamlines. Then, the resultant configuration must be evaluated to determine how well it corresponds to the data. Given that multiple potential solutions exist for this configuration, some type of prior knowledge regarding the expected properties of the trajectories is required. While determining the most appropriate form of prior knowledge may prove to be difficult, the primary drawback of this approach is its reliance on convergence to a globally optimal solution.

Previous works have shown that some of the most prominent limitations of tractography are the large number of false negatives (Innocenti et al., 2019), i.e., streamlines that are hard to estimate, and false positives, i.e., streamlines which should not really be present (Maier-Hein et al., 2017). Many methods have been proposed that tackle some of the limitations of tractography which can collectively be referred to as top-down approaches (also known as filtering algorithms). The goal of top-down approaches, such as spherical-deconvolution informed filtering of tractograms (SIFT) (Smith, Tournier, et al., 2013), SIFT2 (Smith, Tournier, et al., 2015), linear fascicle evaluation (LiFE) (Pestilli et al., 2014), convex optimization modelling for microstructure-informed tractography (COMMIT) (Daducci, Dal Palù, et al., 2014) and COMMIT2 (Schiavi et al., 2020), is to improve the accuracy of reconstructed tractograms by combining them with information about local tissue properties (Mangin et al., 2013). The SIFT2 method, for example, aims to generate a tractogram that is more biologically plausible by addressing the issue of streamlines connectivity quantization. The density of connections in the reconstructed tractogram does not generally coincide with the true density of the underlying axonal connections (Jones, Knösche, et al., 2013). SIFT2 estimates a unique effective cross-sectional area for each streamline to ensure that the resultant streamlines are consistent with fiber densities derived from the diffusion signal. Another example is COMMIT2, which is based on two key ideas: (i) streamlines are representations of actual neuronal fibers and (ii) neuronal fibers should be viewed as bundles rather than as separate entities. COMMIT2 aims to provide a unified framework for expressing both tractography and tissue microstructure. It does so by simultaneously reconstructing tracts that best explain the local axon density approximated from the diffusion-weighted signal while implementing a filtering procedure that minimizes the number of bundles generated. This method thus adds an additional element of prior anatomical knowledge that can be used to reduce the number of false positives that are estimated for the resulting tractogram.

Once a tractography approach has been chosen and the tractogram has been constructed, additional metrics can be calculated along the streamlines to obtain information about white matter changes. Early methods to extract information from DW images included tract based spatial statistics (TBSS) (Smith, Jenkinson, et al., 2006) or the computation of mean diffusion metrics, such as MD, RD, AD, or FA, along a tract. TBSS is performed by computing FA values along a white matter skeleton; these values can then be compared across groups of subjects. This approach is limited, though, by the fact that potentially useful information is excluded by restricting the analysis to the mean along a fiber tract (Corbin et al., 2017). The evaluation of mean diffusion metrics, moreover, is problematic because they have been shown to vary along a tract (Yeatman, Dougherty, Rykhlevskaia, et al., 2011). This may be due to a number of factors, including the fact that the length of some axons may be shorter than the length of the tract and that the entry and exit of different collections of neurons along the tract may not always coincide (Yeatman, Dougherty, Myall, et al., 2012).

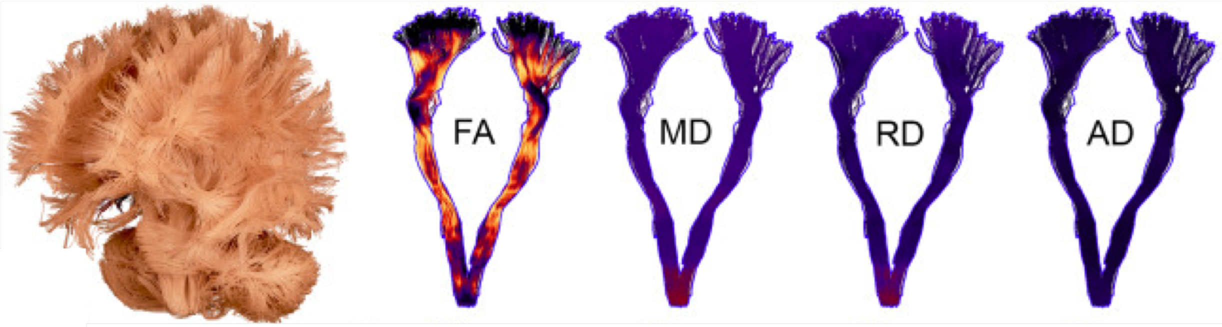

Figure 2.11 Graphical example of tractometry. From the whole brain tractogram (image on the left) the cortico-spinal tract (CST) is dissected (segmented), and various diffusion-derived measures are mapped along the CST. Image reproduced from (Chamberland et al., 2019)

In an effort to improve upon these methods, a process known as tractometry was proposed (Bells et al., 2011). This approach aims to create tract profiles for white matter bundles of interest within the brain by combining measures from multiple metrics along a tract. These profiles can then be used to identify relationships between brain structure and disease (Cousineau et al., 2017; Dayan et al., 2016; Groeschel et al., 2014). Tractometry is typically calculated on bundles of streamlines that were segmented either manually (Catani and Ffytche, 2005) or automatically (Guevara et al., 2011; Wassermann et al., 2016) from a whole brain tractogram (Rheault et al., 2017). Such metrics are indispensable for elucidating the ways in which brain microstructure relates to specific diseases (Michielse et al., 2010; Sala et al., 2012). It has been noted, though, that a formal theoretical link between differences in MRI-derived microstructural metrics and differences in brain function does not exist (Jones and Nilsson, 2014). Diffusion MRI has shown some measure of sensitivity to asses changes in tissue microstructure (De Santis, Drakesmith, et al., 2014a). It does, however, lack biological specificity. Alternative neuroimaging approaches, such as Relaxometry (Laule et al., 2007;

Mackay et al., 1994), magnetization transfer (Henkelman, Huang, et al., 1993), and magnetic susceptibility (Wharton and Bowtell, 2012), have thus been employed to increase specificity. By applying tractometry to these alternative approaches, it may be possible to identify a metric that is more specific to alterations in the underlying tissue microstructure.

## 2.6 Connectomics

Non-invasive imaging techniques such as the ones discussed in the previous sections (diffusion MRI), as well as functional MRI, electroencephalography (EEG), and magneto-electroencephalography (MEG), can be used to extract information about brain structure and function. This information can be further employed to provide a simplistic representation of brain connectivity known as a connectome. The term "connectome" was first used by Olaf Sporns, Giulio Tononi, and Rolf Kötter, to refer to the brain as a network (graph) (Sporns, Tononi, et al., 2005). A network is a mathematical structure that is composed of a set of nodes (vertices) and edges (links) connecting those nodes. The nodes in the graph refer to a neural element, while the links between nodes refer to some property of the connection between the nodes. Depending on the spatial level at which we are analyzing the brain, the neural element can refer to a single neuron (microscopic scale), a cluster of the same type of neurons, e.g., pyramidal neurons in the motor cortex (mesoscale), or they can refer to a region in the brain, e.g., amygdala, hypothalamus, etc. (macroscale). The links between these neural elements correspond to the type of brain connectivity. There are 3 such types of brain connectivity: i) structural (i.e., anatomical pathways), ii) functional (coupling between neural elements), and iii) effective connectivity (causal effects between neural elements) (Bullmore and Sporns, 2009; Sporns, 2011; Sporns, 2012). Most studies use the structural and functional connectivity to probe the brain structure and function.

Each type of network can be represented as an NxN matrix, where N is the number of nodes that constitute the network. Depending on the interactions of the system's elements, the network can be represented as directed or undirected, weighted or unweighted. The matrix that represents an unweighted network is called an adjacency matrix. This matrix is usually a binary matrix where each element can be either 0, if there is not a link between the nodes, or 1 if there is a link between the nodes. On the other hand, the matrix representing a weighted network is called a connectivity matrix. Each element of this matrix corresponds to the strength of the relationship between the nodes. Determining which of these network representations to use is often contingent upon the type of connectivity being investigated.

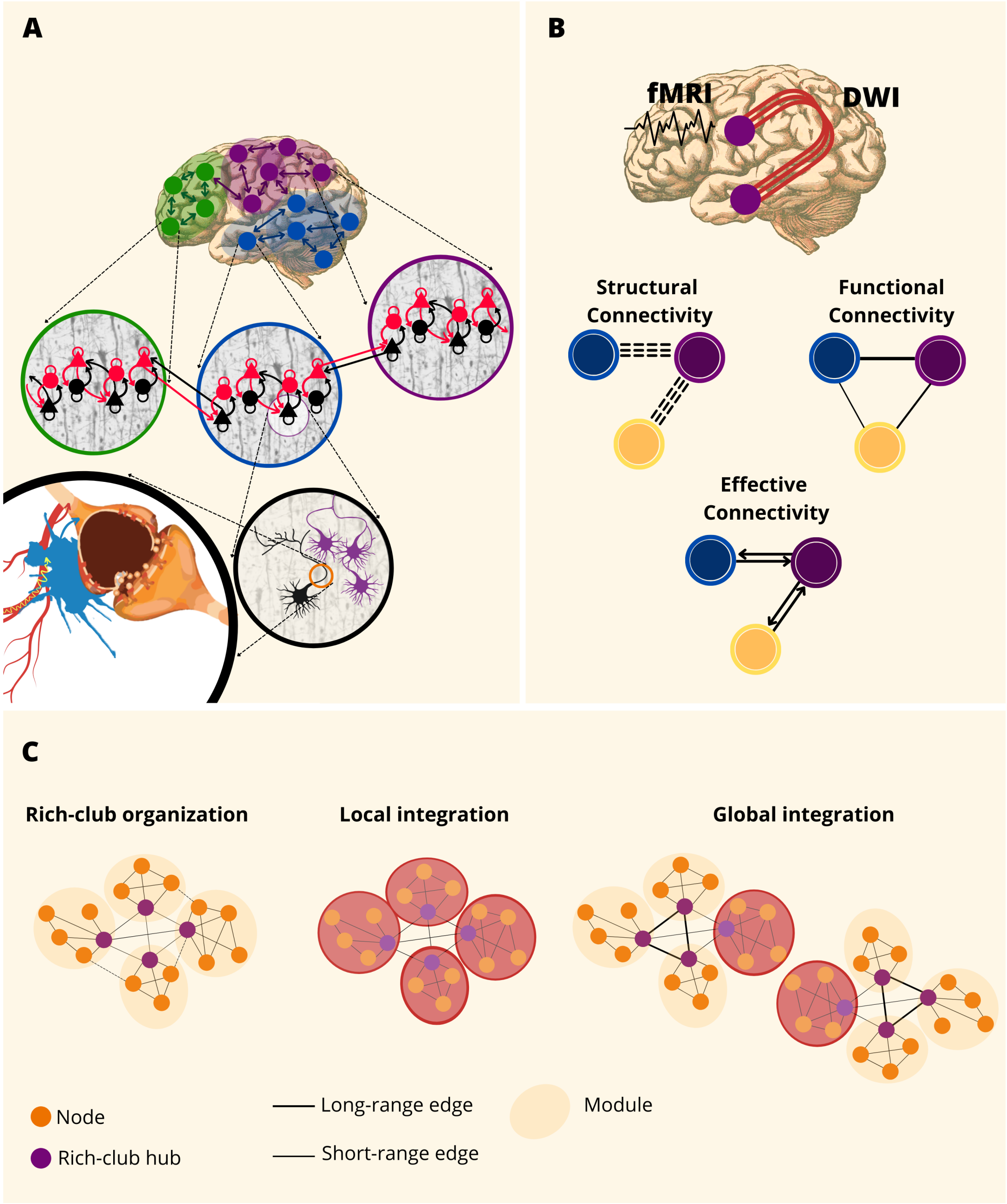

Figure 2.12 The human connectome. A) Multiscale organization of the human connectome in which the nodes represent a region of interest in the brain (macroscale), a population of neurons (mesoscale) or a single neuron (microscale). B) The different types of connectivity as well as the techniques used to extract the information about them. C) The highly modular brain organization showing the local integration of the nodes via short-rage connection, while the rich club network is composed of hub nodes (highly connected nodes) that are interconnected among themselves via long range connections allowing communication between different modules.

### 2.6.1 Structural connectome

The structural connectome is often referred as the wiring map of the brain. It describes a network of anatomical pathways that physically exist in the brain and connect cortical areas. Moreover, the structural connectome is usually represented as an undirected weighted or unweighted (binary) network. To reconstruct the connectome, most studies use diffusion MRI and tractography (Hagmann, Cammoun, et al., 2008a). There are, however, alternatives such as using a structural covariance analysis of conventional MRI for reconstruction of the structural connectome.

To better reflect the biological properties of the structural connectivity, it is very common to assign weights to the connections in the structural connectome. Various diffusion-derived measures have been used as weights. Two of the most commonly used measures are the number of streamlines (Hagmann, Cammoun, et al., 2008a) and the fractional anisotropy (Verstraete et al., 2011).

Many histological and connectomics studies have reported that the structural connectome has economical organization which is achieved by reducing the wiring cost (Achard and Bullmore, 2007; Bullmore and Sporns, 2012), implying that cortical regions that are spatially close to each other have a higher probability of being connected.

### 2.6.2 Functional connectome

The functional connectome aims to describe the "deviations from the statistical independence of the time series data, which is extracted from the spatially distributed brain regions"(Sporns, 2011). To estimate and reconstruct the functional connectome, advanced imaging methods such as functional MRI (fMRI) and electrophysiological techniques such as electroencephalography (EEG) or magnetoencephalography (MEG) are commonly used (Achard, Salvador, et al., 2006; Eguíluz et al., 2005; Salvador et al., 2005; Stam, 2004). The nodes in the reconstructed functional connectome refer to the anatomical regions (fMRI) or the spatial coordinates of the sensors. The edges in the functional connectome, on the other hand, represent the correlation or coherence between time series data extracted from the specific brain locations – nodes. The most commonly used technique to assess the functional connectome is fMRI. fMRI measures the Blood Oxygen Level Dependent (BOLD) signal. It measures the hemodynamic changes in the brain. This implies that the BOLD signal is an indirect measure of the brain activity. Therefore, it is critical to consider the limitations of fMRI. It depends on the changes of the oxygenated and deoxygenated hemoglobin in the brain. In the presence of some cardiovascular diseases, this measure will therefore provide an inaccurate signal (a lot of false positive or false negative activations).

### 2.6.3 Network topological measures

Once the connectivity/adjacency matrix for the network is calculated, one can then explore the topological properties of the network. The following paragraph describes some of network topological measures. A more complete description of the metrics used for examination of the topological properties can be found elsewhere (Rubinov and Sporns, 2010a). The topological properties of a network can be divided into two main classes: local and global. The local topological measures typically reflect the connectivity profiles of the individual network elements (nodes or links) while the global topological measures reflect the connectivity profile on a network. For example, one important local network measure is nodal degree/strength. The nodal degree (for unweighted networks) or strength (for weighted networks) is calculated as the number of connections (degree) or sum of connections' weights (strength) that emerge from a node. These measures provide information about the importance of the node in the network.

Two common classification criteria for networks are functional segregation and functional integration. The functional segregation measures how well the network is segregated into densely interconnected neural elements specialized in procession of a specific task. A common example of a functional segregation measure is the clustering coefficient. The clustering coefficient measures how densely the neighbors of a specific node are interconnected. Another more sophisticated example of functional segregation is the modular (community) structure, which extracts the densely interconnected nodes and groups them into functionally specialized modules or communities. The functional integration, on the other hand, measures how well the information from specialized neural elements can be combined or, in other words, how well the neural elements can communicate with each other. This is usually estimated in terms of paths. The paths are chains of specific nodes and edges that reflect the potential route of information flow. For each path one can estimate the path length. The global, or average, short path length of a network is called the characteristic path length and is defined as the average of the shortest paths between each pair of nodes. The inverse of the shortest path length defines the global efficiency of the network.

An important characteristic for many real world complex systems, including the brain, is the so-called "small-world" organization (Watts and Strogatz, 1998). A network that has small-world architecture exhibits high functional segregation and integration.

### 2.6.4 Connectomics as a biomarker of neurological diseases

Most of the neurodegenerative and neuroinflammatory diseases can be viewed as disconnectivity disorders (Mito et al., 2018; Pievani et al., 2014). Many studies (Griffa et al., 2013) that analyze brain connectivity in neurodegenerative and neuroinflammatory diseases support this theory. They have reported abnormalities in the brain network topology, i.e., infringement of the small world properties of the structural and functional networks. This section mainly focuses on the connectome analyses of the major neurodegenerative diseases (Alzheimer's and Parkinson diseases) and neuroinflammatory diseases (multiple sclerosis).

#### Alzheimer's disease

In connectomics studies of Alzheimer's disease (AD), reduction of the connectivity in both the structural and functional connectome have been noticed (Jack Jr and Holtzman, 2013; Mito et al., 2018; Pievani et al., 2014). More importantly, the disease spreads across the entire brain. The most affected regions in the structural connectome are the hubs. As reported in (Pievani et al., 2014), there is reduced FA in the limbic system and the fiber tract connecting the medial temporal lobe with the posterior cingulate. The posterior cingulate in structural connectome studies is identified as a hub (Leech and Sharp, 2014). The functional connectome analyses are in good agreement with the structural ones, and reported reduction of the functional connectivity of the regions involved in the default mode network (DMN), such as the posterior cingulate. In many graph theoretical analyses, it has been shown that both structural and functional connectomes experience disturbances in the small-world architecture. As reported in (Daianu et al., 2013), the connectomes in AD have a reduced clustering coefficient, implying a degradation of the functional segregation of the network.

#### Parkinson's disease

Parkinson's disease is a progressive neurodegenerative movement disorder characterized by tremor, imprecise movement, and hypertonia. A longitudinal MEG study of the functional connectome in Parkinson's disease patients reported a reduction of the local integration over theta, alpha1, and alpha2 frequency bands, affecting the global efficiency of the network (Olde Dubbelink et al., 2014). A decrease in the average path length in the alpha2 band was also present. Other fMRI studies have also shown reduced efficiency of the motor network (Skidmore et al., 2011; Wu et al., 2009). In a structural connectivity analysis of Parkinson's patients, microstructural damage has been shown to start in the brainstem and then spread through the basal ganglia to the neocortical layers of the brain (Agosta, Canu, Stojković, et al., 2013). Similar to that observed in the functional connectome, reduction of the global network efficiency has been reported (Li, Huang, et al., 2016), including the functional and structural integration of the connectome (Canu et al., 2015).

### Multiple sclerosis

Multiple sclerosis (MS) is a progressive neuroinflammatory disease that is identified by demyelinated lesions in the white matter tracts. Because MS affects the myelin content that wraps around the neural fibers and allows fast transmission of information, disturbances in both structural and functional connectomes have been reported (Fleischer et al., 2019; Sbardella et al., 2013; Shu, Duan, et al., 2016). Interestingly, even if there was a decrease of the connectivity of the structural connectome, some studies have observed an increase in the connectivity in the DMN and frontoparietal network (Akbar et al., 2016; Patel et al., 2016). These disturbances were in many studies characterized by reduction of the global connectivity network measures (global efficiency (Shu, Liu, et al., 2011; Shu, Duan, et al., 2016), clustering coefficient), but increase of the shortest path length (Shu, Duan, et al., 2016).

# CHAPTER 3 METHODOLOGY

Based on the literature review, described in Chapter 2, we have seen that the standard metrics to weight the connectome are the diffusion-derived metrics, FA and number of streamlines. However, the diffusion-derived metrics may not be that specific to the underlying microstructure. For example, the fractional anisotropy derived from diffusion MRI may be influenced by numerous processes such as axon diameter, fiber density, and (de-)myelination. Furthermore, we have seen that the diffusion tractography has several limitations, and, therefore, these limitations could propagate and influence the number of streamlines. However, many neurological diseases are affecting a specific property of the brain microstructure. For example, multiple sclerosis is a disease that affects the myelin content thereby requiring a more specific model of brain connectivity that will incorporate information about the myelin content in the connectome. All of the aforementioned problems identified in the literature review led us consider improving the current model of structural connectivity by complementing it with a measure that is more sensitive to the myelin content.

## 3.1 Research objectives

This thesis has two main objectives:

1. O1. Improve the model of structural brain connectivity by complementing it with microstructural information that plays a role in the information transmission and processing. In particular, the myelin sheath that wraps around the axons in white matter affects conduction speeds in the brain, but has yet to become an integral part of the connectome framework. Introducing the myelin-weighted connectome will improve our understanding of many pathologies in the brain that affect the myelin content.
2. O2. Apply the myelin-weighted connectome model to the analysis of neurological diseases. In particular, we will focus on neurodegenerative diseases, such as multiple sclerosis and Parkinson's disease, where microstructural changes often precede the manifestation of symptoms. This will lead to earlier diagnosis and better-informed decisions about the course of treatment in the clinic.

## 3.2 Plan of the thesis

The study presented in Chapter 4 introduces the use of a myelin-sensitive measure, R1, to complement the structural connectome obtained with diffusion MRI tractography. We weighted the connectome of 35 healthy subjects with R1 and then compared it with a connectome weighted by the NOS in order to evaluate the potential of R1 for identifying tissue myeloarchitecture. We compared the connectomes in terms of their node strength/weighted average distribution and their modular structure. The analysis demonstrated that the R1-weighted average distribution followed a different trend than the NOS strength distribution. Moreover, we showed that modular organization differed between the two connectomes. We then applied a rank-based analysis to further assess the difference between the two connectome weighting schemes on the modular organization. The rank-based analysis showed that R1 is underrepresented in the unimodal regions while it is overrepresented in the transmodal regions. These results provide evidence supporting our hypothesis that the myelin-weighted connectome offers a different perspective on structural connectivity by considering white matter myeloarchitecture. This information can be used to complement diffusion MRI-based connectivity in order to give a more complete picture of brain organization.

After showing that the myelin-weighted connectome (R1-weighted connectome) is capable of providing results that are complementary to the NOS-weighted connectome, we then used it to explore the alterations in myelin content in PD, which is detailed in Chapter 5. R1 was again used as a myelin measure to construct the myelin-weighted connectome. We used partial least squares to identify differences between healthy controls and PD patients by evaluating a multivariate connectivity pattern. A ring analysis was also carried out in order to determine whether any of eight nodes in the brainstem and cortex could be viewed as an epicenter for disease propagation. Finally, we also performed a behavioral PLS in an effort to relate a clinical motor score to changes in myelin content. This work demonstrated that the basal ganglia was the source of almost all of the connections that were found to have decreased myelin content in PD. A significant reduction in R1 was found for connections emerging from the prospective epicenter nodes. This study showed that the myelin-weighted connectome was capable of assessing alterations in myelin content in a neurodegenerative disorder such as PD.

Since it has been well established that MS is a neuroinflammatory disease that is known to affect myelin content, we next focused on using the myelin-weighted connectome to explore changes in myelin content in patients with this disorder. In Chapter 6, the myelin-weighted connectome was used to identify differences in myelin content in the normal-appearing white matter between healthy controls and MS patients. This study employed MTR as the myelin-specific metric used to weight the connectome. This MTR-weighted connectome was compared with a diffusion-based connectome that was weighted with FA. We showed that out of the connections that were different between healthy controls and MS patients, 100 were unique to the MTR-weighted connectome while 62 connections were unique to the FA-weighted connectome. These results further supported the potential for the myelin-weighted connectome to provide complementary information to a diffusion-weighted connectome.

# CHAPTER 4 ARTICLE 1: THE R1-WEIGHTED CONNECTOME: COMPLEMENTING BRAIN NETWORKS WITH A MYELIN-SENSITIVE MEASURE

Authors: T. Boshkovski[1], Lj. Kocarev[2], J. Cohen-Adad[1,3,4], B. Mišić[5], S. Lehéricy[6] N. Stikov[1,7] M. Mancini[1,8,9]

Affiliations:

1. NeuroPoly Lab, Polytechnique Montreal, Montreal, Canada
2. Macedonian Academy of Sciences and Arts, Skopje, Macedonia
3. Department of Neurosciences, Faculty of Medicine, University of Montreal, Montreal, QC, Canada
4. Functional Neuroimaging Unit, Centre de recherche de l'institut universitaire de gériatrie de Montréal, Montreal, QC, Canada
5. Montreal Neurological Institute, Montreal, QC, Canada
6. Paris Brain Institute (ICM), Centre for NeuroImaging Research (CENIR), Inserm U 1127, CNRS UMR 7225, Sorbonne Université, F-75013, Paris, France
7. Department of Neuroscience, Brighton and Sussex Medical School, University of Sussex, Brighton, United Kingdom
8. CUBRIC, Cardiff University, Cardiff, United Kingdom

This article has been published in an open access MIT Press journal, Network Neuroscience, on December 2020 (Boshkovski et al., 2020)

## 4.1 Abstract

Myelin plays a crucial role in how well information travels between brain regions. Complementing the structural connectome, obtained with diffusion MRI tractography, with a myelin-sensitive measure could result in a more complete model of structural brain connectivity and give better insight into white-matter myeloarchitecture. In this work we weight the connectome by the longitudinal relaxation rate (R1), a measure sensitive to myelin, and then we assess its added value by comparing it with connectomes weighted by the number of streamlines (NOS). Our analysis reveals differences between the two connectomes both in the distribution of their weights and the modular organization. Additionally, the rank-based analysis shows that R1 can be used to separate transmodal regions (responsible for higher-order functions) from unimodal regions (responsible for low-order functions). Overall, the R1-weighted connectome provides a different perspective on structural connectivity taking into account white matter myeloarchitecture.

## 4.2 Author Summary

In the present work, we show that by using a myelin-sensitive measure we can complement the diffusion MRI-based connectivity and provide a different picture of the brain organization. We show that the R1-weighted average distribution does not follow the same trend as the number of streamlines strength distribution, and the two connectomes exhibit different modular organization. We also show that unimodal cortical regions tend to be connected by more streamlines, but the connections exhibit a lower R1-weighted average, while the transmodal regions have higher R1-weighted average but fewer streamlines. This could imply that the unimodal regions require more connections with lower myelination, whereas the transmodal regions take more myelinated, but fewer, connections for a reliable transfer of information.

## 4.3 Introduction

The brain is a complex system that can be modelled as an intricate network of interconnected elements (Fornito et al., 2016). Using magnetic resonance imaging (MRI), connectomics aims to characterize macroscopic connectivity by viewing the brain as a set of nodes defined by functionally or anatomically distinguishable regions of interest (ROIs) and edges that are conventionally assumed to reflect the white matter tracts connecting those nodes (Bassett and Sporns, 2017; Hagmann, Kurant, et al., 2007; van den Heuvel, Stam, et al., 2008). Specifically, the white matter tracts can be reconstructed using diffusion MRI and tractography (Jeurissen, Descoteaux, et al., 2019; Mori and Van Zijl, 2002). To better characterize the relationship between the nodes and edges of a brain network, weights can be assigned to the connections, which are presumed to reflect relevant properties (Rubinov and Sporns, 2010b).

There is an ongoing debate as to the most appropriate choice of weighting for the connectome (Yeh, Jones, et al., 2020). So far, the most widely used weight is the number of streamlines (NOS), which counts the reconstructed streamlines, from diffusion tractography, between pairs of ROIs (Fornito et al., 2016). Although, previous work (Sinke et al., 2018; van den Heuvel, de Reus, et al., 2015) showed a positive correlation between NOS and tract-tracing connectivity, suggesting that NOS could be used in principle as a proxy for microstructural fiber count. The use of NOS to weight the structural connectome is still problematic (Calamante, 2019). In particular, NOS does not measure biologically meaningful properties such as conduction velocity or channel capacity. Additionally, fiber tracking often lacks specificity as it can be affected by a number of factors, including the tractography algorithm used (Jones, 2010a; Yeh, Jones, et al., 2020) as well as image acquisition parameters (Jones, Knösche, et al., 2013).

Another potential candidate for weighting the connections is the fractional anisotropy (FA) that can be obtained using diffusion tensor imaging (DTI). While FA does provide more insights into the microstructural properties of white matter, it is also influenced by numerous tissue properties, including axonal diameter, fiber density, tissue geometry, as well as the degree of myelination (Jones, Knösche, et al., 2013). Another reason why FA might not be the best candidate for weighting the connectome is because it is derived from the same diffusion-based measures that are used to reconstruct the tractography. To gain additional insights into the myeloarchitecture it would make sense to weight the connectome by a metric that is orthogonal to diffusion. Many quantitative MRI (qMRI) measures (i.e., magnetization transfer ratio [MTR], longitudinal relaxation rate [R1], myelin water fraction [MWF]) have been used to characterize myelin. Myelin is the dielectric material that wraps around the axons to enable fast conduction in the brain. The use of such metrics is particularly well suited for studies that examine activity dependent myelination (Sampaio-Baptista and Johansen-Berg, 2017) and pathology related to myelin-specific changes in brain connectivity.

Several studies (Caeyenberghs et al., 2016; Kamagata et al., 2019; Mancini, Giulietti, et al., 2018; van den Heuvel, Mandl, et al., 2010) used such myelin-sensitive MR measures in brain network models. Specifically, in the work of Caeyenberghs et al. (Caeyenberghs et al., 2016), multiple quantitative myelin-sensitive MRI metrics were used as weights, including the R1, which has been shown to be effective for myelin imaging (Stüber et al., 2014). Caeyenberghs et al. analyzed the white matter plasticity using connectomics to determine which measures best correlate with white matter plasticity during a working memory task. To weight the connectome they used diffusion-derived measures (FA, AD, MD, RD, TRF [total restricted fraction], TVF [tissue volume fraction], MWF), and relaxometry measures (R1 and R2). They reported that the increased global efficiency in the network during working memory tasks was best captured by the R1-weighted connectome. The influence of myelin on R1 values can be traced to its molecular composition. Voxels containing more myelinated axons have an increased proportion of macromolecules, which increases the longitudinal relaxation rate (Yeatman, Wandell, et al., 2014). Although R1 is affected by iron, calcium content, and axon size (Harkins et al., 2016) and count (Schmierer, Wheeler-Kingshott, et al., 2008), a recent meta-analysis showed that R1 is comparable to other MRI techniques for quantifying myelin content (Mancini, Karakuzu, et al., 2020).

In this article, we introduce a myelin-sensitive measure (R1) to the structural connectome.We do this by weighting the connections in the structural connectome using the median R1 value along a bundle of streamlines connecting pairs of brain regions. We then compared the R1-weighted connectome with the conventional NOS-weighted connectome in terms of multiple network attributes, including strength distribution and modular structure. The differences between the R1- and NOS-weighted connectomes in terms of their overall network organization have the potential to provide a complementary perspective on white matter myeloarchitecture, as R1 is more directly sensitive to myelin compared to NOS.

## 4.4 Materials and methods

### 4.4.1 Data acquisition

Thirty-five healthy volunteers (HC) (12 F / 23 M, mean age ± sd: $61.2 \pm 9.16$ years) participated in the present study. Subjects were scanned at the Paris Brain Institute (ICM – Institut du Cerveau), Paris, France. All subjects signed informed consent forms. The study was approved by the local ethics committee (Ethics Committee: Comité de Protection des Personnes [CPP] Ile de France VI - RCB: 2014-A00725-42). Scans were performed on a 3T SIEMENS Prisma Scanner. The protocol included (i) 3-shell DWI sequence ( $\mathrm{TR} = 10,400ms$, $\mathrm{TE} = 59ms$, voxel size=1.7x1.7x1.7 $mm^3$, number of gradient directions per shell = 64, 32, 8, at respectively b=2500, 700, 300 $\frac{s}{mm^2}$ ), and ii) magnetization-prepared 2 rapid acquisition gradient echoes (MP2RAGE) sequence for R1 mapping (TR=5000$ms$, TE=2.98$ms$, Flip Angles=4 deg and 5 deg, TI=700/2700 $ms$, FOV=256x232$mm$, voxel size=1$mm^3$).

### 4.4.2 Reconstruction of quantitative R1 maps

The MP2RAGE sequence (Marques, Kober, et al., 2010) produces two T1-weighted images with different flip angles and different inversion times (INV1 and INV2). These images are then combined to produce a more uniform T1w image (UNI). The UNI image was used to estimate the longitudinal relaxation times (T1 maps) using qMRLab (Karakuzu et al., 2020). The longitudinal relaxation rate (R1) was then calculated from the T1 maps as:

$$R_1 = \frac{1}{T_1} \tag{4.1}$$

The quantitative maps were reconstructed using the qMRLab module MP2RAGE (Karakuzu et al., 2020).

### 4.4.3 Anatomical and diffusion data pre-processing

As a first step in the anatomical preprocessing pipeline, background noise removal (O'Brien et al., 2014) was applied to the UNI images by using a combination of the two inversion time images with a denoising regularization factor of 70. The denoised UNI images were then processed using FreeSurfer 6.0 (Fischl, 2012) to segment the different tissues and parcellate the brain using the Desikan–Killiany Atlas (Desikan et al., 2006). To reduce the bias from the different parcel sizes, we subdivided them into finer regions of approximately equal size using the Lausanne 2008 parcellation (scale 125) (Cammoun et al., 2012; Hagmann, Cammoun, et al., 2008b), which resulted in 234 brain parcels. Furthermore, because this article focuses on the connectivity between cortical regions, we discarded all the subcortical regions from the analysis, which resulted in 219 brain regions.

The preprocessed anatomical images and parcellation, as well as the reconstructed quantitative maps for each subject, were transferred to the subject's diffusion space by coregistering them to the mean b0 image using $FSL\ FLIRT$ (Jenkinson, Bannister, et al., 2002; Jenkinson, Beckmann, et al., 2012) rigid body registration. Each registration was visually inspected to check the alignment (see Figure A.1 in the Supporting Materials). Besides the registration, all preprocessed images were visually inspected for errors.

The preprocessing of the diffusion images was done using $MRtrix3$ (Tournier, Smith, et al., 2019). First, we applied a noise removal technique (Veraart, Fieremans, et al., 2016; Veraart, Novikov, et al., 2016) followed by a Gibbs ringing artifacts removal method (Kellner et al., 2016) and a B1 field inhomogeneity correction. Then, the images were preprocessed for motion and inhomogeneity distortion correction using FSL's eddy (Andersson and Sotiropoulos,

2016) and topup tools (Andersson, Skare, et al., 2003), respectively. Furthermore, to increase the anatomical contrast and improve the tractography and registration, the preprocessed images were upsampled to a 1-mm isotropic resolution. Multitissue constrained spherical deconvolution (Jeurissen, Tournier, et al., 2014), followed by the anatomically constrained tractography method (Smith, Tournier, et al., 2012), were used to reconstruct the tractogram. We applied the SD_STREAM deterministic tracking algorithm (Tournier, Calamante, et al., 2012a) that used 1 million seeds dynamically placed using the SIFT model (Tournier, Calamante, et al., 2012a) that used 1 million seeds dynamically placed using the SIFT model (Smith, Tournier, et al., 2015). The tractography procedure was set to stop either when (i) it produces 200,000 streamlines and/or (ii) the maximum number of seeds (1,000,000) is reached. During tracking the maximum turning angle was set to 60 deg. Streamlines with length shorter than 20 mm or longer than 250 mm were discarded from the tractogram. Additional constraints were provided by the anatomically constrained tractography (ACT) framework (Smith, Tournier, et al., 2012).

### 4.4.4 Structural connectome reconstruction

Structural connectivity was represented using a weighted graph, where each node corresponded to one of the 219 cortical ROIs, and each edge reflected the presence of reconstructed streamlines between each pair of ROIs. Two metrics were used as weights of the connections: (i) the NOS reconstructed between two regions and (ii) the median R1 values along the bundle of reconstructed streamlines between two regions. The same steps were followed to reconstruct the FA-weighted connectome (see Supplementary Materials). We decided to use the median value of the metric (R1 or FA) along the tract for two main reasons: (i) the median is less sensitive to outliers and (ii) it does not assume a normal distribution of the values along the bundle.

To mitigate the problem with spurious connections reconstructed by the tractography algorithm, we considered two nodes as connected only if there are at least two streamlines connecting the specific pair of ROIs. Also, a more conservative threshold (at least five connections) was applied to test the robustness of the results.

A group consensus approach for both NOS- and R1-weighted connectomes was adopted to reduce individual variability in the reconstructed networks. The group consensus networks for both connectomes were constructed by taking into account only the connections that are present in at least 50% of the subjects (de Reus and van den Heuvel, 2013). The weight of a connection in the group consensus network corresponded to the median of the connection's weights across subjects. We then assessed the relationship between the connection's R1-

weighted connectome and the NOS-weighted connectome using linear regression, as well as between the R1-weighted connectome and the FA-weighted connectome.

### 4.4.5 NOS strength and R1 weighted average

We chose strength as a measure of centrality because of its straightforward interpretation. For the NOS-weighted connectome, the strength was calculated as:

$$S_i^{NOS} = \sum_j w_{ij} \tag{4.2}$$

where $i$ is a given node, $w_{ij}$ is the NOS connectivity between the nodes $i$ and $j$.

For the R1-weighted connectome, we looked at the R1-weighted average, as it is not influenced by the number of connections (Kamagata et al., 2019). The R1-weighted average was calculated as:

$$S_i^{R1} = \frac{\sum_j [w_{ij} v_{ij}]}{\sum_j w_{ij}} \tag{4.3}$$

where $i$ is a given node, $w_{ij}$ is the number of streamlines and $v_{ij}$ is the median R1 sampled along the bundle of those streamlines connecting the nodes $i$ and $j$.

We then looked at the distribution of the centrality measures for each weight. The nodes were first sorted according to their NOS strength. Then, we defined the hubs as regions that have NOS strength of at least 2 standard deviations above the mean NOS strength (van den Heuvel and Sporns, 2013). A more conservative hub definition, at least 3 standard deviations above the mean NOS strength, was also used. Then, we highlighted the hub regions, defined in the NOS-weighted connectome and in the R1-weighted connectome.

### 4.4.6 Modular Structure

To probe the modular structure of the NOS- and R1-weighted connectomes, we used a modularity maximization method (Blondel et al., 2008; Rubinov and Sporns, 2011; Sporns and Betzel, 2016). This is a common method that is used to divide a network into modules/communities with highly interconnected regions within, and less connected regions between the submodules. To achieve this, the method aims to maximize a quality function given by the following equation:

$$Q(\gamma) = \sum_{ij}[A_{ij} - \gamma P_{ij}]\delta(c_i, c_j) \tag{4.4}$$

where $A_{i,j}$ is the empirical connectivity matrix, and $P_{i,j}$ represents the estimated connectivity matrix given a specific null model. The module assignment of node i is described by the variable $c_i$, whereby $\delta(c_i, c_j)$ is the Kronecker function which is equal to 1 when $c_i = c_j$ and 0 otherwise.

The modularity maximization also depends on a resolution parameter ($\gamma$) , which makes it sensitive to different scales. If $\gamma < 1$, then the network is partitioned into larger modules, while for $\gamma > 1$ the method tends to find smaller modules.

To determine at which resolution the modular structure is best described, that is, when it maximizes the quality functions, for each connectome we iterated over $\gamma$ values ranging from 0.5 to 3 with steps of 0.1. At each step, we ran the Louvain algorithm 1,000 times (Blondel et al., 2008). Then, the resolution parameter ($\gamma$) with highest Q was selected on the basis of the highest Rand index (Traud et al., 2011) ) similarity and created a consensus modularity using the netneurotools package https://github.com/netneurolab/netneurotools.

### 4.4.7 Rank-based analysis

To further explore the modular structure and assess the difference between weights, a rank-based analysis (Vázquez-Rodríguez et al., 2019) was performed: the nodes were first sorted by their strength (for the NOS-weighted connectome) and by their weighted average (for the R1-weighted connectome) defining their nodal rank (1 meaning highest and 219 meaning lowest). Then, nodal ranks in the NOS-connectome were subtracted from the corresponding nodal ranks in the R1-weighted connectome. To normalize the difference, a z score normalization was applied. The nodes were then grouped according to the von Economo cytoarchitectonic parcellation (Scholtens et al., 2018) and Yeo's functional parcellation (Thomas Yeo et al., 2011). Finally, the median z score for each cytoarchitectonic and functional class was computed across the respective nodes.

## 4.5 Results

To assess the shared variance between the different connectomes, we first compared the connection weights of the R1-weighted connectome with the weights obtained from the NOS- and FA-weighted connectomes. We found that the R1 and NOS weights exhibited an $R^2$ of 0.023 ($p<0.01$), while the R1 and the FA weights exhibited $R^2$ of 0.24 ($p<0.01$) (Figure 4.1).

Given that R1 measures different microstructural properties compared to NOS and FA, the shared variance between the connections weighted with these measures is limited.

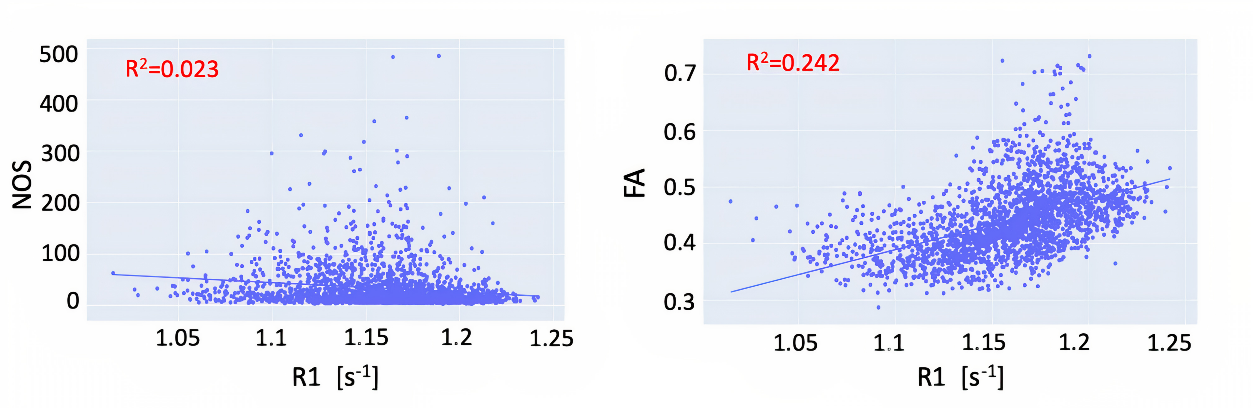

Figure 4.1 Relationship between the connection weights in the R1-weighted and FA-weighted connectome (left) and R1-weighted and NOS-weighted (right)

Next, we looked at the strength distribution and weighted average for the NOS- and R1-weighted connectomes. The strength distribution of the NOS-weighted connectome is heavy tailed (Figure 4.2). Among the nodes with the highest strength were the superior frontal gyrus, lateral occipital, pre- and postcentral gyrus (Table A.1 in the Supplementary Materials).

The R1-weighted average distribution did not follow the same trend as the NOS strength distribution (Figure 4.2). This result indicates that a high number of streamlines is not associated with higher R1 values. Also, the hubs defined with the more conservative threshold (at least 3 standard deviations above the mean NOS strength) did not exhibit a high R1-weighted average (Figure 4.2).

As for the community structure (Figure 4.3), the selected resolution parameter was 0.8 for the R1-weighted, while for the NOS-weighted connectome it was 2.6. The consensus modularity for the R1-weighted connectome yielded 5 modules with average modularity score $Q(\gamma) = 0.569$, whereas the NOS-weighted connectome yielded 11 modules with an average modularity score of $Q(\gamma) = 0.44$. We further explored the organization of the modules by looking at the distributions of the functional classes of the nodes provided by Yeo et al. (Thomas Yeo et al., 2011). Both the NOS and R1 modules were found to include multiple functional classes.

The rank-based analysis (Figure 4.4) shows where the functional and cytoarchitectonic classes are over- and underrepresented in terms of R1-weighted average and NOS strength. For Yeo's functional atlas, the R1 is overrepresented (compared to NOS) in the higher-order subnetworks (transmodal) and underrepresented for function-specific subnetworks (unimodal).

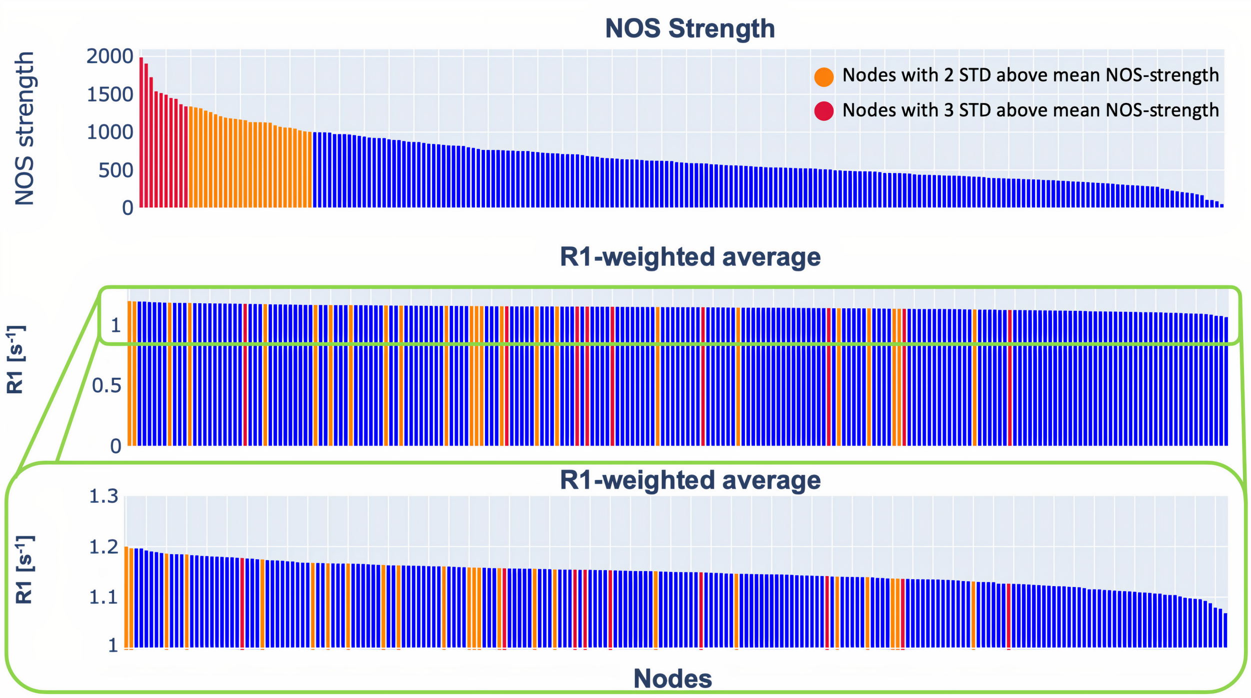

Figure 4.2 Nos strength and R1-weighted average distribution of the group NOS- and R1-weighted connectome. The plot in the middle shows the R1-weighted average distribution in the original range. However, since the trend of the R1-weighted average distribution is not visible in the original range, we selected a range that makes the trend more visible (bottom plot). In orange are highlighted the nodes that are two standard deviations above the mean NOS-strength, while in red are highlighted the nodes that are three standard deviations above the NOS-strength. The details about the nodes are provided in the supplementary materials.

However, this is not the case for the cytoarchitectonic subnetworks derived using the von Economo parcellation, that is, the transmodal/unimodal distinction was less obvious, as R1 was also underrepresented for the insular and the limbic subnetworks, which are transmodal.

We repeated the same analysis on the connectomes constructed with a stricter threshold, that is, two regions are connected if there are at least five streamlines reconstructed between them (see Supplementary Materials). The results showed that centrality measures' distributions and rank-based analysis are consistent between the two thresholds. However, regarding the modularity, the R1-weighted connectome yielded a different number of modules, although the community structure was still different from NOS. Furthermore, the same analysis was done on the connectome constructed using probabilistic tractography, and we have obtained similar results (see Supplementary Materials).

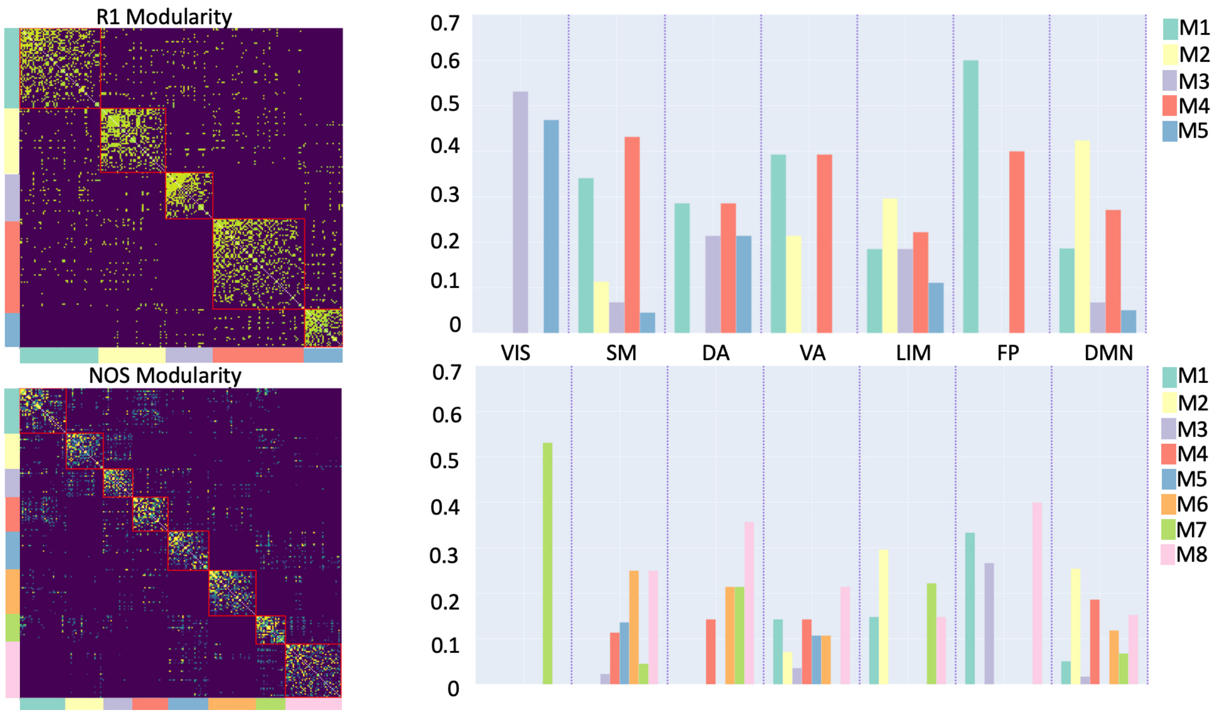

Figure 4.3 Community structure of the R1- and NOS-weighted connectomes. 5 modules were identified for R1 weighted connectome while 11 modules were identified for the NOS-weighted connectome. The bar plots represent the distributions of functional classes, given by Yeo et al. (Thomas Yeo et al., 2011), within the modules (denoted as $M\#$) for the R1- and NOS-weighted connectomes, respectively. Yeo's functional classes: SM (Somatomotor), VIS (Visual), VA (Ventral Attention), FP (Frontoparietal), LIM (Limbic), DA (Dorsal Attention), DMN (Default Mode Network)

## 4.6 Discussion

In this study, we showed that by using a myelin-sensitive measure we can complement the diffusion MRI-based connectivity and provide a different picture of the brain organization. To better characterize the myelin-weighted connectome, we decided to compare it with a connectome weighted by a diffusion-based metric. While there were several candidates for comparison, such as apparent axon density (Raffelt et al., 2012) and SIFT2 (Smith, Tournier, et al., 2015), we settled on NOS as it is the most commonly used approach.

First, we focused on the strength distribution and compared it to the R1-weighted average. From Figure. 4.2 one can appreciate that they do not follow the same trend. The R1-weighted average reflected a more uniform distribution. We also found that the hub regions, defined in the NOS connectome, do not necessarily have a high R1-weighted average. Similar results have been previously reported in (Mancini, Giulietti, et al., 2018) for a g-ratio-weighted

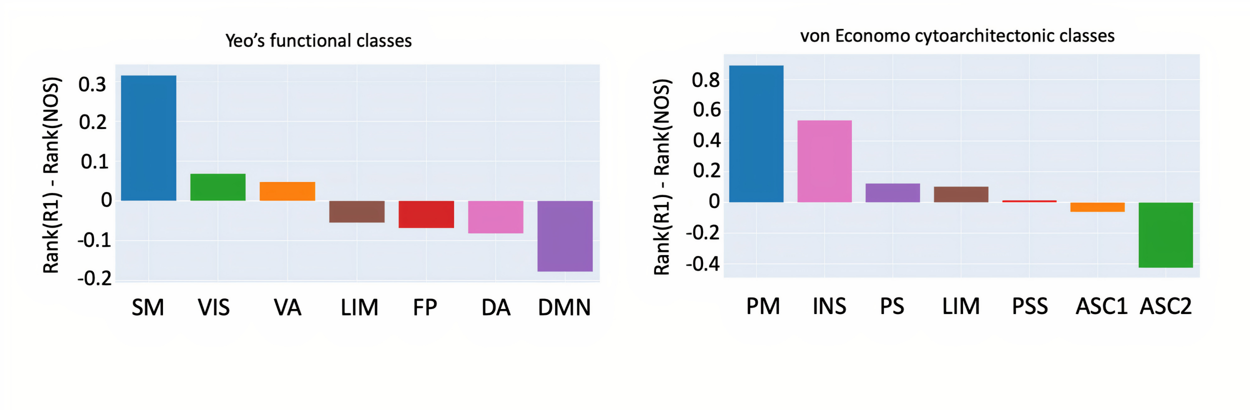

Figure 4.4 Rank-based comparison across functional and cytoarchitectonic classes. The rank for each node was calculated by its strength (for NOS)/weighted average (for R1) and then grouped using a cytoarchitectonic parcellation and functional one. Yeo's functional classes: SM (Somatomotor), VIS (Visual), VA (Ventral Attention), FP (Frontoparietal), LIM (Limbic), DA (Dorsal Attention), DMN (Default Mode Network). Von Economo cytoarchitectonic classes: PM (primary motor), INS (insular), LIM (Limbic), PS (primary sensory), PSS (primary secondary sensory), ASC1 (association cortex), ASC2 (association cortex 2)

connectome.

Second, we observed differences in the modular structure between the NOS- and R1-weighted connectomes. The number of modules was influenced by the resolution parameter, and a different number of modules was expected as the most optimal parameters were different for the two connectomes. However, what we wanted to highlight in this study was the different modular structure for the two weights, and to do this we partitioned the network in the most appropriate way for each weight. We also explored the distribution of the functional classes within the modules and found that there was limited agreement between the functional classes and the estimated modules, that is, the modules included multiple functional classes. This result is in agreement with results previously reported in the literature: it has been observed that structural and functional perspectives highlight different interregional relationships (Betzel et al., 2013; Goni et al., 2014; Honey et al., 2010; Suárez et al., 2020).

Regarding the rank-based analysis, we found that there was a good division of the unimodal versus transmodal functional classes. This pattern seems to follow the functional gradient observed in previous studies (Margulies et al., 2016; Vázquez-Rodríguez et al., 2019). An interesting result was that the unimodal regions exhibited more connections but in proportion a lower R1-weighted average, while the transmodal regions exhibited a higher R1-weighted average but less connections. A recent study has shown an opposite trend in cortical gray matter (Glasser and van Essen, 2011), but our study focuses on white matter connectivity and uses a different imaging modality (R1 versus T1w/T2w).

Our results showed that differences exist between the connectome weighted with NOS and the one weighted with R1 in terms of the distribution of their weights, as well as in the modular organization. Interestingly, the rank-based analysis showed an agreement in subdivision of the regions in unimodal and transmodal functional subnetworks. Future studies could focus on the relationship between white matter myeloarchitecture and function.

The use of qMRI metrics to weight the connectome could have important implications for many applications. qMRI offers several techniques that are sensitive to myelin (Laule et al., 2007; Petiet et al., 2019), such as magnetization transfer, myelin water imaging, or relaxometry (for extensive reviews see (Heath et al., 2018) and (Piredda et al., 2020)). Additionally, these techniques could be used to estimate the conduction velocity and conduction delays, and to incorporate these metrics as weights in the connectome. This would potentially result in a more complete model of the structural connectome and may provide a more comprehensive understanding of how the structure shapes the function. In this direction, Berman and colleagues calculated the conduction delay among the fibers in the corpus callosum using MRI-derived g-ratio (Berman et al., 2019). However, to calculate the conduction velocities and delays, in addition to the information about myelin, one would also need information about the axonal diameter and potentially information about other microstructural properties not accessible from MRI (Drakesmith et al., 2019). The work of Drakesmith et al. (Drakesmith et al., 2019), studied the feasibility of estimating conduction velocity in vivo using MRI microstructural measures. They performed simulations and reported that most of the variance in the estimation of the conduction velocity is explained by the axonal diameter and the g-ratio. However, axonal diameter can be accurately measured only with high gradients (300 mT/m) (Veraart, Nunes, et al., 2020) and is therefore not a measure that one can have on a clinical scanner yet. Additionally, even at such high gradients, the MRI-derived axonal measure is not sensitive to small axons ($1\mu m$ or lower) (Jones, Alexander, et al., 2018), so there are still challenges that need to be tackled in order to compute a robust estimate of the conduction velocity or delay.

There are a few methodological aspects of this work that are worth mentioning. The first is the choice of quantitative MRI metrics to weight the connectome (Collin, Sporns, et al., 2014; Collin, van den Heuvel, et al., 2016; Larivière et al., 2019; Messaritaki et al., 2019; Verstraete et al., 2011). As mentioned before, the structural connectome is often weighted using diffusion-derived metrics such as NOS and FA. . For NOS, this stems from the assumption that streamline count is a proxy of microstructural fiber count, that is, the greater the number of streamlines, the higher the connectivity between regions. This has been shown to be questionable, however, as results are influenced by the tractography algorithms and the choice of tracking parameters. Here we decided to use R1 to weight the connectome, as it has been repeatedly shown to correlate highly with myelin content (Lee, Shmueli, et al., 2012; Lutti et al., 2014). Also, the MP2RAGE sequence, which was used to acquire the R1 maps, is a stock, relatively short protocol with open-source processing, which makes it suitable for a wide clinical application. There are several studies that demonstrated the usefulness of complementing the tractography with longitudinal relaxation time. For instance, (De Santis, Drakesmith, et al., 2014b) showed that to compare two groups, that is, to detect differences between groups, the longitudinal relaxation time (T1), which is just an inverse of R1, requires a smaller sample size compared to the diffusion derived metrics. Another study (De Santis, Assaf, et al., 2016) demonstrated that it is possible to measure tract-specific T1 relaxation, potentially leading to fiber-specific myelin metrics and more thorough network models.

Another aspect is that here we weighted the connectome using the median rather than the standard approach of taking the mean along the bundle of reconstructed streamlines. This is due to the fact that the median is more robust against outliers and does not rely on the normality assumption for the R1 distribution along a fiber bundle. Relying on one measure per bundle instead of averaging a measure across streamlines also avoids biasing the results towards NOS.

Furthermore, we should also mention the choice of network measures that were investigated. The more canonical graph measures such as clustering coefficient and path length were not calculated. The rationale behind our choice is the consequence of the complex role of myelin in white matter pathways: myelinated axons show faster conduction than unmyelinated axons, but when comparing myelinated axons with different amount of myelin, the overall effect on conduction speed, as already mentioned, depends on several factors (e.g., axon diameter, g-ratio, internodal) (Drakesmith et al., 2019). Therefore, the use of myelin measures in network models requires more careful interpretation. As the weight in network models usually reflects the intensity or capacity of a connection (Barrat et al., 2004), most analyses rely on the same assumption. To take into account the myelin-specific role in conduction phenomena and to avoid the strict intensity-based interpretation of the network weight, we decided to focus on the use of R1-weighted average as a centrality measure (as previously done in (Kamagata et al., 2019)) and on the modular structure.

The choice of tractography algorithm is also an important methodological aspect that has to be considered when reconstructing the connectome. Two main classes of tractography algorithms, deterministic and probabilistic, can be employed to reconstruct the connectome. There is an ongoing debate on the advantages and disadvantages of these two classes of algorithms for mapping the connectome (Sarwar et al., 2019). Both classes of algorithms are valid choices for performing fiber tracking, but they also have some disadvantages: in recent studies (Maier-Hein et al., 2017; Sotiropoulos and Zalesky, 2019), it has been shown that the deterministic tractography algorithms reconstruct fewer true positive streamlines compared to probabilistic tractography. On the other hand, probabilistic tractography reconstructs more false positive streamlines as opposed to deterministic tractography, which further biases the reconstructed connectome by introducing spurious connections. In this study, we used both deterministic and probabilistic algorithms to double check the robustness of our results. The limitation of introducing spurious connections is particularly evident for modularity: the different results obtained for R1 using two different thresholds may imply that including spurious streamlines deeply affects the R1 weight distribution and therefore the estimated modular structure. To tackle these thresholding issues, new algorithms have recently been proposed (Schiavi et al., 2020; Smith, Tournier, et al., 2015) that aim to reduce the number of false positive streamlines by using microstructural and anatomical priors. Future studies need to clarify how such methods could be applied to combine tractography with complementary measures.

Finally, one limitation of this study is the relatively small sample size. Unfortunately, we are not aware of any publicly available dataset that includes quantitative MRI metrics (besides diffusion derived ones) that are sensitive to myelin.

In conclusion, the R1-weighted connectome complements the structural connectome derived from dMRI and could provide new biomarkers for many pathologies that affect the brain. Further validation of this approach is required, for example, by studying demyelinating diseases.

## 4.7 Data and code availability

The code and data, to reproduce the results, are available on GitHub
https://github.com/TommyBoshkovski/The_R1-weighted_connectome.

## 4.8 Supplementary materials

In the supplementary materials we provided additional results using also the FA to weight the connectome. We also reported the outcomes obtained using a more stringent threshold in the connectivity matrices.

## 4.9 Acknowledgements

We thank the ICEBERG study group and particularly Marie Vidailhet, MD (Pitié-Salpêtrière Hospital, Paris, Principal investigator), Jean-Christophe Corvol, MD, PhD (Paris Brain Institute, Paris, clinical and genetic data), Isabelle Arnulf, MD, PhD (Pitié-Salpêtrière Hospital, Paris, clinical and sleep data), Rahul Gaurav, MS, (Pitié-Salpêtrière Hospital, Paris, data analysis), Nadya Pyatigorskaya, MD, PhD, (Pitié-Salpêtrière Hospital, Paris, data analysis); for their help in collecting data. The research leading to these results has received funding from the programs "Investissements d'Avenir" ANR-10-IAIHU-06 and ANR-11-INBS-0006, the EDF Foundation, the Fondation Thérèse and René Planiol, Unrestricted support for Research on Parkinson's disease from Energipole (M. Mallart) and Société Française de Médecine Esthétique (M. Legrand), Montreal Heart Institute Foundation (NS), Canadian Open Neuroscience Platform (Brain Canada PSG) (NS), Quebec Bio-Imaging Network (NS, 8436-0501), Natural Science and Engineering Research Council of Canada (NS, 2016-06774) Fonds de Recherche du Québec (NS, FRSQ 36759 and FRSQ 35250). MM was funded by the Wellcome Trust through a Sir Henry Wellcome Postdoctoral Fellowship [213722/Z/18/Z].

## 4.10 References

Andersson, J. L., Skare, S., & Ashburner, J. (2003). How to correct susceptibility distortions in spin-echo echo-planar images: Application to diffusion tensor imaging. *NeuroImage*, *20*(2), 870–888.

Andersson, J. L., & Sotiropoulos, S. N. (2016). An integrated approach to correction for off-resonance effects and subject movement in diffusion MR imaging. *NeuroImage*, *125*, 1063–1078.

Barrat, A., Barthélemy, M., Pastor-Satorras, R., & Vespignani, A. (2004). The architecture of complex weighted networks. *Proceedings of the National Academy of Sciences of the United States of America*, *101*(11), 3747–3752.

Bassett, D., & Sporns, O. (2017). Network neuroscience. *Nature Neuroscience*, *20*(3), 353–364.

Berman, S., Filo, S., & Mezer, A. A. (2019). Modeling conduction delays in the corpus callosum using MRI-measured g-ratio. *NeuroImage*, *195*, 128–139.

Betzel, R. F., Avena-Koenigsberger, A., Goãi, J., Sporns, O., Griffa, A., Thiran, J. P., & Hagmann, P. (2013). Multi-scale community organization of the human structural connectome and its relationship with resting-state functional connectivity. *Network Science*, *1*(3), 353–373.

Blondel, V. D., Guillaume, J.-L., Lambiotte, R., & Lefebvre, E. (2008). Fast unfolding of communities in large networks. *Journal of Statistical Mechanics: Theory and Experiment*, *2008*(10), P10008.

Boshkovski, T., Kocarev, L., Cohen-Adad, J., Mišić, B., Lehéricy, S., Stikov, N., & Mancini, M. (2020). The R1-weighted connectome: complementing brain networks with a myelin-sensitive measure. *Network Neuroscience*, 1–15.

Caeyenberghs, K., Metzler-Baddeley, C., Foley, S., & Jones, D. K. (2016). Dynamics of the human structural connectome underlying working memory training. *Journal of Neuroscience*, *36*(14), 4056–4066.

Calamante, F. (2019). The Seven Deadly Sins of Measuring Brain Structural Connectivity Using Diffusion MRI Streamlines Fibre-Tracking. *Diagnostics*, *9*(3), 115.

Cammoun, L., Gigandet, X., Meskaldji, D., Thiran, J. P., Sporns, O., Do, K. Q., Maeder, P., Meuli, R., & Hagmann, P. (2012). Mapping the human connectome at multiple scales with diffusion spectrum MRI. *Journal of Neuroscience Methods*, *203*(2), 386–397.

Collin, G., Sporns, O., Mandl, R. C., & Van Den Heuvel, M. P. (2014). Structural and functional aspects relating to cost and benefit of rich club organization in the human cerebral cortex. *Cerebral Cortex*, *24*(9), 2258–2267.

Collin, G., van den Heuvel, M. P., Abramovic, L., Vreeker, A., de Reus, M. A., van Haren, N. E., Boks, M. P., Ophoff, R. A., & Kahn, R. S. (2016). Brain network analysis reveals affected connectome structure in bipolar I disorder. *Human Brain Mapping*, *37*(1), 122–134.

Crooks, L., Hylton, N. M., Ortendahl, D. A., Posin, J. P., & Kaufman, L. (1987). The value of relaxation times and density measurements in clinical MRI. *Investigative radiology*, *22*(2), 158–169.

De Santis, S., Assaf, Y., Jeurissen, B., Jones, D. K., & Roebroeck, A. (2016). T1 relaxometry of crossing fibres in the human brain. *NeuroImage*, *141*, 133–142.

De Santis, S., Drakesmith, M., Bells, S., Assaf, Y., & Jones, D. K. (2014a). Why diffusion tensor MRI does well only some of the time: Variance and covariance of white matter tissue microstructure attributes in the living human brain. *NeuroImage*, *89*(100), 35–44.

De Santis, S., Drakesmith, M., Bells, S., Assaf, Y., & Jones, D. K. (2014b). Why diffusion tensor MRI does well only some of the time: variance and covariance of white matter tissue microstructure attributes in the living human brain. *Neuroimage*, *89*, 35–44.

de Reus, M. A., & van den Heuvel, M. P. (2013). Estimating false positives and negatives in brain networks. *NeuroImage*, *70*, 402–409.

Desikan, R. S., Ségonne, F., Fischl, B., Quinn, B. T., Dickerson, B. C., Blacker, D., Buckner, R. L., Dale, A. M., Maguire, R. P., Hyman, B. T., Albert, M. S., & Killiany, R. J. (2006). An automated labeling system for subdividing the human cerebral cortex on MRI scans into gyral based regions of interest. *NeuroImage*, *31*(3), 968–980.

Dobbing, J., & Sands, J. (1973). Quantitative growth and development of human brain. *Archives of disease in childhood*, *48*(10), 757–767.

Drakesmith, M., Harms, R., Rudrapatna, S. U., Parker, G. D., Evans, C. J., & Jones, D. K. (2019). Estimating axon conduction velocity in vivo from microstructural MRI. *NeuroImage*, *203*, 116186.

Fischl, B. (2012). FreeSurfer. *NeuroImage*, *62*(2), 774–781.

Fornito, A., Zalesky, A., & Bullmore, E. T. (2016). *Fundamentals of Brain Network Analysis*. Elsevier Inc.

Glasser, M. F., & van Essen, D. C. (2011). Mapping human cortical areas in vivo based on myelin content as revealed by T1- and T2-weighted MRI. *Journal of Neuroscience*, *31*(32), 11597–11616.

Goni, J., van den Heuvel, M. P., Avena-Koenigsberger, A., Velez de Mendizabal, N., Betzel, R. F., Griffa, A., Hagmann, P., Corominas-Murtra, B., Thiran, J.-P., & Sporns, O. (2014). Resting-brain functional connectivity predicted by analytic measures of network communication. *Proceedings of the National Academy of Sciences*.

Hagmann, P., Cammoun, L., Gigandet, X., Meuli, R., Honey, C. J., Wedeen, V. J., & Sporns, O. (2008b). Mapping the structural core of human cerebral cortex. *PLoS biology*, *6*(7), e159.

Hagmann, P., Kurant, M., Gigandet, X., Thiran, P., Wedeen, V. J., Meuli, R., & Thiran, J.-P. (2007). Mapping Human Whole-Brain Structural Networks with Diffusion MRI (O. Sporns, Ed.). *PLoS ONE*, *2*(7), e597.

Harkins, K., Xu, J., Dula, A., Li, K., Valentine, W., Gochberg, D., Gore, J., & Does, M. (2016). The microstructural correlates of T1 in white matter. *Magnetic resonance in medicine*, *75*(3), 1341–1345.

Heath, F., Hurley, S. A., Johansen-Berg, H., & Sampaio-Baptista, C. (2018). Advances in noninvasive myelin imaging. *Developmental Neurobiology*, *78*(2), 136–151.

Honey, C. J., Thivierge, J. P., & Sporns, O. (2010). Can structure predict function in the human brain? *NeuroImage*, *52*(3), 766–776.

Jenkinson, M., Bannister, P., Brady, M., & Smith, S. (2002). Improved optimization for the robust and accurate linear registration and motion correction of brain images. *NeuroImage*, *17*(2), 825–841.

Jenkinson, M., Beckmann, C. F., Behrens, T. E. J., Woolrich, M. W., & Smith, S. M. (2012). FSL. *NeuroImage*, *62*(2), 782–790.

Jeurissen, B., Descoteaux, M., Mori, S., & Leemans, A. (2019). Diffusion MRI fiber tractography of the brain. *NMR in Biomedicine*, *32*(4), e3785.

Jeurissen, B., Tournier, J. D., Dhollander, T., Connelly, A., & Sijbers, J. (2014). Multi-tissue constrained spherical deconvolution for improved analysis of multi-shell diffusion MRI data. *NeuroImage*, *103*, 411–426.

Jones, D. K., Alexander, D. C., Bowtell, R., Cercignani, M., Dell'Acqua, F., McHugh, D. J., Miller, K. L., Palombo, M., Parker, G. J., Rudrapatna, U. S., & Tax, C. M. (2018). Microstructural imaging of the human brain with a 'super-scanner': 10 key advantages of ultra-strong gradients for diffusion MRI. *NeuroImage*, *182*, 8–38.

Jones, D. K. (2010a). Challenges and limitations of quantifying brain connectivity in vivo with diffusion MRI. *Imaging in Medicine*, *2*(3).

Jones, D. K. (2010b). *Diffusion MRI*. Oxford University Press.

Jones, D. K., Knösche, T. R., & Turner, R. (2013). White matter integrity, fiber count, and other fallacies: The do's and don'ts of diffusion MRI. *NeuroImage*, *73*, 239–254.

Kamagata, K., Zalesky, A., Yokoyama, K., Andica, C., Hagiwara, A., Shimoji, K., Kumamaru, K. K., Takemura, M. Y., Hoshino, Y., Kamiya, K., Hori, M., Pantelis, C., Hattori, N., & Aoki, S. (2019). MR g-ratio-weighted connectome analysis in patients with multiple sclerosis. *Scientific Reports*, *9*(1), 1–13.

Karakuzu, A., Boudreau, M., Duval, T., Boshkovski, T., Leppert, I. R., Cabana, J.-F., Gagnon, I., Beliveau, P., Pike, G. B., Cohen-Adad, J., & Stikov, N. (2020). qMRLab: Quantitative MRI analysis, under one umbrella. *Journal of Open Source Software*, *5*(53), 2343.

Kellner, E., Dhital, B., Kiselev, V. G., & Reisert, M. (2016). Gibbs-ringing artifact removal based on local subvoxel-shifts. *Magnetic Resonance in Medicine*, *76*(5), 1574–1581.

Larivière, S., Vos De Wael, R., Paquola, C., Hong, S. J., Mišić, B., Bernasconi, N., Bernasconi, A., Bonilha, L., & Bernhardt, B. C. (2019). Microstructure-informed connectomics: Enriching large-scale descriptions of healthy and diseased brains. *Brain Connectivity*, *9*(2), 113–127.

Laule, C., Vavasour, I. M., Kolind, S. H., Li, D. K., Traboulsee, T. L., Moore, G. R., & MacKay, A. L. (2007). Magnetic Resonance Imaging of Myelin. *Neurotherapeutics*, *4*(3), 460–484.

Lee, J., Shmueli, K., Kang, B. T., Yao, B., Fukunaga, M., Van Gelderen, P., Palumbo, S., Bosetti, F., Silva, A. C., & Duyn, J. H. (2012). The contribution of myelin to magnetic susceptibility-weighted contrasts in high-field MRI of the brain. *NeuroImage*, *59*(4), 3967–3975.

Lutti, A., Dick, F., Sereno, M. I., & Weiskopf, N. (2014). Using high-resolution quantitative mapping of R1 as an index of cortical myelination. *NeuroImage*, *93*, 176–188.

Maier-Hein, K. H., Neher, P. F., Houde, J. C., Côté, M. A., Garyfallidis, E., Zhong, J., Chamberland, M., Yeh, F. C., Lin, Y. C., Ji, Q., Reddick, W. E., Glass, J. O., Chen, D. Q., Feng, Y., Gao, C., Wu, Y., Ma, J., Renjie, H., Li, Q., … Descoteaux, M. (2017). The challenge of mapping the human connectome based on diffusion tractography. *Nature Communications*, *8*(1), 1–13.

Mancini, M., Giulietti, G., Dowell, N., Spanò, B., Harrison, N., Bozzali, M., & Cercignani, M. (2018). Introducing axonal myelination in connectomics: A preliminary analysis of g-ratio distribution in healthy subjects. *NeuroImage*, *182*, 351–359.

Mancini, M., Karakuzu, A., Cohen-Adad, J., Cercignani, M., Nichols, T. E., & Stikov, N. (2020). An interactive meta-analysis of MRI biomarkers of myelin. *eLife*, *9*.

Margulies, D. S., Ghosh, S. S., Goulas, A., Falkiewicz, M., Huntenburg, J. M., Langs, G., Bezgin, G., Eickhoff, S. B., Castellanos, F. X., Petrides, M., Jefferies, E., & Smallwood, J. (2016). Situating the default-mode network along a principal gradient of macroscale cortical organization. *Proceedings of the National Academy of Sciences of the United States of America*, *113*(44), 12574–12579.

Marques, J. P., Kober, T., Krueger, G., van der Zwaag, W., Van de Moortele, P. F., & Gruetter, R. (2010). MP2RAGE, a self bias-field corrected sequence for improved segmentation and T1-mapping at high field. *NeuroImage*, *49*(2), 1271–1281.

Messaritaki, E., Dimitriadis, S. I., & Jones, D. K. (2019). Optimization of graph construction can significantly increase the power of structural brain network studies. *NeuroImage*, *199*, 495–511.

Mori, S., & Van Zijl, P. C. (2002). Fiber tracking: Principles and strategies - A technical review. *NMR in Biomedicine*, *15*(7-8), 468–480.

O'Brien, K. R., Kober, T., Hagmann, P., Maeder, P., Marques, J., Lazeyras, F., Krueger, G., & Roche, A. (2014). Robust T1-Weighted Structural Brain Imaging and Morphometry at 7T Using MP2RAGE (D. Margulies, Ed.). *PLoS ONE*, *9*(6), e99676.

Petiet, A., Adanyeguh, I., Aigrot, M.-S., Poirion, E., Nait-Oumesmar, B., Santin, M., & Stankoff, B. (2019). Ultrahigh field imaging of myelin disease models: Toward specific markers of myelin integrity? *Journal of Comparative Neurology*, *527*(13), 2179–2189.

Piredda, G. F., Hilbert, T., Thiran, J.-P., & Kober, T. (2020). Probing myelin content of the human brain with MRI: A review. *Magnetic Resonance in Medicine*, mrm.28509.

Raffelt, D., Tournier, J. D., Rose, S., Ridgway, G. R., Henderson, R., Crozier, S., Salvado, O., & Connelly, A. (2012). Apparent Fibre Density: A novel measure for the analysis of diffusion-weighted magnetic resonance images. *NeuroImage*, *59*(4), 3976–3994.

Rubinov, M., & Sporns, O. (2010b). Complex network measures of brain connectivity: uses and interpretations. *NeuroImage*, *52*(3), 1059–69.

Rubinov, M., & Sporns, O. (2011). Weight-conserving characterization of complex functional brain networks. *NeuroImage*, *56*(4), 2068–2079.

Sampaio-Baptista, C., & Johansen-Berg, H. (2017). White Matter Plasticity in the Adult Brain. *Neuron*, *96*(6), 1239–1251.

Sarwar, T., Ramamohanarao, K., & Zalesky, A. (2019). Mapping connectomes with diffusion MRI: deterministic or probabilistic tractography? *Magnetic Resonance in Medicine*, *81*(2), 1368–1384.

Schiavi, S., Ocampo-Pineda, M., Barakovic, M., Petit, L., Descoteaux, M., Thiran, J.-P., & Daducci, A. (2020). A new method for accurate in vivo mapping of human brain connections using microstructural and anatomical information. *Science Advances*, *6*(31), eaba8245.

Schmierer, K., Wheeler-Kingshott, C. A., Tozer, D. J., Boulby, P. A., Parkes, H. G., Yousry, T. A., Scaravilli, F., Barker, G. J., Tofts, P. S., & Miller, D. H. (2008). Quantitative magnetic resonance of postmortem multiple sclerosis brain before and after fixation. *Magnetic Resonance in Medicine*, *59*(2), 268–277.

Scholtens, L. H., de Reus, M. A., de Lange, S. C., Schmidt, R., & van den Heuvel, M. P. (2018). An MRI Von Economo – Koskinas atlas. *NeuroImage*, *170*, 249–256.

Sinke, M. R., Otte, W. M., Christiaens, D., Schmitt, O., Leemans, A., van der Toorn, A., Sarabdjitsingh, R. A., Joëls, M., & Dijkhuizen, R. M. (2018). Diffusion MRI-based cortical connectome reconstruction: dependency on tractography procedures and neuroanatomical characteristics. *Brain Structure and Function*, *223*(5), 2269–2285.

Smith, R., Tournier, D., Calamante, F., & Connelly, A. (2012). Anatomically-constrained tractography: Improved diffusion MRI streamlines tractography through effective use of anatomical information. *NeuroImage*, *62*(3), 1924–1938.

Smith, R., Tournier, J., Calamante, F., & Connelly, A. (2015). SIFT2: Enabling dense quantitative assessment of brain white matter connectivity using streamlines tractography. *NeuroImage*, *119*, 338–351.

Sotiropoulos, S. N., & Zalesky, A. (2019). Building connectomes using diffusion MRI: why, how and but. *NMR in Biomedicine*, *32*(4), e3752.

Sporns, O., & Betzel, R. F. (2016). Modular Brain Networks. *Annual Review of Psychology*, *67*(1), 613–640.

Stüber, C., Morawski, M., Schäfer, A., Labadie, C., Wähnert, M., Leuze, C., Streicher, M., Barapatre, N., Reimann, K., Geyer, S., Spemann, D., & Turner, R. (2014). Myelin and iron concentration in the human brain: A quantitative study of MRI contrast. *NeuroImage*, *93*(P1), 95–106.

Suárez, L. E., Markello, R. D., Betzel, R. F., & Misic, B. (2020). Linking Structure and Function in Macroscale Brain Networks. *Trends in Cognitive Sciences*, *24*(4), 302–315.

Thomas Yeo, B. T., Krienen, F. M., Sepulcre, J., Sabuncu, M. R., Lashkari, D., Hollinshead, M., Roffman, J. L., Smoller, J. W., Zöllei, L., Polimeni, J. R., Fisch, B., Liu, H., & Buckner, R. L. (2011). The organization of the human cerebral cortex estimated by intrinsic functional connectivity. *Journal of Neurophysiology*, *106*(3), 1125–1165.

Tournier, J. D., Calamante, F., & Connelly, A. (2012a). MRtrix: Diffusion tractography in crossing fiber regions. *International Journal of Imaging Systems and Technology*, *22*(1), 53–66.

Tournier, J. D., Smith, R., Raffelt, D., Tabbara, R., Dhollander, T., Pietsch, M., Christiaens, D., Jeurissen, B., Yeh, C. H., & Connelly, A. (2019). MRtrix3: A fast, flexible and open software framework for medical image processing and visualisation. *NeuroImage*, *202*, 116137.

Traud, A. L., Kelsic, E. D., Mucha, P. J., & Porter, M. A. (2011). Comparing community structure to characteristics in online collegiate social networks. *SIAM Review*, *53*(3), 526–543.

van den Heuvel, M. P., Stam, C. J., Boersma, M., & Hulshoff Pol, H. E. (2008). Small-world and scale-free organization of voxel-based resting-state functional connectivity in the human brain. *NeuroImage*, *43*(3), 528–539.

van den Heuvel, M. P., de Reus, M. A., Feldman Barrett, L., Scholtens, L. H., Coopmans, F. M., Schmidt, R., Preuss, T. M., Rilling, J. K., & Li, L. (2015). Comparison of diffusion tractography and tract-tracing measures of connectivity strength in rhesus macaque connectome. *Human Brain Mapping*, *36*(8), 3064–3075.

van den Heuvel, M. P., Mandl, R. C. W., Stam, C. J., Kahn, R. S., Hulshoff Pol, H. E., Heuvel, v. d. M. P., Mandl, R. C. W., Stam, C. J., Kahn, R. S., & Pol, H. E. H. (2010). Aberrant Frontal and Temporal Complex Network Structure in Schizophrenia: A Graph Theoretical Analysis. *The Journal of Neuroscience*, *30*(47), 15915–15926.

van den Heuvel, M. P., & Sporns, O. (2013). Network hubs in the human brain. *Trends in Cognitive Sciences*, *17*(12).

Vázquez-Rodríguez, B., Suárez, L. E., Markello, R. D., Shafiei, G., Paquola, C., Hagmann, P., Van Den Heuvel, M. P., Bernhardt, B. C., Spreng, R. N., & Misic, B. (2019). Gradients of structure–function tethering across neocortex. *Proceedings of the National Academy of Sciences of the United States of America*, *116*(42), 21219–21227.

Veraart, J., Fieremans, E., & Novikov, D. S. (2016). Diffusion MRI noise mapping using random matrix theory. *Magnetic Resonance in Medicine*, *76*(5), 1582–1593.

Veraart, J., Novikov, D. S., Christiaens, D., Ades-aron, B., Sijbers, J., & Fieremans, E. (2016). Denoising of diffusion MRI using random matrix theory. *NeuroImage*, *142*, 394–406.

Veraart, J., Nunes, D., Rudrapatna, U., Fieremans, E., Jones, D. K., Novikov, D. S., & Shemesh, N. (2020). Noninvasive quantification of axon radii using diffusion MRI. *eLife*, *9*.

Verstraete, E., Veldink, J. H., Mandl, R. C., van den Berg, L. H., & van den Heuvel, M. P. (2011). Impaired structural motor connectome in amyotrophic lateral sclerosis. *PLoS ONE*, *6*(9).

Yeatman, J., Wandell, B., & Mezer, A. (2014). Lifespan maturation and degeneration of human brain white matter. *Nature Communications*, *5*(1), 4932.

Yeh, C.-H., Jones, D. K., Liang, X., Descoteaux, M., & Connelly, A. (2020). Mapping Structural Connectivity Using Diffusion MRI: Challenges and Opportunities. *Journal of Magnetic Resonance Imaging*.

# CHAPTER 5 ARTICLE 2: THE MYELIN-WEIGHTED CONNECTOME IN PARKINSON'S DISEASE

**Authors:** T. Boshkovski[1], J. Cohen-Adad[1,2,3], B. Mišić[4], I. Arnulf [5], J-C. Corvol[5], M. Vidailhet[5], S. Lehéricy[5], N. Stikov[1,6,a], M. Mancini[1,7,8,a]

**Affiliations:**

1. NeuroPoly Lab, Polytechnique Montreal, Montreal, Canada
2. Department of Neurosciences, Faculty of Medicine, University of Montreal, Montreal, QC, Canada
3. Functional Neuroimaging Unit, Centre de recherche de l'institut universitaire de gériatrie de Montréal, Montreal, QC, Canada
4. Montreal Neurological Institute, Montreal, QC, Canada
5. Sorbonne Université, Paris Brain Institute - ICM, Inserm, CNRS, Assistance Publique Hôpitaux de Paris, Hôpital Pitié-Salpêtrière, Paris, France
6. Department of Neuroscience, Brighton and Sussex Medical School, University of Sussex, Brighton, United Kingdom
7. CUBRIC, Cardiff University, Cardiff, United Kingdom

a. These authors equally contributed to this work

This article has been submitted to Movement Disorders journal.

## 5.1 Abstract

**Background**: Even though Parkinson's disease (PD) is typically viewed as largely affecting the gray matter, there is growing evidence that there are also structural changes in the white matter. Traditional connectomics methods that study PD may not be specific to underlying microstructural changes, such as myelin loss.

**Objective**: The primary objective of this study is to investigate the PD-induced changes in myelin content in the connections emerging from the basal ganglia and the brainstem. For the weighting of the connectome we used the longitudinal relaxation rate (R1) as a biologically grounded myelin sensitive metric.

**Methods**: We computed the myelin-weighted connectome in 35 healthy controls (HC) and 81 PD patients. We used partial least squares (PLS) to highlight the differences between PD and HC. Then, a ring analysis was performed on selected brainstem and subcortical regions to evaluate each node's potential role as an epicenter for disease propagation. Then, we used behavioral PLS to relate the myelin alterations with a clinical motor score.

**Results**: Most connections (~80%) emerging from the basal ganglia showed a reduced myelin content. The connections emerging from potential epicentral nodes (substantia nigra, nucleus basalis of Meynert, amygdala, hippocampus, and midbrain) showed significant decrease in the longitudinal relaxation rate ($p<0.05$). This effect was not seen for the medulla and the pons.

**Conclusion**: The myelin-weighted connectome was able to identify alteration of the myelin content in PD in basal ganglia connections. This could provide a different view on the importance of myelination in neurodegeneration and disease progression.

## 5.2 Introduction

Parkinson's disease (PD) is a neurodegenerative disorder that is characterized by motor and non-motor symptoms. PD is considered to be a disease that mainly affects the gray matter, specifically the dopaminergic neurons that affect motor function. Additionally, this disease has been characterized by the accumulation of misfolded $\alpha$-synuclein proteins across the brain (Breydo et al., 2012; Brundin and Melki, 2017; Luk et al., 2012; Masuda-Suzukake et al., 2013). It has also been noted that the myelination status and the size of the axons could play an important role in neurodegeneration in PD (Braak and Del Tredici, 2009). According to this hypothesis, long axons that are sparsely or poorly myelinated seem to be more susceptible to neurodegeneration. A well-established model of PD suggests that the disease progression, i.e. neurodegeneration, follows a topological sequence (Braak, Del Tredici, et al., 2003). According to the Braak hypothesis, there are 6 stages of disease progression. The disease first affects the lower part of the brain stem and then spreads to the medulla oblongata, the pons, the midbrain, the mesocortex and, finally, the neocortex. An alternative hypothesis for the disease spreading has also been proposed, according to which the disease first starts in the cortex and then spreads to the rest of the brain (Hawkes et al., 2007; Ubeda-Bañon et al., 2014). It has been recently suggested that neurodegeneration in PD patients with rapid eye movement sleep behavior disorder (RBD) follows the Braak model ("bottom-up") of disease progression (Knudsen et al., 2018; Pyatigorskaya, Yahia-Cherif, et al., 2021) whereas neurodegeneration in PD patients without RBD follows the alternative "top-down" model (from cortex to brainstem) (Horsager et al., 2020; Pyatigorskaya, Yahia-Cherif, et al., 2021). Like other neurodegenerative disorders, one possible hypothesis of PD progression is that it progresses by means of a prion-like mode of transmission throughout the brain (Iturria-Medina and Evans, 2015; Jucker and Walker, 2013; Seeley et al., 2009; Warren et al., 2013; Zheng et al., 2019). This mechanism of transmission is characterized by the trans-neuronal spread of misfolded $\alpha$-synuclein, i.e., one misfolded protein can prompt misfolding in adjacent proteins. In this manner, the pathology can travel from one brain region to another via interconnected neural pathways. The trans-neuronal spread of how misfolded proteins propagate through the brain is analogous to the manner in which infectious diseases are known to spread through person-to-person contact. Hence, several studies (Pandya et al., 2019; Zheng et al., 2019) have employed spreading models, such as the susceptible-infected-removed model or the network-diffusion model, to investigate how the degeneration propagates through the brain. Magnetic resonance imaging (MRI) has made it possible to investigate the neurodegenerative patterns of PD in vivo (Yau et al., 2018). A number of diffusion-weighted imaging (DWI) studies, in particular, have demonstrated alterations in brain network architecture in various cortical and subcortical systems. Moreover, changes in tensor metrics such as radial diffusivity (RD) and fractional anisotropy (FA) in nigrostriatal fibers are related to the extent of motor deficits present in patients with PD (Zhang, Wu, et al., 2015). White matter abnormalities are routinely found in the white matter of the frontal and parietal lobes (Karagulle Kendi et al., 2008; Zhan et al., 2012). White matter microstructural damage in PD patients who do not exhibit cognitive impairment has also been found to occur before gray matter atrophy can be detected (Agosta, Canu, Stefanova, et al., 2014). Although diffusion imaging has repeatedly identified white matter abnormalities in PD, the diffusion metrics are not specific to one particular microstructural property and can be affected by different pathological mechanisms such as neuronal and myelin loss. Only recently researchers have started to investigate whether PD affects the myelin in the white matter. In the study of Dean et al. (Dean et al., 2016), the authors performed a voxel-wise comparison of myelin sensitive MRI metrics (myelin water fraction [MWF], longitudinal relaxation rate [R1] and transverse relaxation rate [R2]) and found that there were myelin alterations in the frontal and temporal white matter. Another study (Baumeister et al., 2019) used the myelin water fraction (MWF) to investigate the alterations in myelin content in 20 different white matter regions of interest (ROIs). They did not find any significant differences between the PD and healthy controls, but they did find that the MWF was negatively correlated with clinical scores. In this paper, we took a whole brain connectomics approach to investigate the effect of Parkinson's disease on myelin in the white matter. There is a growing interest in evaluating pathology for which myelin-specific changes in brain connectivity are suspected (Kamagata et al., 2019; Mancini, Giulietti, et al., 2018; van den Heuvel, Mandl, et al., 2010). Several myelin-sensitive metrics have been proposed, including magnetization transfer ratio and the g-ratio, as well as R1, which has been shown to provide a complementary perspective on white matter myeloarchitecture (Boshkovski et al., 2020; Caeyenberghs et al., 2016). For this study we chose R1 as it has been shown to be highly correlated with myelin content (Mancini, Karakuzu, et al., 2020; Stüber et al., 2014) in a broad range of pathologies. Then, we performed multivariate statistical analysis to test the hypothesis that most of the alteration of the myelin alteration is concentrated in the connections emerging from the subcortical regions.

## 5.3 Materials and Methods

### 5.3.1 Subjects

35 healthy volunteers (HC) (12 F / 23 M, mean age ± sd: $61.2 \pm 9.16$ years) and 81 subjects with PD (52F/29M, mean age ± sd: $61.6 \pm 9.6$ years) participated in the present study. The study was approved by the local ethics committee (CPP Paris VI, RCB: 2009-A00922-55). All subjects provided a written informed consent.

### 5.3.2 Clinical assessment

The subjects were evaluated using the H&Y staging (Hoehn and Yahr, 1967). For all subjects the motor disability was assessed in the "OFF" state, following 12 hours withdrawal of dopaminergic treatment, using the Movement Disorders Society - Unified Parkinson's Disease Rating Scale, part III. The PD subjects were also evaluated for presence of REM sleep behavior disorder (RBD) using polysomnographic (PSG) recordings. Therefore, the PD subjects were subdivided into 2 groups: PD with RBD (PDRBD) which consisted of 22 subjects, and PD without RBD (PDnonRBD) which included 59 subjects.

### 5.3.3 MRI data acquisition

Each of the participants was scanned on a 3T SIEMENS Prisma Scanner following a multimodal acquisition protocol. The protocol included: i) 3-shell diffusion-weighted imaging (DWI) sequence ( TR = 10,400 $ms$, TE = 59 $ms$, voxel size=1.7x1.7x1.7 $mm^3$, number of gradient directions (per shell) = 64, 32, 8 at respectively b=2500, 700, 300 $s/mm^2$), ii) magnetization-prepared 2 rapid acquisition gradient echoes (MP2RAGE) sequence to estimate the longitudinal relaxation rate R1 (TR=5000 $ms$, TE = 2.98 $ms$, Flip Angles = 4 deg and 5 deg, TI=700/2700 ms, FOV=256x232 $mm$, voxel size=1x1x1 $mm^3$).

### 5.3.4 R1 map reconstruction

The R1 map was calculated using the qMRLab software tool (Karakuzu et al., 2020). To reconstruct the map, a UNI image is used. The UNI image is obtained with a combination of two T1-weighted images (INV1 and INV2), produced with the MP2RAGE protocol (Marques, Kober, et al., 2010), with different flip angles and with different inversion times. The benefit of using the unified T1-weighted image is that it is free from proton density and T2* contrast.

### 5.3.5 Data preprocessing

The T1-weighted images for each subject were first denoised using a robust noise background removal tool (O'Brien et al., 2014) as implemented in https://github.com/JosePMarques/MP2RAGE-related-scripts, and and N4 bias field correction (version 2.2) (Tustison et al., 2010) was applied. Following the denoising and the bias correction, the images were processed using FreeSurfer 6.0 (Fischl, 2012) to segment the different brain tissues and to parcellate the brain using the Desikan-Killiany atlas (Desikan et al., 2006). We used the following additional ROIs to cover all the structures of interest for PD: (1) the midbrain and the pons, as segmented from FreeSurfer (Iglesias et al., 2015); (2) the posterior part of medulla oblongata, which was manually segmented (Pyatigorskaya, Mongin, et al., 2016); (3) the locus coeruleus (LC), which was segmented semi-automatically as previously described (Gallea et al., 2017; García-Lorenzo et al., 2013); (4) the nucleus basalis of Meynert (NBM), which was segmented manually using T1-w and T2-w images; (5) the substantia nigra (SN), obtained from the atlas of the basal ganglia (ATAG atlas) (Keuken et al., 2017) and non-linearly registered to each subject using ANTs 3.0 (http://stnava.github.io/ANTs/), was used to map the SN to subject space, for each subject.

The diffusion data were pre-processed using MRTrix 3.0 (Tournier, Smith, et al., 2019). The pipeline for the diffusion preprocessing is described in (Boshkovski et al., 2020). Briefly, the diffusion images were first denoised (Veraart, Fieremans, et al., 2016; Veraart, Novikov, et al., 2016), corrected for Gibbs ringing artifacts (Kellner et al., 2016) and B1 field inhomogeneity. Then, the images were also corrected for motion (Andersson and Sotiropoulos, 2016) and inhomogeneity distortions (Andersson, Skare, et al., 2003) using the FSL's eddy and topup tools. The tractogram for each subject was reconstructed deterministically using multi-tissue constrained spherical deconvolution (Jeurissen, Tournier, et al., 2014) and anatomically-constrained tractography (Smith, Tournier, et al., 2012).

### 5.3.6 Myelin-weighted networks

The structural connectome for each subject was reconstructed using the Desikan-Killiany parcellation and the reconstructed tractograms. To each connection in the connectome, a weight was assigned. The weight was calculated as the median R1 value along the bundle of streamlines between each pair of regions. Then, for each individual connectome, we kept only the connections that were present in at least 50% of the subjects (de Reus and van den Heuvel, 2013).

### 5.3.7 PLS analysis

The partial least squares (PLS) analysis is a multivariate statistical technique used to relate two sets of variables to each other (Abdi, 2010; Krishnan et al., 2011; McIntosh and Mišić, 2013; McIntosh and Lobaugh, 2004). The first set of variables represents the weights of the connections while the second set represents the experiment design. In this study we used mean-centering PLS to compare the HC group with PD groups (HC vs. PD; HC vs. PDnonRBD; HC vs. PDRBD) and behavioral PLS to relate connectivity pattern with MDS-UPDRS III score for the PD group. The PLS analysis tries to find linear combinations of variables in both sets that maximally covary with each other. For the mean-centering, we aim to find an optimal contrast between HC and PD groups, as well as connectivity patterns that maximally covary with this contrast. On the other hand, for the behavioral PLS, we aim to find a relationship between the connectivity pattern and behavioral (clinical) score, in our case the MDS-UPDRS III score. In this analysis the mean-centered and behavioral data matrices are subjected to singular value decomposition (SVD), that outputs a mutually orthogonal latent variables (LVs). The statistical significance of the LVs was estimated using 500 permutation tests. The permutation tests randomly reordered the subjects in the original data matrices while ignoring their group assignments. Then, from the permuted data matrices we calculated covariance matrices which then were subjected to SVD. As the singular values reflect the degree of the statistical relationship of the latent variables, the p-values were computed as a ratio of the number of times the singular values were greater than the singular values of the original covariance matrix. To check the reliability of each individual connection, a bootstrap resampling with 500 bootstraps was done. The participants (i.e., the rows) from the original data matrix were randomly resampled with replacement, while preserving the group assignment. Then, from the resampled data matrices, covariance matrices were calculated that were subjected to SVD as described before. From the bootstrap distribution a standard error was estimated for each connection which corresponds to the stability of the connection. Afterwards, a bootstrap ratio (BSR) was calculated for each connection, by dividing the connection's weight (from the singular vectors) with its bootstrap-estimated standard error. The BSR can be considered as a z-score when it has an approximately normal distribution (B. Efron and R. Tibshirani, 1986), which allows us to extract the most reliable connections by thresholding the BSR at values that correspond to the 99% confidence interval.

### 5.3.8 Connectivity ring analysis

Connectivity ring analysis (Mallio et al., 2015) was performed to assess the hypothesis that the connections emerging from the disease epicenters would show greater structural damage in the early stages of the disease. Here, 8 groups of nodes (4 subcortical: bilateral SN, NBM, hippocampus, amygdala, and 4 brainstem: medulla, pons, midbrain and LC) were considered as potential epicenter nodes from where the disease would spread. We chose these regions based on what has previously been reported in the literature (Pyatigorskaya, Yahia-Cherif, et al., 2021). For each potential epicenter, two sets of nodes, denoted as rings, were defined (Figure 5.1). The first ring consisted of nodes that were directly connected to one of the epicenter nodes, while the second ring was composed of nodes indirectly connected to the epicenter nodes through a node from the first ring. Then, for each subject we calculated the median R1 value of the connections for each of the rings. The median R1-value of the rings between the groups (PD and HC) was compared using ANCOVA while controlling for age and sex and corrected for multiple comparisons using false discovery rate (FDR).

## 5.4 Results

To assess the connectome differences between the PD and HC participants, we performed a PLS analysis (Figure 5.2). This type of analysis allowed us to identify the connections that maximally and reliably (BSR>2.56) covaried between the two groups. The mean-centered

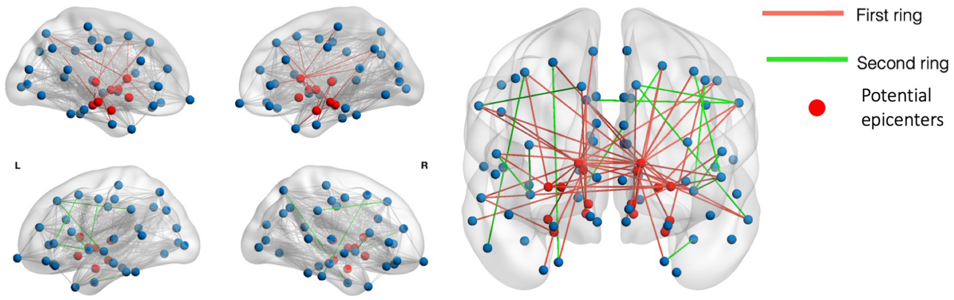

Figure 5.1 Example representation of the first and second rings. The nodes in red represent the potential epicenters. The connections in red are first ring connections, i.e., connections emerging from the epicenters, while the connections in green are second ring connections, i.e., connections that are connecting the first ring node with the second ring nodes.

PLS analysis showed that most of the connections that demonstrated a difference between HC and PD emerged from the basal ganglia (Figure 5.2). The highest number of affected connections (~80%) emerged from the SN. The identified multivariate connectivity pattern included connections between the SN and the bilateral precentral gyrus, postcentral gyrus, precuneus, superior frontal gyrus, caudate, midbrain, pons and medulla; between the LC and thalamus, and midbrain; and between the hippocampus and amygdala. After subdividing the PD data into PDnonRBD and PDRBD, and comparing them with the control group we obtained that the PDRBD exhibited more affected connections with a decreased R1 between the BG and cortex as well as more cortico-cortical connections.

To further examine how the disease progression affected the myelin content, we performed a connectivity ring analysis in which the connections were subdivided into two sets (Figure 5.3). Among the subcortical regions all four regions emerged as potential epicenters: the SN, the amygdala, the hippocampus and the NBM. The median R1 of the SN first ring was significantly decreased in the PD groups compared to controls (p=1.02x10-11, ANCOVA corrected for multiple comparisons). Significant decreases of the fist ring median R1 value were also obtained for the NBM (p = 6.98x10-11), amygdala (p=1.22x10-12), hippocampus (p = 0.0017). There was no significant difference between the HC and the PD groups in the second ring's median R1. Among the brainstem regions (midbrain, pons, medulla and LC), we only found a significant difference only for the midbrain's first ring median R1 between the HC and PD groups (p=0.046), and that relationship was only marginally significant.

To correlate these findings with clinical symptoms, we then examined the relationship of the myelin content with a motor clinical score using behavioral PLS (Figure 5.4). We found that the MDS-UPDRS part III correlates negatively with the identified multivariate connectivity

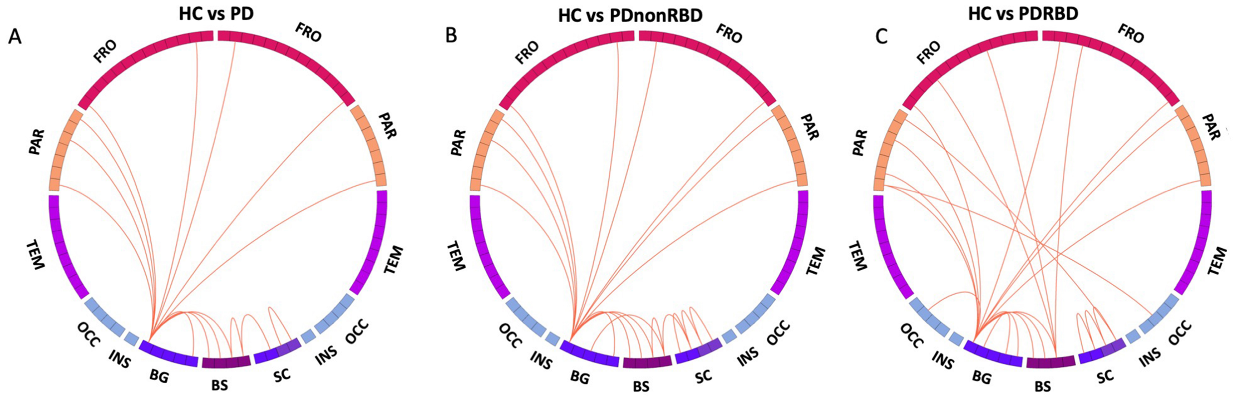

Figure 5.2 Connectogram of the multivariate connectivity pattern obtained with mean-centering PLS, composed of the connections that maximally covary between the groups. These connections showed decreased R1 in the PD groups compared to HC. Most of the connections associated with a significant HC/PD difference are emerging from the basal ganglia. FRO (Frontal lobe), PAR (Parietal lobe), TEM (Temporal lobe), OCC (Occipital lobe), SC (Subcortical regions including: amygdala, hippocampus, thalamus, and nucleus basalis of Meynert), BG (Basal ganglia), BS (Brain stem)

pattern (r=-0.85, p< 0.01). Six of the eight connections identified latent variable with the behavioral PLS analysis negatively covaried with MDS-UPDRS part III clinical score. The connections that negatively covaried with the MDS-UPDRS part III score were between the putamen and: precentral gyrus (BSR=2.66), superior parietal gyrus (BSR=3.05), and lateral occipital gyrus (BSR=2.75); as well as between the thalamus and paracentral lobule (BSR=2.9), and postcentral gyrus (BSR=2.75), and between the inferior temporal gyrus and superior parietal gyrus (BSR=2.64). There were 2 connections that positively covaried with the MDS-UPDRS part III score, between inferior parietal gyrus and temporal pole (BSR = -2.89), and between paracentral lobule and rostral anterior cingulate gyrus (BSR = -2.59).

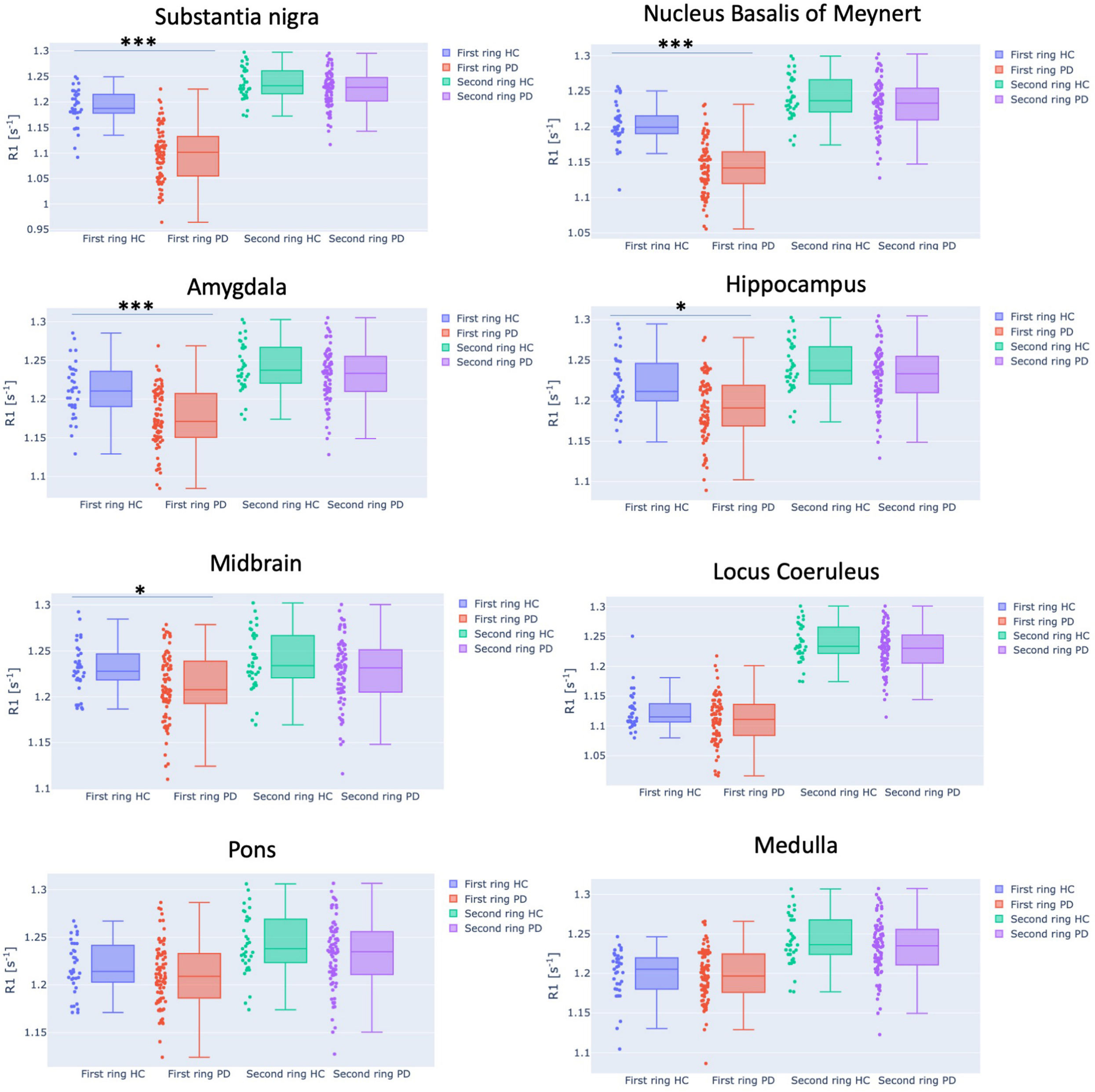
Substantia nigra
Nucleus Basalis of Meynert
Amygdala
Hippocampus
Midbrain
Locus Coeruleus
Pons
Medulla

Figure 5.3 Ring analysis of the 8 potential bilateral epicenter regions. A significant difference of the median R1 was found for the first rings of substantia nigra, hippocampus and amygdala, nucleus basalis of Meynert, and midbrain. No significant difference was observed for the second rings for all 7 potential epicenters. Dots in the bar plots represent the subject's median R1 of the first and second ring, respectively. The *** reflects a significant difference, with a $p<0.001$, of the median R1 of the ring, while * correspond to significant difference with a $p<0.05$, respectively

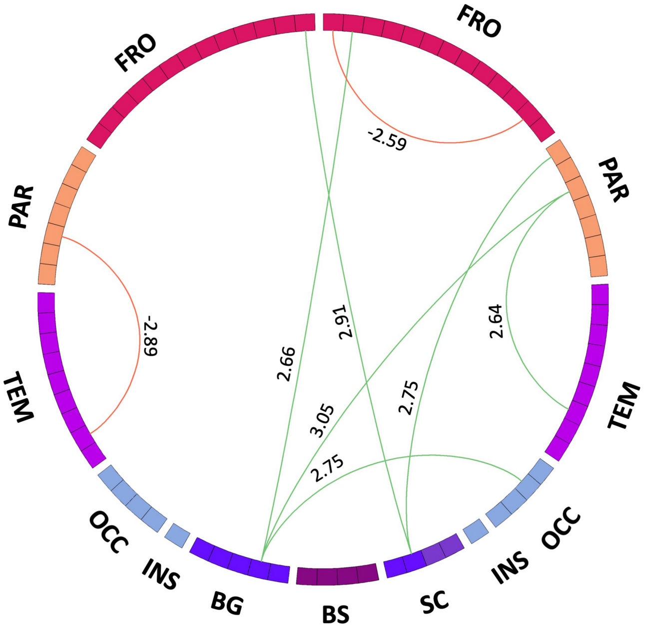

Figure 5.4 Multivariate connectivity pattern from the behavioral PLS that identifies the connection that maximally covary with the MDS-UPDRS-III. The red links represent positive covariance with the clinical score, while the green ones represent negative covariance. The number associated with each connection represents the BSR, which shows how reliably the connections contribute to the multivariate connectivity pattern. FRO (Frontal lobe), PAR (Parietal lobe), TEM (Temporal lobe), OCC (Occipital lobe), SC (Subcortical regions including: Amygdala, Hippocampus, Thalamus, and Nucleus Basalis of Meynert ), BG (Basal ganglia), BS (Brain stem).

## 5.5 Discussion

In this study we have shown that the myelin-weighted connectome was able to identify alterations of the myelin content along connections that were mostly emerging from the basal ganglia. Using a ring analysis, we have shown that the SN, NBM, amygdala, hippocampus, and midbrain have significantly decreased R1 of the connections directly emerging from them and could be confirmed as potential epicenters. Additionally, using behavioral PLS, we identified a subnetwork that maximally covaried with the MDS-UPDRS III motor score.

Most of the connections showing alterations in the myelin content between the PD and HC group were emerging from the SN, connecting it with the caudate nucleus, frontal and parietal cortical areas as well as the brainstem regions. This is in line with previous studies that have reported altered microstructural integrity along the nigrostriatal connections (Menke et al., 2010; Sharman et al., 2013; Zhang, Wu, et al., 2015) as well as altered functional connectivity of the cortical regions connected to SN (Meder et al., 2019). Moreover, according to the Braak and Del Tredici hypothesis, the regions with long projections that are unmyelinated or poorly myelinated are more susceptible to Lewy body pathology (Braak and Del Tredici, 2009). As the nigrostriatal connections are poorly myelinated, it is expected that the SN is more susceptible to disease pathology. Applying R1 to a poorly myelinated region would result in a reduced dynamic range for the myelin measurement, but the robustness and high resolution of the MP2RAGE pulse sequence produced reliable statistics (Maranzano et al., 2019; Shams et al., 2019). Other affected connections were identified between the LC and thalamus and LC and midbrain as well as between the hippocampus and amygdala, which is also in line with the pathological lesions in the LC as reported from a previous study that used neuromelanin-sensitive MRI (Pyatigorskaya, Yahia-Cherif, et al., 2021). Previous studies have reported that the PDRBD group has more severe cognitive dysfunction compared to the PDnonRBD group (Guo et al., 2018). This is in agreement with what has been observed when we compared the PDnonRBD and PDRBD relative to the HC group. According to the PLS analysis, the multivariate connectivity pattern did not vary much when we analyzed the whole PD group, compared to when we divided the patients into PDnonRBD and PDRBD group. However, the PDRBD pattern had more affected connections, including those between the SN and the cortex, the brainstem and cortex, as well as some cortico-cortical connections. As previously reported in the literature (Guo et al., 2018), as PDRBD is related to more severe cognitive dysfunction, we expected to identify more affected connections.

We then tested the hypothesis that most of the connections emerging from the potential disease epicenters would have decreased myelin content, compared to the healthy controls. Our results showed a significantly decreased median R1 along the connections emerging from the SN in the PD population compared to the control population. Previous imaging studies have already shown that the SN is an epicenter from where the disease spreads (Pyatigorskaya, Yahia-Cherif, et al., 2021; Zeighami et al., 2015; Zheng et al., 2019). Besides the SN, amygdala, hippocampus, NBM and the midbrain have also shown significantly reduced R1 in their first ring. This result is consistent with the alternative "top-down" model of PD progression for the PDnonRBD group, as reported in previous studies (Horsager et al., 2020; Pyatigorskaya, Yahia-Cherif, et al., 2021). On the other hand, previous studies have reported that the PDRBD follows the “bottom-up” model of disease progression. However, we did not observe significant differences of the first ring’s median R1 for the brainstem regions. This could be due to the fact that the whole brain tractography could not always reconstruct the fibers emerging from small structures such as the LC without anatomical priors on the fiber structure itself (Carandini et al., 2021; Schilling et al., 2020). Another possibility is that the brainstem’s larger structures, such as the pons and medulla, could be overrepresented with connections that are not affected, which may give misleading results.

Finally, using a behavioral PLS we identified a subnetwork of connections that maximally covaried with the MDS-UPDRS-III motor clinical score. Most of the identified connections negatively covaried with the motor clinical score and emerge from the putamen connecting it with the precentral and superior parietal gyrus. This is in line with the motor symptoms caused by the disease, because the putamen is linked to motor performance as has been shown previously (Redgrave et al., 2010). Other connections that also negatively covaried with the motor score were identified between the thalamus and the paracentral lobule and postcentral gyrus which is also in agreement with previous dMRI and fMRI studies (Akram et al., 2017; Sharman et al., 2013).

An important limitation to disclose is the unbalanced number of PDRBD and PDnonRBD patients. In the study we had a greater population of PDnonRBD compared to PDRBD, which could have driven the results when analyzing the whole PD population. In conclusion, the myelin-weighted connectome determined alteration in the myelin content in the PD patients especially in the basal ganglia network. Furthermore, the alterations of the myelin content along the connections emerging from the potential epicenters is in line with the “top-down” model of disease progression for PD patients without RBD. Further investigation is needed to validate that the alterations of the myelin content along the connections emerging from the small brainstem nuclei in PD patients with RBD follows the “bottom-up” model of disease progression.

## 5.6 Acknowledgements

This study was funded by grants from the Investissements d'Avenir, IAIHU-06 (Paris Institute of Neurosciences – IHU), ANR-11-INBS-0006, Fondation d'Entreprise EDF, Biogen Inc., Fondation Thérèse and René Planiol, Fondation Saint Michel, Unrestricted support for Research on Parkinson's disease from Energipole (M. Mallart), M.Villain and Société Française de Médecine Esthétique (M. Legrand). Montreal Heart Institute Foundation (NS), Canadian Open Neuroscience Platform (Brain Canada PSG) (NS), Quebec Bio-Imaging Network (NS, 8436-0501), Natural Science and Engineering Research Council of Canada (NS, 2016-06774) Fonds de Recherche du Québec (NS, FRSQ 36759 and FRSQ 35250). MM was funded by the Wellcome Trust through a Sir Henry Wellcome Postdoctoral Fellowship [213722/Z/18/Z].

## 5.7 References

Abdi, H. (2010). Partial least squares regression and projection on latent structure regression (PLS Regression). *WIREs Computational Statistics*, *2*(1), 97–106.

Agosta, F., Canu, E., Stefanova, E., Sarro, L., Tomić, A., Špica, V., Comi, G., Kostić, V. S., & Filippi, M. (2014). Mild cognitive impairment in Parkinson's disease is associated with a distributed pattern of brain white matter damage. *Human Brain Mapping*, *35*(5), 1921–1929.

Akram, H., Wu, C., Hyam, J., Foltynie, T., Limousin, P., De Vita, E., Yousry, T., Jahanshahi, M., Hariz, M., Behrens, T., Ashburner, J., & Zrinzo, L. (2017). l-Dopa responsiveness is associated with distinctive connectivity patterns in advanced Parkinson's disease. *Movement Disorders*, *32*(6), 874–883.

Andersson, J. L., Skare, S., & Ashburner, J. (2003). How to correct susceptibility distortions in spin-echo echo-planar images: Application to diffusion tensor imaging. *NeuroImage*, *20*(2), 870–888.

Andersson, J. L., & Sotiropoulos, S. N. (2016). An integrated approach to correction for off-resonance effects and subject movement in diffusion MR imaging. *NeuroImage*, *125*, 1063–1078.

B. Efron, & R. Tibshirani. (1986). Bootstrap Methods for Standard Errors, Confidence Intervals, and Other Measures of Statistical Accuracy on JSTOR. *Statistical Science*, *1*(1), 54–75.

Baumeister, T. R., Kim, J. L., Zhu, M., & McKeown, M. J. (2019). White matter myelin profiles linked to clinical subtypes of Parkinson's disease. *Journal of Magnetic Resonance Imaging*, *50*(1), 164–174.

Boshkovski, T., Kocarev, L., Cohen-Adad, J., Mišić, B., Lehéricy, S., Stikov, N., & Mancini, M. (2020). The R1-weighted connectome: complementing brain networks with a myelin-sensitive measure. *Network Neuroscience*, 1–15.

Braak, H., & Del Tredici, K. (2009). *Neuroanatomy and Pathology of Sporadic Parkinson's Disease* (Vol. 201). Springer Berlin Heidelberg.

Braak, H., Del Tredici, K., Rüb, U., De Vos, R. A., Jansen Steur, E. N., & Braak, E. (2003). Staging of brain pathology related to sporadic Parkinson's disease. *Neurobiology of Aging*, *24*(2), 197–211.

Breydo, L., Wu, J. W., & Uversky, V. N. (2012). $\alpha$-Synuclein misfolding and Parkinson's disease.

Brundin, P., & Melki, R. (2017). Prying into the prion hypothesis for parkinson's disease. *Journal of Neuroscience*, *37*(41), 9808–9818.

Caeyenberghs, K., Metzler-Baddeley, C., Foley, S., & Jones, D. K. (2016). Dynamics of the human structural connectome underlying working memory training. *Journal of Neuroscience*, *36*(14), 4056–4066.

Carandini, T., Mancini, M., Bogdan, I., L Rae, C., W Barritt, A., Sethi, A., Harrison, N., Rashid, W., Scarpini, E., Galimberti, D., Bozzali, M., & Cercignani, M. (2021). Disruption of brainstem monoaminergic fibre tracts in multiple sclerosis as a putative mechanism for cognitive fatigue: a fixel-based analysis. *NeuroImage: Clinical*, *30*, 102587.

Dean, D. C., Sojkova, J., Hurley, S., Kecskemeti, S., Okonkwo, O., Bendlin, B. B., Theisen, F., Johnson, S. C., Alexander, A. L., & Gallagher, C. L. (2016). Alterations of myelin content in Parkinson's disease:a cross-sectional neuroimaging study. *PLoS ONE*, *11*(10).

de Reus, M. A., & van den Heuvel, M. P. (2013). Estimating false positives and negatives in brain networks. *NeuroImage*, *70*, 402–409.

Desikan, R. S., Ségonne, F., Fischl, B., Quinn, B. T., Dickerson, B. C., Blacker, D., Buckner, R. L., Dale, A. M., Maguire, R. P., Hyman, B. T., Albert, M. S., & Killiany, R. J. (2006). An automated labeling system for subdividing the human cerebral cortex on MRI scans into gyral based regions of interest. *NeuroImage*, *31*(3), 968–980.

Fischl, B. (2012). FreeSurfer. *NeuroImage*, *62*(2), 774–781.

Gallea, C., Ewenczyk, C., Degos, B., Welter, M.-L., Grabli, D., Leu-Semenescu, S., Valabregue, R., Berroir, P., Yahia-Cherif, L., Bertasi, E., Fernandez-Vidal, S., Bardinet, E., Roze, E., Benali, H., Poupon, C., François, C., Arnulf, I., Lehéricy, S., & Vidailhet, M. (2017). Pedunculopontine network dysfunction in Parkinson's disease with postural control and sleep disorders. *Movement Disorders*, *32*(5), 693–704.

García-Lorenzo, D., Longo-Dos Santos, C., Ewenczyk, C., Leu-Semenescu, S., Gallea, C., Quattrocchi, G., Pita Lobo, P., Poupon, C., Benali, H., Arnulf, I., Vidailhet, M., &

Lehericy, S. (2013). The coeruleus/subcoeruleus complex in rapid eye movement sleep behaviour disorders in Parkinson's disease. *Brain*, *136*(7), 2120–2129.

Guo, T., Guan, X., Zeng, Q., Xuan, M., Gu, Q., Huang, P., Xu, X., & Zhang, M. (2018). Alterations of brain structural network in Parkinson's disease with and without rapid eye movement sleep behavior disorder. *Frontiers in Neurology*, *9*(MAY), 11.

Hawkes, C. H., Del Tredici, K., & Braak, H. (2007). Parkinson's disease: a dual-hit hypothesis. *Neuropathology and Applied Neurobiology*, *33*(6), 599–614.

Hoehn, M. M., & Yahr, M. D. (1967). Parkinsonism: Onset, progression, and mortality. *Neurology*, *17*(5), 427–442.

Horsager, J., Andersen, K. B., Knudsen, K., Skjærbæk, C., Fedorova, T. D., Okkels, N., Schaeffer, E., Bonkat, S. K., Geday, J., Otto, M., Sommerauer, M., Danielsen, E. H., Bech, E., Kraft, J., Munk, O. L., Hansen, S. D., Pavese, N., Göder, R., Brooks, D. J., … Borghammer, P. (2020). Brain-first versus body-first Parkinson's disease: A multimodal imaging case-control study. *Brain*, *143*(10), 3077–3088.

Iglesias, J. E., Van Leemput, K., Bhatt, P., Casillas, C., Dutt, S., Schuff, N., Truran-Sacrey, D., Boxer, A., & Fischl, B. (2015). Bayesian segmentation of brainstem structures in MRI. *NeuroImage*, *113*, 184–195.

Iturria-Medina, Y., & Evans, A. C. (2015). On the central role of brain connectivity in neurodegenerative disease progression.

Jeurissen, B., Tournier, J. D., Dhollander, T., Connelly, A., & Sijbers, J. (2014). Multi-tissue constrained spherical deconvolution for improved analysis of multi-shell diffusion MRI data. *NeuroImage*, *103*, 411–426.

Jucker, M., & Walker, L. C. (2013). Self-propagation of pathogenic protein aggregates in neurodegenerative diseases.

Kamagata, K., Zalesky, A., Yokoyama, K., Andica, C., Hagiwara, A., Shimoji, K., Kumamaru, K. K., Takemura, M. Y., Hoshino, Y., Kamiya, K., Hori, M., Pantelis, C., Hattori, N., & Aoki, S. (2019). MR g-ratio-weighted connectome analysis in patients with multiple sclerosis. *Scientific Reports*, *9*(1), 1–13.

Karagulle Kendi, A. T., Lehericy, S., Luciana, M., Ugurbil, K., & Tuite, P. (2008). Altered diffusion in the frontal lobe in Parkinson disease. *American Journal of Neuroradiology*, *29*(3), 501–505.

Karakuzu, A., Boudreau, M., Duval, T., Boshkovski, T., Leppert, I. R., Cabana, J.-F., Gagnon, I., Beliveau, P., Pike, G. B., Cohen-Adad, J., & Stikov, N. (2020). qMRLab: Quantitative MRI analysis, under one umbrella. *Journal of Open Source Software*, *5*(53), 2343.

Kellner, E., Dhital, B., Kiselev, V. G., & Reisert, M. (2016). Gibbs-ringing artifact removal based on local subvoxel-shifts. *Magnetic Resonance in Medicine*, *76*(5), 1574–1581.

Keuken, M. C., Bazin, P. L., Backhouse, K., Beekhuizen, S., Himmer, L., Kandola, A., Lafeber, J. J., Prochazkova, L., Trutti, A., Schäfer, A., Turner, R., & Forstmann, B. U. (2017). Effects of aging on T1 , T2* , and QSM MRI values in the subcortex. *Brain Structure and Function*, *222*(6), 2487–2505.

Knudsen, K., Fedorova, T. D., Hansen, A. K., Sommerauer, M., Otto, M., Svendsen, K. B., Nahimi, A., Stokholm, M. G., Pavese, N., Beier, C. P., Brooks, D. J., & Borghammer, P. (2018). In-vivo staging of pathology in REM sleep behaviour disorder: a multimodality imaging case-control study. *The Lancet Neurology*, *17*(7), 618–628.

Krishnan, A., Williams, L. J., McIntosh, A. R., & Abdi, H. (2011). Partial Least Squares (PLS) methods for neuroimaging: A tutorial and review. *NeuroImage*, *56*(2), 455–475.

Luk, K. C., Kehm, V., Carroll, J., Zhang, B., O'Brien, P., Trojanowski, J. Q., & Lee, V. M. (2012). Pathological $\alpha$-synuclein transmission initiates Parkinson-like neurodegeneration in nontransgenic mice. *Science*, *338*(6109), 949–953.

Mallio, C. A., Schmidt, R., de Reus, M. A., Vernieri, F., Quintiliani, L., Curcio, G., Beomonte Zobel, B., Quattrocchi, C. C., & van den Heuvel, M. P. (2015). Epicentral disruption of structural connectivity in Alzheimer's disease. *CNS neuroscience & therapeutics*, *21*(10), 837–845.

Mancini, M., Giulietti, G., Dowell, N., Spanò, B., Harrison, N., Bozzali, M., & Cercignani, M. (2018). Introducing axonal myelination in connectomics: A preliminary analysis of g-ratio distribution in healthy subjects. *NeuroImage*, *182*, 351–359.

Mancini, M., Karakuzu, A., Cohen-Adad, J., Cercignani, M., Nichols, T. E., & Stikov, N. (2020). An interactive meta-analysis of MRI biomarkers of myelin. *eLife*, *9*.

Maranzano, J., Dadar, M., Rudko, D. A., De Nigris, D., Elliott, C., Gati, J. S., Morrow, S. A., Menon, R. S., Collins, D. L., Arnold, D. L., & Narayanan, S. (2019). Comparison of multiple sclerosis cortical lesion types detected by multicontrast 3T and 7T MRI. *American Journal of Neuroradiology*, *40*(7), 1162–1169.

Marques, J. P., Kober, T., Krueger, G., van der Zwaag, W., Van de Moortele, P. F., & Gruetter, R. (2010). MP2RAGE, a self bias-field corrected sequence for improved segmentation and T1-mapping at high field. *NeuroImage*, *49*(2), 1271–1281.

Masuda-Suzukake, M., Nonaka, T., Hosokawa, M., Oikawa, T., Arai, T., Akiyama, H., Mann, D. M. A., & Hasegawa, M. (2013). Prion-like spreading of pathological $\alpha$-synuclein in brain. *Brain*, *136*(4), 1128–1138.

McIntosh, A. R., & Mišić, B. (2013). Multivariate Statistical Analyses for Neuroimaging Data. *Annual Review of Psychology*, *64*(1), 499–525.

McIntosh, A. R., & Lobaugh, N. J. (2004). Partial least squares analysis of neuroimaging data: Applications and advances. *NeuroImage*, *23*(SUPPL. 1), S250–S263.

Meder, D., Herz, D. M., Rowe, J. B., Lehéricy, S., & Siebner, H. R. (2019). The role of dopamine in the brain - lessons learned from Parkinson's disease.

Menke, R., Jbabdi, S., Miller, K., Matthews, P., & Zarei, M. (2010). Connectivity-based segmentation of the substantia nigra in human and its implications in Parkinson's disease. *Neuroimage*.

O'Brien, K. R., Kober, T., Hagmann, P., Maeder, P., Marques, J., Lazeyras, F., Krueger, G., & Roche, A. (2014). Robust T1-Weighted Structural Brain Imaging and Morphometry at 7T Using MP2RAGE (D. Margulies, Ed.). *PLoS ONE*, *9*(6), e99676.

Pandya, S., Zeighami, Y., Freeze, B., Dadar, M., Collins, D. L., Dagher, A., & Raj, A. (2019). Predictive model of spread of Parkinson's pathology using network diffusion. *NeuroImage*, *192*, 178–194.

Pyatigorskaya, N., Mongin, M., Valabregue, R., Yahia-Cherif, L., Ewenczyk, C., Poupon, C., Debellemaniere, E., Vidailhet, M., Arnulf, I., & Lehéricy, S. (2016). Medulla oblongata damage and cardiac autonomic dysfunction in Parkinson disease. *Neurology*, *87*(24), 2540–2545.

Pyatigorskaya, N., Yahia-Cherif, L., Valabregue, R., Gaurav, R., Gargouri, F., Ewenczyk, C., Gallea, C., Fernandez-Vidal, S., Arnulf, I., Vidailhet, M., & Lehericy, S. (2021). Parkinson Disease Propagation Using MRI Biomarkers and Partial Least Squares Path Modeling. *Neurology*, *96*(3), e460–e471.

Redgrave, P., Rodriguez, M., Smith, Y., Rodriguez-Oroz, M. C., Lehericy, S., Bergman, H., Agid, Y., Delong, M. R., & Obeso, J. A. (2010). Goal-directed and habitual control in the basal ganglia: Implications for Parkinson's disease.

Schilling, K. G., Petit, L., Rheault, F., Remedios, S., Pierpaoli, C., Anderson, A. W., Landman, B. A., & Descoteaux, M. (2020). Brain connections derived from diffusion MRI tractography can be highly anatomically accurate—if we know where white matter pathways start, where they end, and where they do not go. *Brain Structure and Function*, *225*(8), 2387–2402.

Seeley, W. W., Crawford, R. K., Zhou, J., Miller, B. L., & Greicius, M. D. (2009). Neurodegenerative Diseases Target Large-Scale Human Brain Networks. *Neuron*, *62*(1), 42–52.

Shams, Z., Norris, D. G., & Marques, J. P. (2019). A comparison of in vivo MRI based cortical myelin mapping using T1w/T2w and R1 mapping at 3T (P. Lundberg, Ed.). *PLOS ONE*, *14*(7), e0218089.

Sharman, M., Valabregue, R., Perlbarg, V., Marrakchi-Kacem, L., Vidailhet, M., Benali, H., Brice, A., & Lehéricy, S. (2013). Parkinson's disease patients show reduced cortical-subcortical sensorimotor connectivity. *Movement Disorders*, *28*(4), 447–454.

Smith, R., Tournier, D., Calamante, F., & Connelly, A. (2012). Anatomically-constrained tractography: Improved diffusion MRI streamlines tractography through effective use of anatomical information. *NeuroImage*, *62*(3), 1924–1938.

Stüber, C., Morawski, M., Schäfer, A., Labadie, C., Wähnert, M., Leuze, C., Streicher, M., Barapatre, N., Reimann, K., Geyer, S., Spemann, D., & Turner, R. (2014). Myelin and iron concentration in the human brain: A quantitative study of MRI contrast. *NeuroImage*, *93*(P1), 95–106.

Tournier, J. D., Smith, R., Raffelt, D., Tabbara, R., Dhollander, T., Pietsch, M., Christiaens, D., Jeurissen, B., Yeh, C. H., & Connelly, A. (2019). MRtrix3: A fast, flexible and open software framework for medical image processing and visualisation. *NeuroImage*, *202*, 116137.

Tustison, N. J., Avants, B. B., Cook, P. A., Zheng, Y., Egan, A., Yushkevich, P. A., & Gee, J. C. (2010). N4ITK: Improved N3 bias correction. *IEEE Transactions on Medical Imaging*, *29*(6), 1310–1320.

Ubeda-Bañon, I., Saiz-Sanchez, D., De La Rosa-Prieto, C., & Martinez-Marcos, A. (2014). $\alpha$-Synuclein in the olfactory system in Parkinson's disease: Role of neural connections on spreading pathology.

van den Heuvel, M. P., Mandl, R. C. W., Stam, C. J., Kahn, R. S., Hulshoff Pol, H. E., Heuvel, v. d. M. P., Mandl, R. C. W., Stam, C. J., Kahn, R. S., & Pol, H. E. H. (2010). Aberrant Frontal and Temporal Complex Network Structure in Schizophrenia: A Graph Theoretical Analysis. *The Journal of Neuroscience*, *30*(47), 15915–15926.

Veraart, J., Fieremans, E., & Novikov, D. S. (2016). Diffusion MRI noise mapping using random matrix theory. *Magnetic Resonance in Medicine*, *76*(5), 1582–1593.

Veraart, J., Novikov, D. S., Christiaens, D., Ades-aron, B., Sijbers, J., & Fieremans, E. (2016). Denoising of diffusion MRI using random matrix theory. *NeuroImage*, *142*, 394–406.

Warren, J. D., Rohrer, J. D., Schott, J. M., Fox, N. C., Hardy, J., & Rossor, M. N. (2013). Molecular nexopathies: A new paradigm of neurodegenerative disease. *Trends in Neurosciences*, *36*(10), 561–569.

Yau, Y., Zeighami, Y., Baker, T. E., Larcher, K., Vainik, U., Dadar, M., Fonov, V. S., Hagmann, P., Griffa, A., Mišić, B., Collins, D. L., & Dagher, A. (2018). Network connectivity determines cortical thinning in early Parkinson's disease progression. *Nature Communications*, *9*(1), 1–10.

Zeighami, Y., Ulla, M., Iturria-Medina, Y., Dadar, M., Zhang, Y., Larcher, K. M. H., Fonov, V., Evans, A. C., Collins, D. L., & Dagher, A. (2015). Network structure of brain atrophy in de novo parkinson's disease. *eLife*, *4*(September 2015).

Zhan, W., Kang, G. A., Glass, G. A., Zhang, Y., Shirley, C., Millin, R., Possin, K. L., Nezamzadeh, M., Weiner, M. W., Marks, W. J., & Schuff, N. (2012). Regional alterations of brain microstructure in Parkinson's disease using diffusion tensor imaging. *Movement Disorders*, *27*(1), 90–97.

Zhang, Y., Wu, I.-W., Buckley, S., Coffey, C. S., Foster, E., Mendick, S., Seibyl, J., & Schuff, N. (2015). Diffusion tensor imaging of the nigrostriatal fibers in Parkinson's disease. *Movement Disorders*, *30*(9), 1229–1236.

Zheng, Y.-Q., Zhang, Y., Yau, Y., Zeighami, Y., Larcher, K., Misic, B., & Dagher, A. (2019). Local vulnerability and global connectivity jointly shape neurodegenerative disease propagation (H. Kennedy, Ed.). *PLOS Biology*, *17*(11), e3000495.

# CHAPTER 6 ARTICLE 3: THE MYELIN-WEIGHTED CONNECTOME: A NEW LOOK AT MUTIPLE SCLEROSIS

**Authors:** T. Boshkovski[1], A. Badji[1], P. Janjic[2], Lj. Kocarev[2], J. Cohen-Adad[1], A. Giorgio[3], N. De Stefano[3], B. Misic[4], N. Stikov[1]

**Affiliations:**

1. NeuroPoly Lab, Polytechnique Montreal, Montreal, Canada
2. Macedonian Academy of Sciences and Arts, Skopje, Macedonia
3. Department of Medicine, Surgery and Neuroscience, University of Siena, Siena, Italy
4. Montreal Neurological Institute, Montreal, Canada

This study has been presented at the 27th annual meeting of the International Society for Magnetic Resonance in Medicine (ISMRM).

## 6.1 Synopsis

Myelin imaging has yet to make its way into standard connectomics protocols. Myelin-specific MRI metrics are useful for the assessment of neurological conditions that affect white matter. In this study we compared the structural connectomes of multiple sclerosis (MS) patients and healthy controls. Magnetization transfer ratio was used as a myelin-specific metric computed along each tract (MTR-weighted connectome) and compared against the connectome weighted by fractional anisotropy (FA-weighted connectome). We then identified the connections that were reliably different between MS patients and controls, and found 100 connections that were unique to the MTR-weighted connectome and 62 connections that were unique to the FA-weighted connectome.

## 6.2 Introduction

Multiple sclerosis (MS) is a chronic, inflammatory and neurodegenerative disease characterized by pathological abnormal heterogeneity affecting the myelin sheath. Myelin is a lipid-rich dielectric material that wraps axons in the central nervous system to provide efficient transfer of information. To date, most of the connectomics studies used standard diffusion metrics, such as fractional anisotropy (FA) or number of streamlines (NOS), to evaluate the neurological disease. However, these metrics are not specific to myelin. FA is strongly affected by the underlying fiber organization (crossing fibers, "kissing" fibers, etc.), whereas the NOS is only a topological measure that is not specific to the underlying microstructure. Recent studies (Mancini, Giulietti, et al., 2018; van den Heuvel, Mandl, et al., 2010) have reported a range of brain network properties derived from myelin metrics, but it is unclear whether these novel metrics can shine a light on neurodegenerative diseases. In this abstract we introduce the MTR-weighted connectome to the study of demyelination in the normal appearing white matter in multiple sclerosis.

## 6.3 Data and Methods

42 MS patients (25 females, 17 males, mean age ± sd: 44.1±15) and 21 healthy subjects (HC) (11 females, 9 males, mean age ± sd: 39.5±10.6) participated in the present study.

Diffusion images were acquired on a 1.5T Philips Gyroscan with 32 gradient directions (2.5mm$^3$, bmax=1000, TR/TE = 8500/100ms). MTR was calculated from a pair of MT on/off images (1x1x3 mm, TR/TE = 35/10ms). Furthermore, a T1-weighted and a FLAIR image were acquired for segmentation of the white matter lesions in MS participants. The MS lesions were segmented using a fully automatic lesion growth algorithm (Schmidt et al., 2012) as implemented in the LST toolbox (www.statisticalmodelling.de/lst.html) for SPM.

For each subject, we reconstructed a connectome weighted by FA and MTR. The weight corresponds to the median FA and MTR along the tracts reconstructed using a deterministic tractography algorithm (Yeh, Verstynen, et al., 2013). The fibers passing through MS lesions were discarded from the analysis, as these tracts bias the analysis and make it more difficult to interpret the results in the normal-appearing white matter. The most consistent connections were selected from the connectivity matrices, and a consensus network was created for each subject. Thereafter, a partial least square (PLS) analysis (McIntosh and Lobaugh, 2004; Mišić, Betzel, et al., 2016) was applied on the consensus networks to evaluate the difference between HC and MS connectomes. The multivariate connectivity pattern was assessed by permutation tests (Mišić, Dunkley, et al., 2016) with 500 permutations by randomly reordering the subjects in the data matrix without preserving the subject's group assignments (i.e. MS and HC label was ignored). Then, a bootstrapping procedure (Mišić, Dunkley, et al., 2016) with 500 bootstraps was performed by randomly resampling the subjects with replacement, while preserving the original group assignment. The bootstrapping was used for weighting the contribution of individual connections. A bootstrap ratio (BSR) was computed by dividing the connection weight from the singular vector by its bootstrap-estimated standard error. The BSR was thresholded at values ± 2.58, (corresponding to the 99% confidence interval), to identify connections where there is a difference between MS patients and HC.

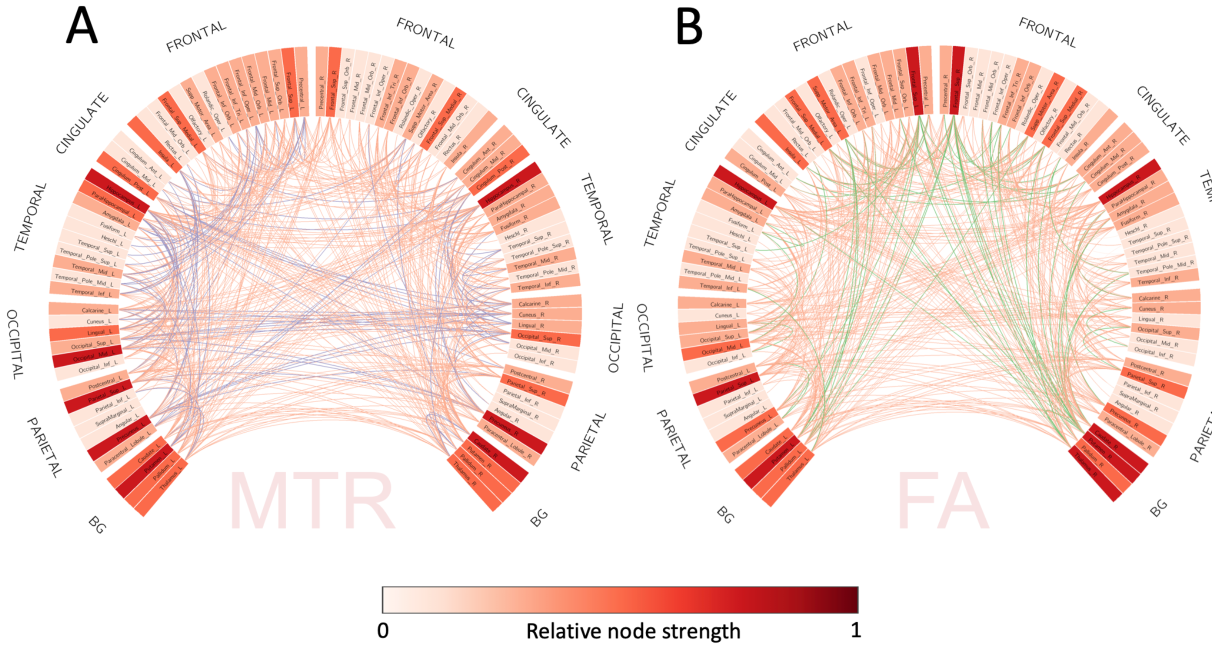

Figure 6.1 The MTR- and FA-weighted connectomes composed of connections that show a reliable difference (BSR<-2.58) between the HC and MS A) The MTR-weighted connectome identified 549 connections where there is a difference between MS and HC subjects. B) The FA-weighted connectome identified 511 connections with a reliable difference between MS and HC group. More than three-quarters of the connections are shared between the MTR- and the FA-weighted connectome (red). The connections in purple (A) and in green (B) correspond to the connections that are not shared between the two connectomes.

## 6.4 Results

For both connectomes MS mostly affected the central (hub) regions such as Precuneus, Superior Parietal gyrus, Superior Occipital gyrus, which have previously been established as hub regions in the literature (Kwon et al., 2017) (Figure 6.1). After the PLS analysis, we characterized the differences between the MTR and FA-weighted connectomes. The MTR-weighted connectome identified 549 connections where there is a reliable difference between MS and HC subjects (Figure 6.1A). The FA-weighted connectome identified 511 connections (Figure 6.2B). More than three-quarters of these connections are shared between the MTR- and the

FA-weighted connectome, but Figure 6.2 shows which connections are unique to each of the connectomes.

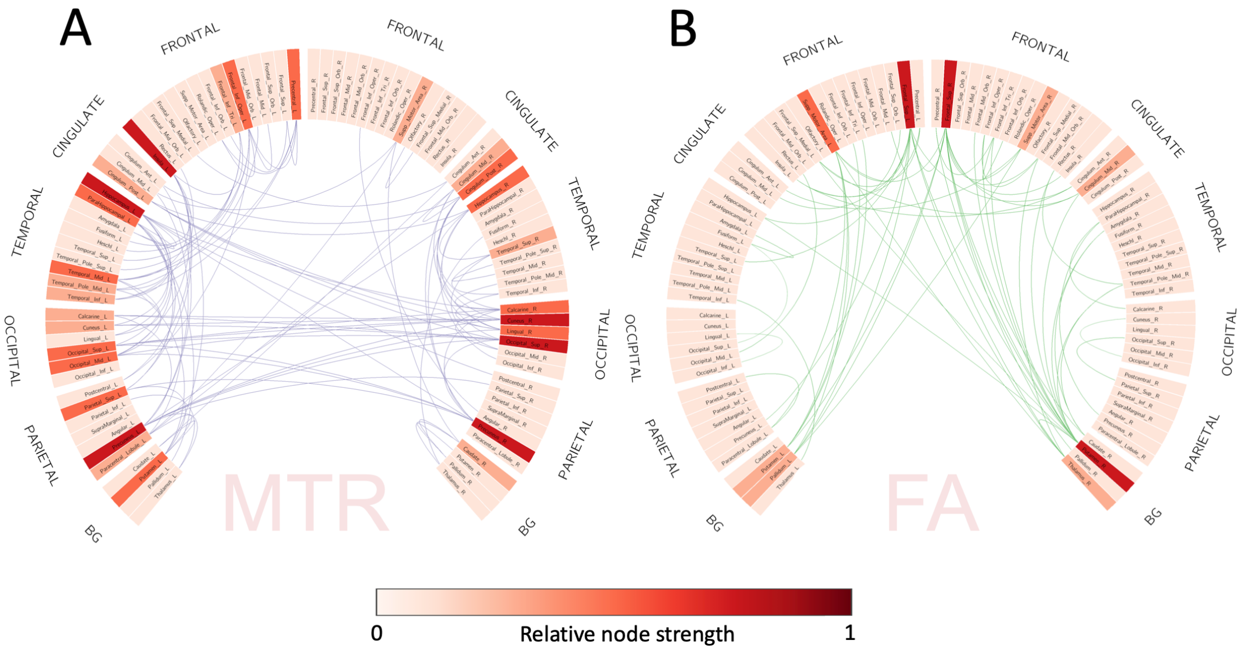

Figure 6.2 Network composed of unique connections that show a reliable difference between the HC and the MS group (A) only for MTR ($BSR_{MTR} < -2.58$ and $BSR_{FA} > -2.58$), and (B) only for FA ($BSR_{MTR} > -2.58$ and $BSR_{FA} < -2.58$).

## 6.5 Discussion and Conclusion

In this study, we demonstrate that the MTR-weighted connectome is different than the FA-weighted connectome. The MTR-weighted connectome identified more connections between regions involved in the processing of various functions, mainly visual, motor, and cognitive functions (Fleischer et al., 2019). On the other hand, the FA-weighted connectome identified more connections mainly between the basal ganglia and the frontal cortex that are mostly linked to motor function (Wen et al., 2012). Some of these differences might be due to the underlying fiber organization that alters the FA along a tract, while keeping the MTR relatively constant. To make sense of these differences, we plan to conduct a more comprehensive analysis that includes the patients' disability scores and a network dynamics model that can increase specificity to the conduction delays in the MTR-weighted connectome.

## 6.6 References

Fleischer, V., Radetz, A., Ciolac, D., Muthuraman, M., Gonzalez-Escamilla, G., Zipp, F., & Groppa, S. (2019). Graph theoretical framework of brain networks in multiple sclerosis: a review of concepts. *Neuroscience*, *403*, 35–53.

Kwon, H., Choi, Y.-H., Seo, S. W., & Lee, J.-M. (2017). Scale-integrated Network Hubs of the White Matter Structural Network. *Scientific reports*, *7*(1), 1–10.

Mancini, M., Giulietti, G., Dowell, N., Spanò, B., Harrison, N., Bozzali, M., & Cercignani, M. (2018). Introducing axonal myelination in connectomics: A preliminary analysis of g-ratio distribution in healthy subjects. *NeuroImage*, *182*, 351–359.

McIntosh, A. R., & Lobaugh, N. J. (2004). Partial least squares analysis of neuroimaging data: Applications and advances. *NeuroImage*, *23*(SUPPL. 1), S250–S263.

Mišić, B., Betzel, R., De Reus, M., Van Den Heuvel, M., Berman, M., McIntosh, A., & Sporns, O. (2016). Network-level structure-function relationships in human neocortex. *Cerebral Cortex*, *26*(7), 3285–3296.

Mišić, B., Dunkley, B. T., Sedge, P. A., Da Costa, L., Fatima, Z., Berman, M. G., Doesburg, S. M., McIntosh, A. R., Grodecki, R., Jetly, R. et al. (2016). Post-traumatic stress constrains the dynamic repertoire of neural activity. *Journal of neuroscience*, *36*(2), 419–431.

Schmidt, P., Gaser, C., Arsic, M., Buck, D., Förschler, A., Berthele, A., Hoshi, M., Ilg, R., Schmid, V. J., Zimmer, C. et al. (2012). An automated tool for detection of FLAIR-hyperintense white-matter lesions in multiple sclerosis. *Neuroimage*, *59*(4), 3774–3783.

van den Heuvel, M. P., Mandl, R. C. W., Stam, C. J., Kahn, R. S., Hulshoff Pol, H. E., Heuvel, v. d. M. P., Mandl, R. C. W., Stam, C. J., Kahn, R. S., & Pol, H. E. H. (2010). Aberrant Frontal and Temporal Complex Network Structure in Schizophrenia: A Graph Theoretical Analysis. *The Journal of Neuroscience*, *30*(47), 15915–15926.

Wen, X., Yao, L., Fan, T., Wu, X., & Liu, J. (2012). The spatial pattern of basal ganglia network: A resting state fMRI study. *2012 ICME International Conference on Complex Medical Engineering (CME)*, 43–46.

Yeh, F.-C., Verstynen, T. D., Wang, Y., Fernández-Miranda, J. C., & Tseng, W.-Y. I. (2013). Deterministic diffusion fiber tracking improved by quantitative anisotropy. *PloS one*, *8*(11), e80713.

# CHAPTER 7 GENERAL DISCUSSION

This manuscript aimed to improve the standard model of structural brain connectivity by complementing it with a myelin-sensitive measure producing the so-called myelin-weighted connectome as presented in Chapter 4. The myelin-weighted connectome provides complementary information in terms of strength distribution and modular structure compared with the connectomes weighted with standard diffusion metrics (FA and NOS). Then we applied this framework of myelin-weighted connectome to study the alterations in the myelin content in Parkinson's disease and multiple sclerosis. Using this framework we were able to identify connection-wise changes in the myelin content in subjects with PD and MS.

## 7.1 The choice of T1 mapping sequence to estimate the myelin

T1 mapping plays a vital role in qMRI, particularly for applications that focus on the assessment of myelin content. Given the importance of T1 mapping in these endeavours, it is worth noting that there are a variety of options available for generating T1 maps (MP2RAGE, Inversion Recovery (IR), Variable Flip Angle (VFA)), each with its own benefits and pitfalls. In Chapter 4 and Chapter 5 we used the MP2RAGE sequence. The reason for choosing the MP2RAGE pulse sequence is because it is capable of self-bias correction of the B0 and B1 magnetic fields, which is an improvement over the VFA technique, which is more sensitive to B1 field inhomogeneities. MP2RAGE has demonstrated a high degree of reproducibility in estimating T1 values in the brain (Voelker et al., 2016) and also provides similar results as IR, which is considered a gold standard. However, there are some limitations to consider when implementing MP2RAGE acquisitions. To achieve high reproducibility in the estimation of a T1 map, it is important to use a single pre-calculated dictionary. Moreover, B1 inhomogeneities may be present to such a degree as to require a separate B1 map for correction (Haast et al., 2018; Marques and Gruetter, 2013). Finally, the equations underlying the MP2RAGE pulse sequence presuppose mono-exponential longitudinal relaxation, which has been shown to provide substandard estimates of the long T1 component for a biexponential relaxation model (Rioux et al., 2016). Also, a big advantage of the MP2RAGE sequence is the relatively short acquisition time ( $7min$), compared to the conventional IR sequence that requires long TR values on the order of 2 to 5 T1). This makes MP2RAGE feasible for a clinical application and a good way to provide an estimate of the myelin content.

## 7.2 The choice of myelin-sensitive metric

There is an ongoing debate regarding the choice of a myelin measure that is both sensitive and specific enough to adequately represent the true nature of brain tissue microstructure. Despite the vast number of MRI measures employed to assess myelin content, according to a recent meta-analysis (Mancini, Karakuzu, et al., 2020) it is difficult to tell them apart. The cited meta-analysis examined 43 published quantitative validation studies to assess differences in myelin quantification with regard to histology data. For the purposes of this thesis, the most important observation is that MT- and relaxometry-based measures appear to be superior to those derived from diffusion imaging. The authors point out, however, that a majority of the measures demonstrate large prediction intervals, which is not consistent with them being robust biomarkers of myelin content. In light of these results, it may be worth considering an alternative focus for these MRI measures. Recent work has shown potential for the use of multiple MR parameters for the characterization of various types of pathophysiology. Granziera et al. (Granziera et al., 2015) found that T1, $T2^*$, and MTR could be used to infer information regarding the pathological substrate of mild cognitive impairment. Similarly, Lommers et al. (Lommers et al., 2019) used MT, $R2^*$, and R1 to assess the microstructure of normal appearing brain tissue in MS. Thus, the most useful approach to evaluating brain tissue microstructure may not be to identify a single "best" metric, but, rather, to combine information from more than one. In this sense, a structural network model alone may not be sufficient for evaluating pathological changes in tissue microstructure. This can be illustrated by the fact that several qMRI techniques, such as MT, relaxometry, and myelin water imaging may also be used to estimate the conduction velocity and conduction delays along an axon. By incorporating this information into the connectome, a more complete network model can be established.

## 7.3 Sensitivity of the myelin weighted-connectome to the methodology parameters

*In vivo* investigations of connections within the brain are inherently indirect in that they must depend upon models and inference because they are not capable of directly measuring a specific quantity. As a result, they tend to be more prone to errors (Sotiropoulos and Zalesky, 2019). Connectome reconstruction can be affected by multiple factors, such as image acquisition parameters, node parcellation, fiber tracking algorithms, and edge quantification. To date, there is no single methodological choice that can be considered "best" for all analyses and cohorts. The ultimate methodological choice for any study will be some trade-off that is deemed to work best for the particular task at hand. As far as data acquisition, better data may improve connectome estimation by improving diffusion-to-axon mapping and reducing partial volume through higher SNR, increased spatial and angular resolution, and increased angular contrast when possible. Obtaining these improvements, however, must be weighted against other needs that may influence the choice of diffusion acquisition protocol. Node parcellation may be affected by variability in brain structure and function, within-region heterogeneity, and the scale and number of nodes chosen. When exploring fiber tracking algorithm options, one must consider various methods for mapping fiber orientations, as well as seeding strategy and stopping criteria. Given the vast number of options for each of these elements, the resultant connectomes may vary considerably. Edge quantification is also an important factor to consider. Options typically include streamline counts, metrics that reflect microstructural properties, or features that reflect tract macrostructure. Regardless of which option is chosen, none of them has been shown to directly provide an inter-regional measure of the number of axon connections. Thus, the choice is often made in the context of what is most appropriate for a given analysis. Despite the limitations of the methods involved in construction of the myelin-weighted connectome, and the structural connectome in general, it has the potential to be translated into a diagnostic tool that can identify the early pathological changes of many neurodegenerative and neuroinflammatory diseases. To do this, more validation on larger, normative datasets is necessary. Additionally, standardizing the methods involved in the creation of the myelin-weighted connectome will increase the reproducibility and repeatability, making it more robust. This can be more easily achieved by using open science practices, such as sharing imaging protocols, which will result in more standardized data.

## 7.4 Open science: a way to standardize neuroimaging and neuroscience research

To translate qMRI research into clinical practice, standardization is required. Most of the tools are developed in-house, making it hard to port them across sites. Recently, a number of open source tools were proposed that unify the methods for quantitative MRI processing. One of them is qMRLab, a software tool for data fitting, simulation and protocol optimization of qMRI. In addition to processing qMRI data, the idea of qMRLab is to create standard qMRI workflows that could potentially allow for a better translation of the qMRI methods in clinical practice. One of the major challenges for MR-based myelin imaging, and qMRI techniques in general, is the poor reproducibility across sites and MR vendors, which makes comparisons difficult (Stikov et al., 2019). In a recent challenge organized by the ISMRM reproducible research study group on the reproducibility of T1 mapping (http://rrsg2020.herokuapp.com/), it was shown that the reproducibility is higher when the acquisition protocols are shared between centers, compared to when they are not.

The idea of open science is not limited to sharing data and code. It also applies to the sharing of educational tools. Scientific conferences are an excellent tool for information sharing among researchers, but they can be prohibitive to some individuals due to their location or a lack of adequate funding and/or resources. In an effort to remedy this situation, I partnered with the ISMRM Educational Committee to develop a three-part series on DWI called "Diffusion Without Equations" that later resulted in an interactive educational course on diffusion MRI that is freely available from the ISMRM website. For the second part blog, I built an animation that enables the user to visualize the diffusion process by selecting various parameter options, such as the gradient strength, gradient duration, and diffusion coefficient. The user may also choose to capture the diffusion-weighted signal with either 180°pulses (spin echo) or without (gradient echo). Once the parameters have been set, the user can view a simulation of how the selected parameters affect the diffusion process. In a follow-up blog post entitled "...and now for some equations: An interactive course on diffusion MRI", I coordinated with experts on diffusion imaging to provide instructive video tutorials that coincide with an interactive quiz. The user has the option to either view the full tutorial videos or navigate through them by answering a series of questions about diffusion MRI. In this way, the users have access to information from leading experts in the field of MRI that is traditionally reserved for those who are able to attend a conference in person. Thus, by making a concerted effort in multiple aspects of scientific research, including, but not limited to, data and code sharing, open source tools, reproducibility efforts, and educational opportunities, we can build a stronger and more adept scientific community that works together to confront the challenges facing us all.

# CHAPTER 8 CONCLUSION

The myelin-weighted connectome can be seen as a powerful tool to uncover the nature of neurodegenerative/neuroinflammatory diseases. It provides biologically more meaningful information compared to the standard diffusion-based measures that are not specific to the underlying microstructure. Therefore, the general objective of this dissertation was to improve the standard model of structural connectivity, which generally uses measures such as FA and NOS to weight the connectome, by complementing it with a myelin sensitive MRI measure that could provide information about the myelin content.

The first study in this dissertation was focused on complementing the structural connectome with the longitudinal relaxation rate as a myelin-sensitive measure. We showed that the R1-weighted connectome provides complementary information compared to the standard diffusion-derived metrics (NOS and FA). However, the limitation of this study was the small sample size, which might affect the results to a certain extent. This study opens a door for future studies to complement the connectome with more biologically grounded measures, such as the axon diameter.

After establishing that the myelin-weighted connectome provides complementary information to the standard diffusion-derived metrics, we used this approach to investigate the relationship between Parkinson's disease and myelination. We found that the myelin-weighted connectome could identify changes in the myelin content in PD. These changes follow the prion-like spreading of misfolded $\alpha-$syn proteins, and is consistent with a spread from the cortex to the rest of the brain. To validate that the myelin changes are following a topological sequence, as is the case with the gray matter atrophy, future studies should focus on the longitudinal changes in myelin content.

Last but not least, we also investigated the MS-induced demyelination in normal appearing white matter through the lens of the myelin-weighted connectome. The difference from the previous two studies was that in this study the myelin-weighted connectome was weighted using the magnetization transfer ratio (MTR). This study, using a multivariate statistical technique (PLS), was able to identify the demyelinated connections. However, the limitation of this study was that the connectome was reconstructed from a tractogram obtained from DTI data and therefore inherits the limitations of DTI. Future work could concentrate on relating the myelin changes and the network topological measures with clinical scores specific to MS.

# REFERENCES

Achard, S., & Bullmore, E. (2007). Efficiency and Cost of Economical Brain Functional Networks. *PLoS Computational Biology*, *3*(2), 17.

Achard, S., Salvador, R., Whitcher, B., Suckling, J., & Bullmore, E. (2006). A Resilient, Low-Frequency, Small-World Human Brain Functional Network with Highly Connected Association Cortical Hubs. *Journal of Neuroscience*, *26*(1).

Agosta, F., Canu, E., Stojković, T., Pievani, M., Tomić, A., Sarro, L., Dragašević, N., Copetti, M., Comi, G., Kostić, V., & Filippi, M. (2013). The topography of brain damage at different stages of Parkinson's disease. *Human Brain Mapping*, *34*(11), 2798–2807.

Akbar, N., Giorgio, A., Till, C., Sled, J., Doesburg, S., De Stefano, N., & Banwell, B. (2016). Alterations in Functional and Structural Connectivity in Pediatric-Onset Multiple Sclerosis. *PloS One*, *11*(1), 0145906.

Argyridis, I., Li, W., Johnson, G. A., & Liu, C. (2014). Quantitative magnetic susceptibility of the developing mouse brain reveals microstructural changes in the white matter. *Neuroimage*, *88*, 134–142.

Azevedo, F. A., Carvalho, L. R., Grinberg, L. T., Farfel, J. M., Ferretti, R. E., Leite, R. E., Filho, W. J., Lent, R., & Herculano-Houzel, S. (2009). Equal numbers of neuronal and nonneuronal cells make the human brain an isometrically scaled-up primate brain. *Journal of Comparative Neurology*, *513*(5), 532–541.

Barkovich, A. J. (2000). Concepts of myelin and myelination in neuroradiology. *American Journal of Neuroradiology*, *21*(6), 1099–1109.

Basinger, H., & Hogg, J. P. (2020). Neuroanatomy, brainstem. *StatPearls [Internet]*.

Basser, P. J., Mattiello, J., & LeBihan, D. (1994a). Estimation of the effective self-diffusion tensor from the NMR spin echo. *Journal of Magnetic Resonance, Series B*, *103*(3), 247–254.

Basser, P. J., Mattiello, J., & LeBihan, D. (1994b). MR diffusion tensor spectroscopy and imaging. *Biophysical journal*, *66*(1), 259–267.

Basser, P. J., Pajevic, S., Pierpaoli, C., Duda, J., & Aldroubi, A. (2000). In vivo fiber tractography using DT-MRI data. *Magnetic resonance in medicine*, *44*(4), 625–632.

Bells, S., Cercignani, M., Deoni, S., Assaf, Y., Pasternak, O., Evans, C., Leemans, A., & Jones, D. (2011). Tractometry–comprehensive multi-modal quantitative assessment of white matter along specific tracts. *Proc. ISMRM*, *678*, 1.

Bloch, F. (1946). Nuclear induction. *Physical review*, *70*(7-8), 460.

Brown, R. W., Cheng, Y.-C. N., Haacke, E. M., Thompson, M. R., & Venkatesan, R. (2014). *Magnetic resonance imaging: physical principles and sequence design*. John Wiley & Sons.

Bullmore, E., & Sporns, O. (2012). The economy of brain network organization. *Nature Reviews Neuroscience*, *13*(5), 336–349.

Bullmore, E., & Sporns, O. (2009). Complex brain networks: graph theoretical analysis of structural and functional systems. *Nature Reviews. Neuroscience*, *10*(3), 186–198.

By, S., Xu, J., Box, B. A., Bagnato, F. R., & Smith, S. A. (2017). Application and evaluation of NODDI in the cervical spinal cord of multiple sclerosis patients. *NeuroImage: Clinical*, *15*, 333–342.

Campbell, J. S. W., & Pike, G. B. (2019). Diffusion magnetic resonance imaging. In R. Narayan (Ed.), *Encyclopedia of biomedical engineering* (pp. 505–518). Elsevier.

Canu, E., Agosta, F., Sarasso, E., Volontè, M., Basaia, S., Stojkovic, T., Stefanova, E., Comi, G., Falini, A., Kostic, V., Gatti, R., & Filippi, M. (2015). Brain structural and functional connectivity in Parkinson's disease with freezing of gait. *Human Brain Mapping*, *36*(12), 5064–5078.

Cao, M., Huang, H., & He, Y. (2017). Developmental connectomics from infancy through early childhood. *Trends in neurosciences*, *40*(8), 494–506.

Carr, H. Y., & Purcell, E. M. (1954). Effects of diffusion on free precession in nuclear magnetic resonance experiments. *Physical review*, *94*(3), 630.

Catani, M., & Ffytche, D. H. (2005). The rises and falls of disconnection syndromes. *Brain*, *128*(10), 2224–2239.

Chamberland, M., Raven, E. P., Genc, S., Duffy, K., Descoteaux, M., Parker, G. D., Tax, C. M., & Jones, D. K. (2019). Dimensionality reduction of diffusion mri measures for improved tractometry of the human brain. *NeuroImage*, *200*, 89–100.

Collin, G., & Van Den Heuvel, M. P. (2013). The ontogeny of the human connectome: development and dynamic changes of brain connectivity across the life span. *The Neuroscientist*, *19*(6), 616–628.

Conturo, T. E., Lori, N. F., Cull, T. S., Akbudak, E., Snyder, A. Z., Shimony, J. S., McKinstry, R. C., Burton, H., & Raichle, M. E. (1999). Tracking neuronal fiber pathways in the living human brain. *Proceedings of the National Academy of Sciences*, *96*(18), 10422–10427.

Corbin, C., Gupta, V., Villalon-Reina, J. E., Nir, T. M., Rashid, F. M., Thomopoulos, S. I., Jahanshad, N., & Thompson, P. M. (2017). White Matter Alterations In Parkinson's Disease Mapped Using Tractometry. *BioRxiv*.

Costabile, J. D., Alaswad, E., D'Souza, S., Thompson, J. A., & Ormond, D. R. (2019). Current applications of diffusion tensor imaging and tractography in intracranial tumor resection. *Frontiers in oncology*, *9*, 426.

Cousineau, M., Jodoin, P.-M., Garyfallidis, E., Côté, M.-A., Morency, F. C., Rozanski, V., Grand'Maison, M., Bedell, B. J., & Descoteaux, M. (2017). A test-retest study on Parkinson's PPMI dataset yields statistically significant white matter fascicles. *NeuroImage: Clinical*, *16*, 222–233.

Crooks, L., Hylton, N. M., Ortendahl, D. A., Posin, J. P., & Kaufman, L. (1987). The value of relaxation times and density measurements in clinical MRI. *Investigative radiology*, *22*(2), 158–169.

Daducci, A., Dal Palu, A., Lemkaddem, A., & Thiran, J.-P. (2013). A convex optimization framework for global tractography. *2013 IEEE 10th International Symposium on Biomedical Imaging*, 524–527.

Daducci, A., Dal Palù, A., Lemkaddem, A., & Thiran, J.-P. (2014). Commit: convex optimization modeling for microstructure informed tractography. *IEEE transactions on medical imaging*, *34*(1), 246–257.

Daianu, M., Jahanshad, N., Nir, T., Toga, A., Jack, C., Weiner, M., Thompson, f. t. A. D., M., P., & Initiative, A. D. N. (2013). Breakdown of Brain Connectivity Between Normal Aging and Alzheimer's Disease: A Structural k -Core Network Analysis. *Brain Connectivity*, *3*(4), 407–422.

Dayan, M., Monohan, E., Pandya, S., Kuceyeski, A., Nguyen, T. D., Raj, A., & Gauthier, S. A. (2016). Profilometry: a new statistical framework for the characterization of white matter pathways, with application to multiple sclerosis. *Human brain mapping*, *37*(3), 989–1004.

Dell'Acqua, F., & Tournier, J. (2017). Reconstructing fiber orientations with diffusion MRI. *NMR Biomed*.

Dobbing, J., & Sands, J. (1973). Quantitative growth and development of human brain. *Archives of disease in childhood*, *48*(10), 757–767.

Dubois, J., Dehaene-Lambertz, G., Kulikova, S., Poupon, C., Hüppi, P. S., & Hertz-Pannier, L. (2014). The early development of brain white matter: a review of imaging studies in fetuses, newborns and infants. *Neuroscience*, *276*, 48–71.

Duval, T., Stikov, N., & Cohen-Adad, J. (2016). Modeling white matter microstructure. *Functional neurology*, *31*(4), 217.

Eguíluz, V., Chialvo, D., Cecchi, G., Baliki, M., & Apkarian, A. (2005). Scale-Free Brain Functional Networks. *Physical Review Letters*, *94*(1), 018102.

Essayed, W. I., Zhang, F., Unadkat, P., Cosgrove, G. R., Golby, A. J., & O'Donnell, L. J. (2017). White matter tractography for neurosurgical planning: A topography-based review of the current state of the art. *NeuroImage: Clinical*, *15*, 659–672.

Ferizi, U. (2014). *Compartment models and model selection for in-vivo diffusion-MRI of human brain white matter* (Doctoral dissertation). UCL (University College London).

Fick, A. (1995). On liquid diffusion. *Journal of Membrane Science*, *100*(1), 33–38.

Fillard, P., Poupon, C., & Mangin, J.-F. (2009). A novel global tractography algorithm based on an adaptive spin glass model. *International conference on medical image computing and computer-assisted intervention*, 927–934.

Fleischer, V., Radetz, A., Ciolac, D., Muthuraman, M., Gonzalez-Escamilla, G., Zipp, F., & Groppa, S. (2019). Graph theoretical framework of brain networks in multiple sclerosis: a review of concepts. *Neuroscience*, *403*, 35–53.

Fortin, D., Aubin-Lemay, C., Boré, A., Girard, G., Houde, J.-C., Whittingstall, K., & Descoteaux, M. (2012). Tractography in the study of the human brain: a neurosurgical perspective. *Canadian journal of neurological sciences*, *39*(6), 747–756.

Goldsmith, D. R., Crooks, C. L., Walker, E. F., & Cotes, R. O. (2018). An update on promising biomarkers in schizophrenia. *Focus*, *16*(2), 153–163.

Granziera, C., Daducci, A., Donati, A., Bonnier, G., Romascano, D., Roche, A., Cuadra, M. B., Schmitter, D., Klöppel, S., Meuli, R. et al. (2015). A multi-contrast MRI study of microstructural brain damage in patients with mild cognitive impairment. *NeuroImage: Clinical*, *8*, 631–639.

Griffa, A., Baumann, P. S., Thiran, J.-P., & Hagmann, P. (2013). Structural connectomics in brain diseases. *Neuroimage*, *80*, 515–526.

Groeschel, S., Tournier, J.-D., Northam, G. B., Baldeweg, T., Wyatt, J., Vollmer, B., & Connelly, A. (2014). Identification and interpretation of microstructural abnormalities in motor pathways in adolescents born preterm. *NeuroImage*, *87*, 209–219.

Grussu, F., Schneider, T., Tur, C., Yates, R. L., Tachrount, M., Ianuş, A., Yiannakas, M. C., Newcombe, J., Zhang, H., Alexander, D. C. et al. (2017). Neurite dispersion: a new marker of multiple sclerosis spinal cord pathology? *Annals of clinical and translational neurology*, *4*(9), 663–679.

Guevara, P., Poupon, C., Rivière, D., Cointepas, Y., Descoteaux, M., Thirion, B., & Mangin, J.-F. (2011). Robust clustering of massive tractography datasets. *Neuroimage*, *54*(3), 1975–1993.

Haast, R. A., Ivanov, D., & Uludağ, K. (2018). The impact of correction on MP2RAGE cortical T 1 and apparent cortical thickness at 7 T. *Human brain mapping*, *39*(6), 2412–2425.

Hagmann, P., Cammoun, L., Gigandet, X., Meuli, R., Honey, C. J., Wedeen, V. J., & Sporns, O. (2008a). Mapping the structural core of human cerebral cortex. *PLoS Biology*, *6*(7), 159.

Hahn, E. L. (1950). Spin echoes. *Physical review*, *80*(4), 580.

Harkins, K., Xu, J., Dula, A., Li, K., Valentine, W., Gochberg, D., Gore, J., & Does, M. (2016). The microstructural correlates of T1 in white matter. *Magnetic resonance in medicine*, *75*(3), 1341–1345.

Heath, F., Hurley, S. A., Johansen-Berg, H., & Sampaio-Baptista, C. (2018). Advances in noninvasive myelin imaging. *Developmental Neurobiology*, *78*(2), 136–151.

Helms, G., Dathe, H., Kallenberg, K., & Dechent, P. (2008). High-resolution maps of magnetization transfer with inherent correction for RF inhomogeneity and T1 relaxation obtained from 3D FLASH MRI. *Magnetic Resonance in Medicine: An Official Journal of the International Society for Magnetic Resonance in Medicine*, *60*(6), 1396–1407.

Hemond, C. C., & Bakshi, R. (2018). Magnetic resonance imaging in multiple sclerosis. *Cold Spring Harbor perspectives in medicine*, *8*(5), a028969.

Henkelman, R. M., Huang, X., Xiang, Q.-S., Stanisz, G., Swanson, S. D., & Bronskill, M. J. (1993). Quantitative interpretation of magnetization transfer. *Magnetic resonance in medicine*, *29*(6), 759–766.

Henkelman, R., Stanisz, G., & Graham, S. (2001). Magnetization transfer in MRI: a review. *NMR in Biomedicine: An International Journal Devoted to the Development and Application of Magnetic Resonance In Vivo*, *14*(2), 57–64.

Hore, P. J. (2015). *Nuclear magnetic resonance*. Oxford University Press, USA.

Huang, H., Zhang, J., Van Zijl, P. C., & Mori, S. (2004). Analysis of noise effects on DTI-based tractography using the brute-force and multi-ROI approach. *Magnetic Resonance in Medicine: An Official Journal of the International Society for Magnetic Resonance in Medicine*, *52*(3), 559–565.

Innocenti, G. M., Dyrby, T. B., Girard, G., St-Onge, E., Thiran, J.-P., Daducci, A., & Descoteaux, M. (2019). Topological principles and developmental algorithms might refine diffusion tractography. *Brain Structure and Function*, *224*(1), 1–8.

Jack Jr, C. R., Bernstein, M. A., Fox, N. C., Thompson, P., Alexander, G., Harvey, D., Borowski, B., Britson, P. J., L. Whitwell, J., Ward, C. et al. (2008). The Alzheimer's disease neuroimaging initiative (ADNI): MRI methods. *Journal of Magnetic Resonance Imaging: An Official Journal of the International Society for Magnetic Resonance in Medicine*, *27*(4), 685–691.

Jack Jr, C. R., & Holtzman, D. M. (2013). Biomarker modeling of Alzheimer's disease. *Neuron*, *80*(6), 1347–1358.

Jäkel, S., & Dimou, L. (2017). Glial cells and their function in the adult brain: a journey through the history of their ablation. *Frontiers in cellular neuroscience*, *11*, 24.

Jawabri, K. H., & Sharma, S. (2019). Physiology, Cerebral Cortex Functions. *StatPearls [Internet]*.

Jelescu, I., & Budde, M. (2017). Design and validation of diffusion MRI models of white matter. *Frontiers in physics*, *5*, 61.

Jensen, J. H., Helpern, J. A., Ramani, A., Lu, H., & Kaczynski, K. (2005). Diffusional kurtosis imaging: the quantification of non-gaussian water diffusion by means of magnetic resonance imaging. *Magnetic Resonance in Medicine: An Official Journal of the International Society for Magnetic Resonance in Medicine*, *53*(6), 1432–1440.

Jeurissen, B., Descoteaux, M., Mori, S., & Leemans, A. (2019). Diffusion MRI fiber tractography of the brain. *NMR in Biomedicine*, *32*(4), e3785.

Jeurissen, B., Leemans, A., Jones, D. K., Tournier, J.-D., & Sijbers, J. (2011). Probabilistic fiber tracking using the residual bootstrap with constrained spherical deconvolution. *Human brain mapping*, *32*(3), 461–479.

Jones, D. (2003). Determining and visualizing uncertainty in estimates of fiber orientation from diffusion tensor MRI. *Magnetic Resonance in Medicine: An Official Journal of the International Society for Magnetic Resonance in Medicine*, *49*(1), 7–12.

Jones, D. K. (2010a). Challenges and limitations of quantifying brain connectivity in vivo with diffusion MRI. *Imaging in Medicine*, *2*(3).

Jones, D. K. (2010b). *Diffusion MRI*. Oxford University Press.

Jones, D. K., Knösche, T. R., & Turner, R. (2013). White matter integrity, fiber count, and other fallacies: The do's and don'ts of diffusion MRI. *NeuroImage*, *73*, 239–254.

Jones, D. K., & Nilsson, M. (2014). Tractometry and the hunt for the missing link: a physicist perspective. *Microstructures Of Learning*, 38.

Kilby, P. M., Bolas, N. M., & Radda, G. K. (1991). 31P-NMR study of brain phospholipid structures in vivo. *Biochimica et Biophysica Acta (BBA)-Lipids and Lipid Metabolism*, *1085*(2), 257–264.

Kiselev, V. G. (2010). The cumulant expansion: an overarching mathematical framework for understanding diffusion NMR. *Diffusion MRI*, 152–168.

Kocevar, G., Stamile, C., Hannoun, S., Cotton, F., Vukusic, S., Durand-Dubief, F., & Sappey-Marinier, D. (2016). Graph theory-based brain connectivity for automatic classification of multiple sclerosis clinical courses. *Frontiers in neuroscience*, *10*, 478.

Koenig, S. H. (1991). Cholesterol of myelin is the determinant of gray-white contrast in MRI of brain. *Magnetic resonance in medicine*, *20*(2), 285–291.

Kreher, B., Mader, I., & Kiselev, V. (2008). Gibbs tracking: a novel approach for the reconstruction of neuronal pathways. *Magnetic Resonance in Medicine: An Official Journal of the International Society for Magnetic Resonance in Medicine*, *60*(4), 953–963.

Lazar, M., & Alexander, A. (2003). An error analysis of white matter tractography methods: synthetic diffusion tensor field simulations. *Neuroimage*, *20*(2), 1140–1153.

Le Bihan, D., Breton, E., Lallemand, D., Grenier, P., Cabanis, E., & Laval-Jeantet, M. (1986). MR imaging of intravoxel incoherent motions: application to diffusion and perfusion in neurologic disorders. *Radiology*, *161*(2), 401–407.

Lebel, C., Treit, S., & Beaulieu, C. (2019). A review of diffusion MRI of typical white matter development from early childhood to young adulthood. *NMR in Biomedicine*, *32*(4), e3778.

Lee, J., Hyun, J.-W., Lee, J., Choi, E.-J., Shin, H.-G., Min, K., Nam, Y., Kim, H. J., & Oh, S.-H. (2020). So you want to image myelin using MRI: an overview and practical guide for myelin water imaging. *Journal of Magnetic Resonance Imaging*.

Leech, R., & Sharp, D. (2014). The role of the posterior cingulate cortex in cognition and disease. *Brain : A Journal of Neurology*, *137*(Pt 1), 12–32.

Li, C., Huang, B., Zhang, R., Ma, Q., Yang, W., Wang, L., Wang, L., Xu, Q., Feng, J., Liu, L., Zhang, Y., & Huang, R. (2016). Impaired topological architecture of brain structural networks in idiopathic parkinson’s disease: a dti study. *Brain Imaging and Behavior*, 1–16.

Li, L., Rilling, J. K., Preuss, T. M., Glasser, M. F., & Hu, X. (2012). The effects of connection reconstruction method on the interregional connectivity of brain networks via diffusion tractography. *Human brain mapping*, *33*(8), 1894–1913.

Li, T.-Q., Yao, B., van Gelderen, P., Merkle, H., Dodd, S., Talagala, L., Koretsky, A. P., & Duyn, J. (2009). Characterization of T2* heterogeneity in human brain white matter. *Magnetic Resonance in Medicine: An Official Journal of the International Society for Magnetic Resonance in Medicine*, *62*(6), 1652–1657.

Li, W., Wu, B., Batrachenko, A., Bancroft-Wu, V., Morey, R. A., Shashi, V., Langkammer, C., De Bellis, M. D., Ropele, S., Song, A. W. et al. (2014). Differential developmental trajectories of magnetic susceptibility in human brain gray and white matter over the lifespan. *Human brain mapping*, *35*(6), 2698–2713.

Lodish, H., Berk, A., Zipursky, S. L., Matsudaira, P., Baltimore, D., & Darnell, J. (2000a). Intracellular ion environment and membrane electric potential. *Molecular cell biology. 4th edition*. WH Freeman.

Lodish, H., Berk, A., Zipursky, S. L., Matsudaira, P., Baltimore, D., & Darnell, J. (2000b). The action potential and conduction of electric impulses. *Molecular cell biology. 4th edition*. WH Freeman.

Lodygensky, G. A., Marques, J. P., Maddage, R., Perroud, E., Sizonenko, S. V., Hüppi, P. S., & Gruetter, R. (2012). In vivo assessment of myelination by phase imaging at high magnetic field. *Neuroimage*, *59*(3), 1979–1987.

Lommers, E., Simon, J., Reuter, G., Delrue, G., Dive, D., Degueldre, C., Balteau, E., Phillips, C., & Maquet, P. (2019). Multiparameter MRI quantification of microstructural tissue alterations in multiple sclerosis. *NeuroImage: Clinical*, *23*, 101879.

Lubetzki, C., Sol-Foulon, N., & Desmazières, A. (2020). Nodes of Ranvier during development and repair in the CNS. *Nature Reviews Neurology*, *16*(8), 426–439.

Mackay, A., Whittall, K., Adler, J., Li, D., Paty, D., & Graeb, D. (1994). In vivo visualization of myelin water in brain by magnetic resonance. *Magnetic resonance in medicine*, *31*(6), 673–677.

Madden, D. J., Bennett, I. J., & Song, A. W. (2009). Cerebral white matter integrity and cognitive aging: contributions from diffusion tensor imaging. *Neuropsychology review*, *19*(4), 415.

Mahlknecht, P., Hotter, A., Hussl, A., Esterhammer, R., Schocke, M., & Seppi, K. (2010). Significance of MRI in diagnosis and differential diagnosis of Parkinson's disease. *Neurodegenerative Diseases*, *7*(5), 300–318.

Mangin, J.-F., Fillard, P., Cointepas, Y., Le Bihan, D., Frouin, V., & Poupon, C. (2013). Toward global tractography. *Neuroimage*, *80*, 290–296.

Marques, J. P., & Gruetter, R. (2013). New Developments and Applications of the MP2RAGE Sequence-Focusing the Contrast and High Spatial Resolution R 1 Mapping. *PloS one*, *8*(7), e69294.

Mastrogiacomo, S., Dou, W., Jansen, J., & Walboomers, F. (2019). Magnetic resonance imaging of hard tissues and hard tissue engineered bio-substitutes. *Molecular imaging and biology*, *21*(6), 1003–1019.

Mchinda, S., Varma, G., Prevost, V. H., Le Troter, A., Rapacchi, S., Guye, M., Pelletier, J., Ranjeva, J.-P., Alsop, D. C., Duhamel, G. et al. (2018). Whole brain inhomogeneous magnetization transfer (ihMT) imaging: Sensitivity enhancement within a steady-state gradient echo sequence. *Magnetic resonance in medicine*, *79*(5), 2607–2619.

Michielse, S., Coupland, N., Camicioli, R., Carter, R., Seres, P., Sabino, J., & Malykhin, N. (2010). Selective effects of aging on brain white matter microstructure: a diffusion tensor imaging tractography study. *Neuroimage*, *52*(4), 1190–1201.

Miot-Noirault, E., Barantin, L., Akoka, S., & Le Pape, A. (1997). T2 relaxation time as a marker of brain myelination: experimental MR study in two neonatal animal models. *Journal of neuroscience methods*, *72*(1), 5–14.

Mito, R., Raffelt, D., Dhollander, T., Vaughan, D. N., Tournier, J.-D., Salvado, O., Brodtmann, A., Rowe, C. C., Villemagne, V. L., & Connelly, A. (2018). Fibre-specific white matter reductions in Alzheimer's disease and mild cognitive impairment. *Brain*, *141*(3), 888–902.

Mori, S. (2007). *Introduction to diffusion tensor imaging*. Elsevier.

Mori, S., Crain, B. J., Chacko, V. P., & Van Zijl, P. C. (1999). Three-dimensional tracking of axonal projections in the brain by magnetic resonance imaging. *Annals of Neurology: Official Journal of the American Neurological Association and the Child Neurology Society*, *45*(2), 265–269.

Moseley, M. (2002). Diffusion tensor imaging and aging: A review. *NMR in Biomedicine: An International Journal Devoted to the Development and Application of Magnetic Resonance In Vivo*, *15*(7-8), 553–560.

Moseley, M. E., Cohen, Y., Kucharczyk, J., Mintorovitch, J., Asgari, H., Wendland, M., Tsuruda, J., & Norman, D. (1990). Diffusion-weighted MR imaging of anisotropic water diffusion in cat central nervous system. *Radiology*, *176*(2), 439–445.

Nishimura, D. G. (2010). *Principles of magnetic resonance imaging*. Standford Univ.

Novikov, D. S., Kiselev, V. G., & Jespersen, S. N. (2018). On modeling. *Magnetic resonance in medicine*, *79*(6), 3172–3193.

Olde Dubbelink, K., Hillebrand, A., Stoffers, D., Deijen, J. B., Twisk, J., Stam, C., & Berendse, H. (2014). Disrupted brain network topology in Parkinson's disease: a longitudinal magnetoencephalography study. *Brain*, *137*(1), 197–207.

Panesar, S. S., Abhinav, K., Yeh, F.-C., Jacquesson, T., Collins, M., & Fernandez-Miranda, J. (2019). Tractography for surgical neuro-oncology planning: towards a gold standard. *neurotherapeutics*, *16*(1), 36–51.

Patel, K., Tobyne, S., Daria, B., Bireley, J., Smith, V., & Klawiter, E. (2016). Structural Disconnection Is Responsible for Increased Resting State Functional Connectivity in Multiple Sclerosis. *Neurology*, *86*(16).

Pestilli, F., Yeatman, J., Rokem, A., Kay, K., Takemura, H., & Wandell, B. (2014). Life: linear fascicle evaluation a new technology to study visual connectomes. *Journal of Vision*, *14*(10), 1122–1122.

Pievani, M., Filippini, N., Van Den Heuvel, M., Cappa, S., & Frisoni, G. (2014). Brain connectivity in neurodegenerative diseases—from phenotype to proteinopathy. *Nature Reviews Neurology*, *10*(11), 620.

Prasloski, T., Rauscher, A., MacKay, A. L., Hodgson, M., Vavasour, I. M., Laule, C., & Mädler, B. (2012). Rapid whole cerebrum myelin water imaging using a 3D GRASE sequence. *Neuroimage*, *63*(1), 533–539.

Purcell, E. M., Torrey, H. C., & Pound, R. V. (1946). Resonance absorption by nuclear magnetic moments in a solid. *Physical review*, *69*(1-2), 37.

Rapoport, M., van Reekum, R., & Mayberg, H. (2000). The role of the cerebellum in cognition and behavior: a selective review. *The Journal of neuropsychiatry and clinical neurosciences*, *12*(2), 193–198.

Reeves, C., Tachrount, M., Thomas, D., Michalak, Z., Liu, J., Ellis, M., Diehl, B., Miserocchi, A., McEvoy, A., Eriksson, S. et al. (2016). Combined ex vivo 9.4 t mri and quantitative histopathological study in normal and pathological neocortical resections in focal epilepsy. *Brain pathology*, *26*(3), 319–333.

Reisert, M., Mader, I., & Kiselev, V. (2009). Global reconstruction of neuronal fibres. *Proc. MICCAI Diffusion Modelling Workshop.*

Rheault, F., Houde, J.-C., & Descoteaux, M. (2017). Visualization, interaction and tractometry: Dealing with millions of streamlines from diffusion mri tractography. *Frontiers in neuroinformatics*, *11*, 42.

Rioux, J. A., Levesque, I. R., & Rutt, B. K. (2016). Biexponential longitudinal relaxation in white matter: characterization and impact on T1 mapping with IR-FSE and MP2RAGE. *Magnetic resonance in medicine*, *75*(6), 2265–2277.

Rubinov, M., & Sporns, O. (2010a). Complex network measures of brain connectivity: uses and interpretations. *NeuroImage*, *52*(3), 1059–1069.

Sala, S., Agosta, F., Pagani, E., Copetti, M., Comi, G., & Filippi, M. (2012). Microstructural changes and atrophy in brain white matter tracts with aging. *Neurobiology of aging*, *33*(3), 488–498.

Salvador, R., Suckling, J., Coleman, M., Pickard, J., Menon, D., & Bullmore, E. (2005). Neurophysiological architecture of functional magnetic resonance images of human brain. *Cerebral Cortex*, *15*(9), 1332–1342.

Savadjiev, P., Campbell, J. S., Descoteaux, M., Deriche, R., Pike, G. B., & Siddiqi, K. (2008). Labeling of ambiguous subvoxel fibre bundle configurations in high angular resolution diffusion MRI. *NeuroImage*, *41*(1), 58–68.

Sbardella, E., Tona, F., Petsas, N., & Pantano, P. (2013). DTI measurements in multiple sclerosis: evaluation of brain damage and clinical implications. *Multiple sclerosis international*, *2013.*

Schiavi, S., Ocampo-Pineda, M., Barakovic, M., Petit, L., Descoteaux, M., Thiran, J.-P., & Daducci, A. (2020). A new method for accurate in vivo mapping of human brain connections using microstructural and anatomical information. *Science Advances*, *6*(31), eaba8245.

Schlaier, J. R., Beer, A. L., Faltermeier, R., Fellner, C., Steib, K., Lange, M., Greenlee, M. W., Brawanski, A. T., & Anthofer, J. M. (2017). Probabilistic vs. deterministic fiber tracking and the influence of different seed regions to delineate cerebellar-thalamic fibers in deep brain stimulation. *European Journal of Neuroscience*, *45*(12), 1623–1633.

Schmierer, K., Scaravilli, F., Altmann, D. R., Barker, G. J., & Miller, D. H. (2004). Magnetization transfer ratio and myelin in postmortem multiple sclerosis brain. *Annals of neurology*, *56*(3), 407–415.

Shu, N., Liu, Y., Li, K., Duan, Y., Wang, J., Yu, C., Dong, H., Ye, J., & He, Y. (2011). Diffusion tensor tractography reveals disrupted topological efficiency in white matter structural networks in multiple sclerosis. *Cerebral Cortex*, *21*(11), 2565–2577.

Shu, N., Duan, Y., Xia, M., Schoonheim, M., Huang, J., Ren, Z., Sun, Z., Ye, J., Dong, H., Shi, F.-D., Barkhof, F., Li, K., & Liu, Y. (2016). Disrupted topological organization of structural and functional brain connectomes in clinically isolated syndrome and multiple sclerosis. *Scientific Reports*, *6*(1), 29383.

Skidmore, F., Korenkevych, D., Liu, Y., He, G., Bullmore, E., & Pardalos, P. (2011). Connectivity brain networks based on wavelet correlation analysis in parkinson fmri data. *Neuroscience Letters*, *499*(ue 1)).

Smith, R., Tournier, J., Calamante, F., & Connelly, A. (2015). SIFT2: Enabling dense quantitative assessment of brain white matter connectivity using streamlines tractography. *NeuroImage*, *119*, 338–351.

Smith, R. E., Tournier, J.-D., Calamante, F., & Connelly, A. (2013). SIFT: Spherical - deconvolution informed filtering of tractograms. *Neuroimage*, *67*, 298–312.

Smith, S. M., Jenkinson, M., Johansen-Berg, H., Rueckert, D., Nichols, T. E., Mackay, C. E., Watkins, K. E., Ciccarelli, O., Cader, M. Z., Matthews, P. M. et al. (2006). Tract-based spatial statistics: voxelwise analysis of multi-subject diffusion data. *Neuroimage*, *31*(4), 1487–1505.

Sotiropoulos, S. N., & Zalesky, A. (2019). Building connectomes using diffusion MRI: why, how and but. *NMR in Biomedicine*, *32*(4), e3752.

Sporns, O. (2011). *Networks of the brain*. The MIT Press.

Sporns, O. (2012). *Discovering the human connectome*. The MIT Press.

Sporns, O., Tononi, G., & Kötter, R. (2005). The human connectome: a structural description of the human brain. *PLoS Comput Biol*, *1*(4), e42.

Stam, C. (2004). Functional connectivity patterns of human magnetoencephalographic recordings: a 'small-world' network? *Neuroscience Letters*, *355*(ue 1)).

Stejskal, E. O., & Tanner, J. E. (1965). Spin diffusion measurements: spin echoes in the presence of a time-dependent field gradient. *The journal of chemical physics*, *42*(1), 288–292.

Stern, M., Braffman, B., Skolnick, B., Hurtig, H., & Grossman, R. (1989). Magnetic resonance imaging in Parkinson's disease and parkinsonian syndromes. *Neurology*, *39*(11), 1524–1524.

Stikov, N., Trzasko, J. D., & Bernstein, M. A. (2019). Reproducibility and the future of MRI research.

Stuss, D. T., & Alexander, M. P. (2000). Executive functions and the frontal lobes: a conceptual view. *Psychological research*, *63*(3), 289–298.

Tan, W.-Q., Yeoh, C.-S., Rumpel, H., Nadkarni, N., Lye, W.-K., Tan, E.-K., & Chan, L.-L. (2015). Deterministic tractography of the nigrostriatal-nigropallidal pathway in Parkinson's disease. *Scientific reports*, *5*(1), 1–6.

Tardif, C. L., Bedell, B. J., Eskildsen, S. F., Collins, D. L., & Pike, G. B. (2011). Quantitative magnetic resonance imaging of cortical multiple sclerosis pathology. *Multiple sclerosis international*, *2012*.

Theisen, F., Leda, R., Pozorski, V., Oh, J. M., Adluru, N., Wong, R., Okonkwo, O., Dean III, D. C., Bendlin, B. B., Johnson, S. C. et al. (2017). Evaluation of striatonigral connectivity using probabilistic tractography in Parkinson's disease. *NeuroImage: Clinical*, *16*, 557–563.

Toosy, A. T., Ciccarelli, O., Parker, G. J., Wheeler-Kingshott, C. A., Miller, D. H., & Thompson, A. J. (2004). Characterizing function–structure relationships in the human visual system with functional MRI and diffusion tensor imaging. *Neuroimage*, *21*(4), 1452–1463.

Torrey, H. (1956). Bloch equations with diffusion terms. *Physical review*, *104*(3), 563.

Tournier, J.-D., Mori, S., & Leemans, A. (2011). Diffusion tensor imaging and beyond. *Magnetic resonance in medicine*, *65*(6), 1532.

Tournier, J.-D., Calamante, F., & Connelly, A. (2012b). MRtrix: diffusion tractography in crossing fiber regions. *International journal of imaging systems and technology*, *22*(1), 53–66.

Tromp, D. (n.d.). *The diffusion tensor, and its relation to FA, MD, AD and RD* (tech. rep.) [type: dataset].

Van Kampen, N. (2007). Stochastic processes in physics and chemistry, 3rd edn Amsterdam. *The Netherlands: Elsevier.*

Vanderweyen, D. C., Theaud, G., Sidhu, J., Rheault, F., Sarubbo, S., Descoteaux, M., & Fortin, D. (2020). The role of diffusion tractography in refining glial tumor resection. *Brain Structure and Function*, *225*(4), 1413–1436.

van Gelderen, P., de Vleeschouwer, M. H., DesPres, D., Pekar, J., van Zijl, P. C., & Moonen, C. T. (1994). Water diffusion and acute stroke. *Magnetic resonance in medicine*, *31*(2), 154–163.

Varma, G., Duhamel, G., de Bazelaire, C., & Alsop, D. C. (2015). Magnetization transfer from inhomogeneously broadened lines: a potential marker for myelin. *Magnetic resonance in medicine*, *73*(2), 614–622.

Vemuri, P., & Jack, C. R. (2010). Role of structural MRI in Alzheimer's disease. *Alzheimer's research & therapy*, *2*(4), 1–10.

Voelker, M. N., Kraff, O., Brenner, D., Wollrab, A., Weinberger, O., Berger, M. C., Robinson, S., Bogner, W., Wiggins, C., Trampel, R. et al. (2016). The traveling heads: multicenter brain imaging at 7 Tesla. *Magnetic resonance materials in physics, biology and medicine*, *29*(3), 399–415.

Volkmar, F. R., & Volkmar, F. R. (2013). *Encyclopedia of autism spectrum disorders*. Springer New York, NY.

Waldman, A., Rees, J., Brock, C., Robson, M., Gatehouse, P., & Bydder, G. (2003). MRI of the brain with ultra-short echo-time pulse sequences. *Neuroradiology*, *45*(12), 887–892.

Wassermann, D., Makris, N., Rathi, Y., Shenton, M., Kikinis, R., Kubicki, M., & Westin, C.-F. (2016). The white matter query language: a novel approach for describing human white matter anatomy. *Brain Structure and Function*, *221*(9), 4705–4721.

Watts, D., & Strogatz, S. (1998). Collective dynamics of 'small-world' networks. *Nature*, *393*(6684), 440–442.

Wharton, S., & Bowtell, R. (2012). Fiber orientation-dependent white matter contrast in gradient echo MRI. *Proceedings of the National Academy of Sciences*, *109*(45), 18559–18564.

Wu, T., Wang, L., Chen, Y., Zhao, C., Li, K., & Chan, P. (2009). Changes of functional connectivity of the motor network in the resting state in Parkinson's disease. *Neuroscience Letters*, *460*, 6–10.

Yarnykh, V. L. (2012). Fast macromolecular proton fraction mapping from a single off-resonance magnetization transfer measurement. *Magnetic resonance in medicine*, *68*(1), 166–178.

Yeatman, J. D., Dougherty, R. F., Myall, N. J., Wandell, B. A., & Feldman, H. M. (2012). Tract profiles of white matter properties: automating fiber-tract quantification. *PloS one*, *7*(11), e49790.

Yeh, C.-H., Jones, D. K., Liang, X., Descoteaux, M., & Connelly, A. (2020). Mapping Structural Connectivity Using Diffusion MRI: Challenges and Opportunities. *Journal of Magnetic Resonance Imaging*.

Zhang, H., Schneider, T., Wheeler-Kingshott, C. A., & Alexander, D. C. (2012). NODDI: practical in vivo neurite orientation dispersion and density imaging of the human brain. *Neuroimage*, *61*(4), 1000–1016.

# APPENDIX A SUPPLEMENTARY MATERIALS FOR ARTICLE 1

## A.1 Quality assurance of the data

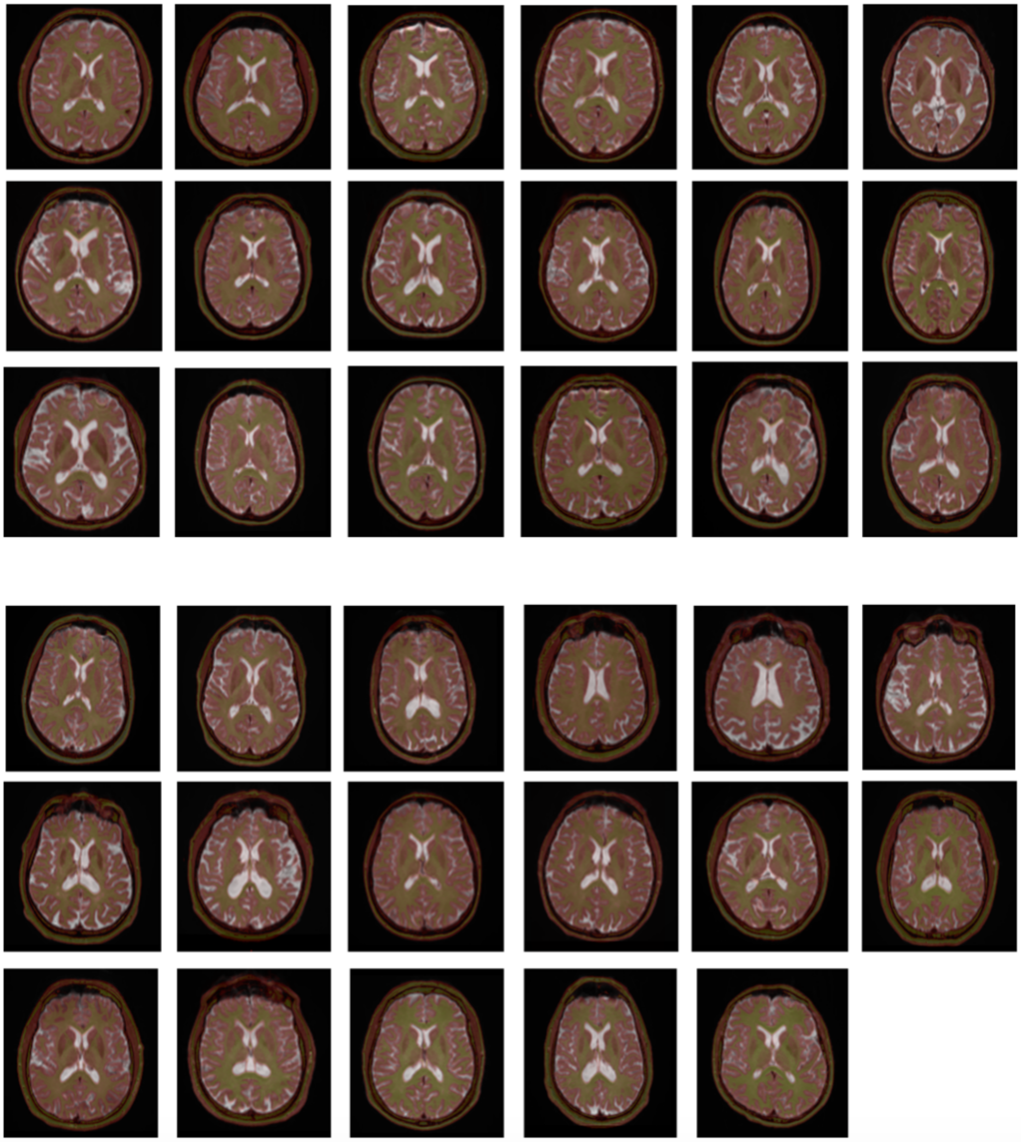

Figure A.1 Overlay of the registered T1-weighted volume (in red) over the mean b0 volume (in gray scale) for all subjects (representative slices).

## A.2 Additional Analyses

### A.2.1 Comparison with FA-weighted networks

As an additional comparison, we built a FA-weighted connectome. The procedure for obtaining the FA-weighted network is the same as for the R1-weighted connectome: we assigned to each connection the median FA value along the bundle of streamlines connecting pairs of regions.

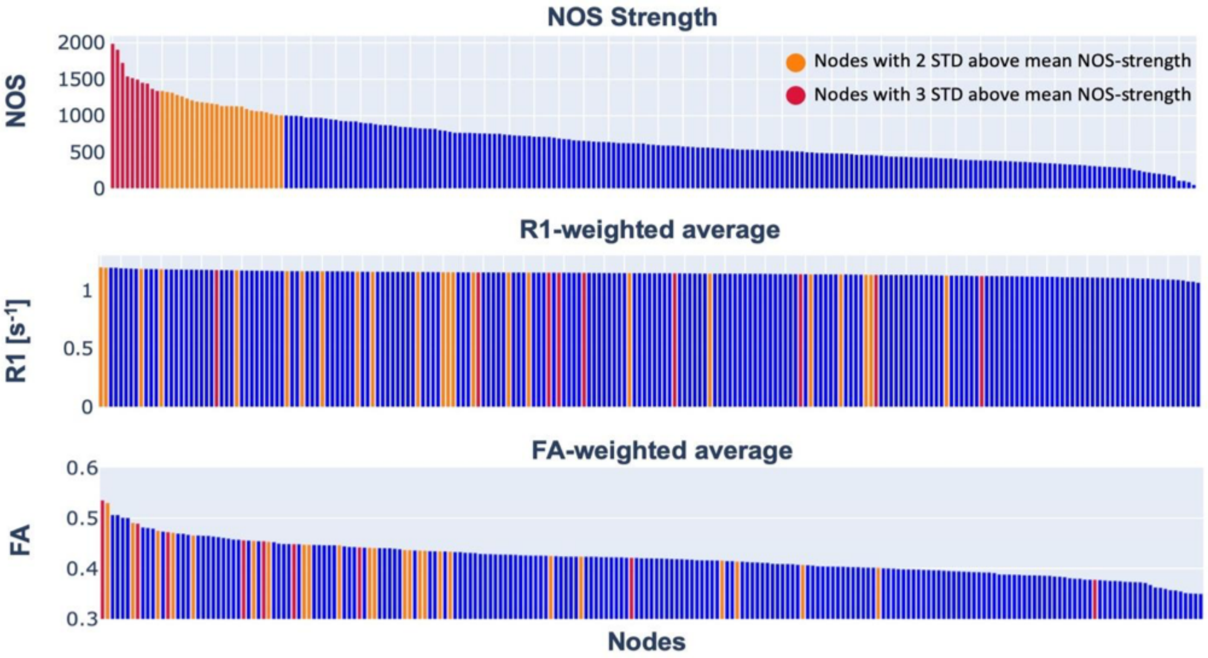

Figure A.2 Strength and weighted average distribution of the group NOS-, FA-, and R1-weighted connectome. In orange are highlighted the nodes that are two standard deviations above the mean NOS-strength, while in red are highlighted the nodes that are three standard deviations above the NOS-strength

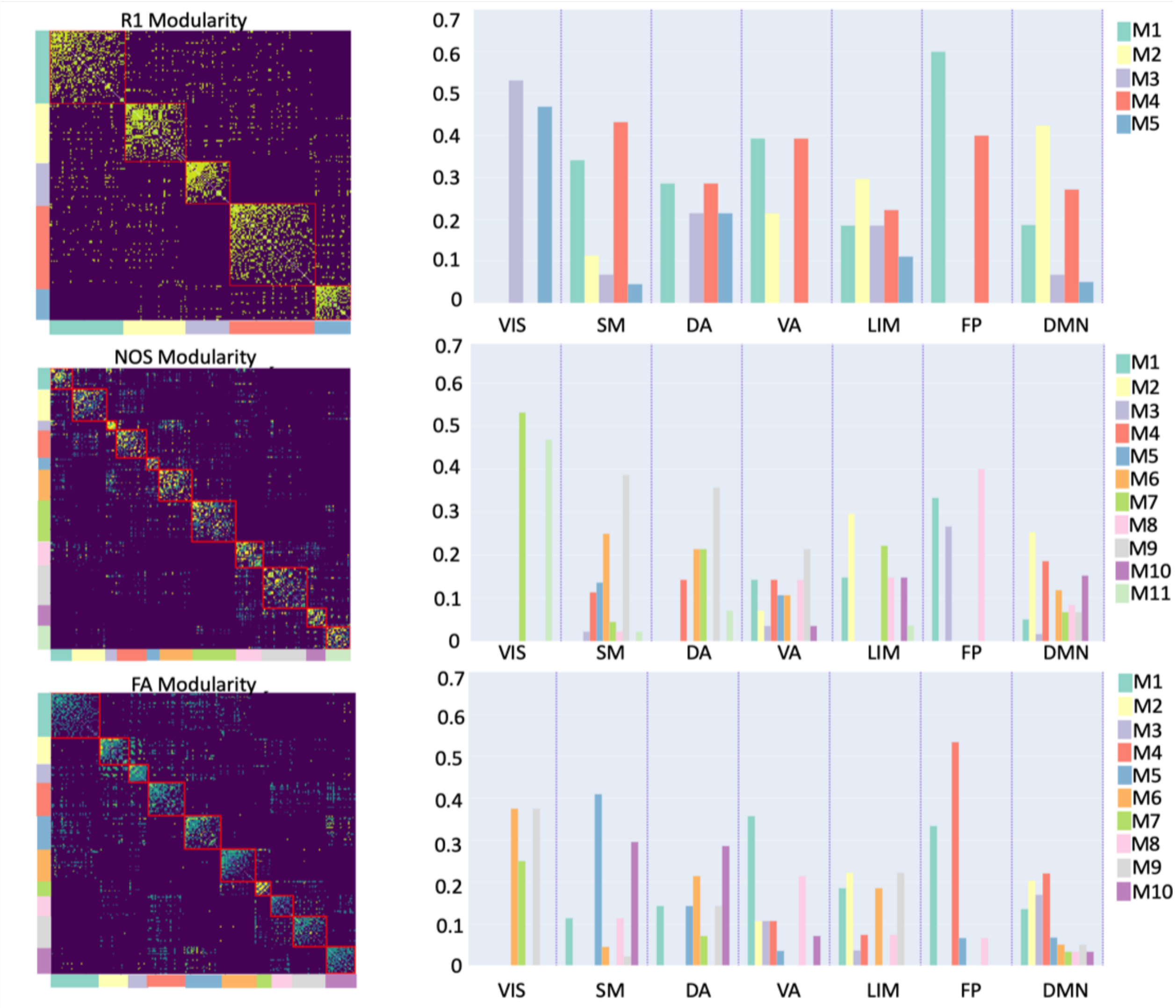

Figure A.3 Community structure of the R1-, FA-, and NOS-weighted connectomes. The bar plots represent the distributions of functional classes, given by Yeo et al., within the modules (denoted as M#) for the R1-, NOS-, and FA-weighted connectomes, respectively. Yeo's functional classes: SM (Somatomotor), VIS (Visual), VA (Ventral Attention), FP (Frontoparietal), LIM (Limbic), DA (Dorsal Attention), DMN (Default Mode Network)

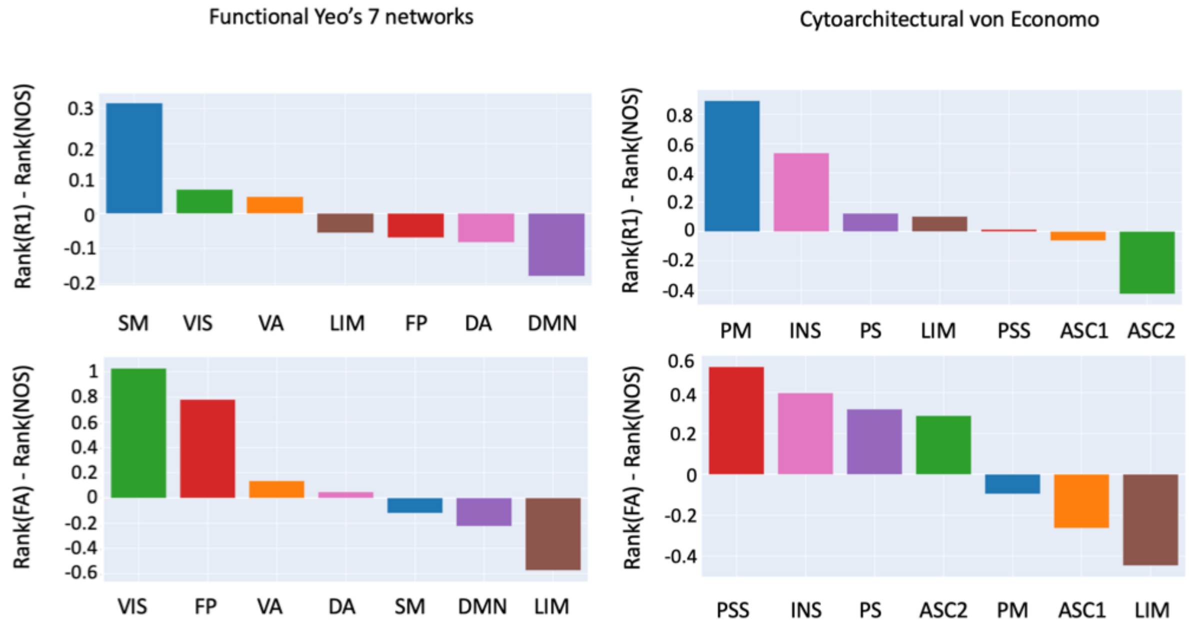

Figure A.4 Gradient of the nodes' rank. The rank for each node was calculated by its strength (for NOS) and weighted average (for R1 and FA). Then the nodes were grouped using a cytoarchitectonic parcellation and functional one. Yeo's functional classes: SM (Somatomotor), VIS (Visual), VA (Ventral Attention), FP (Frontoparietal), LIM (Limbic), DA (Dorsal Attention), DMN (Default Mode Network). Von Economo cytoarchitectonic classes: PM (primary motor), INS (insular), LIM (Limbic), PS (primary sensory), PSS (primary secondary sensory), ASC1 (association cortex), ASC2 (association cortex 2)

### A.2.2 Robustness of the analysis

To check the robustness of the analyses, we built a connectome that was constructed using a more conservative threshold. Basically, we considered two nodes to be connected if and only if they are at least 5 streamlines reconstructed between them. The order of the figures mimics the same order as the figures in the manuscript.

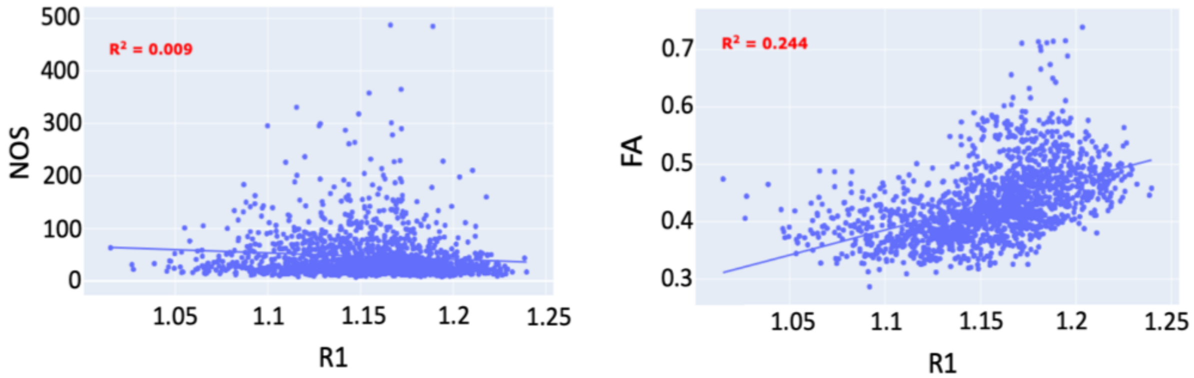

Figure A.5 Relationship between the connection weights in the R1-weighted and FA-weighted connectome (left) and R1-weighted and NOS-weighted (right)

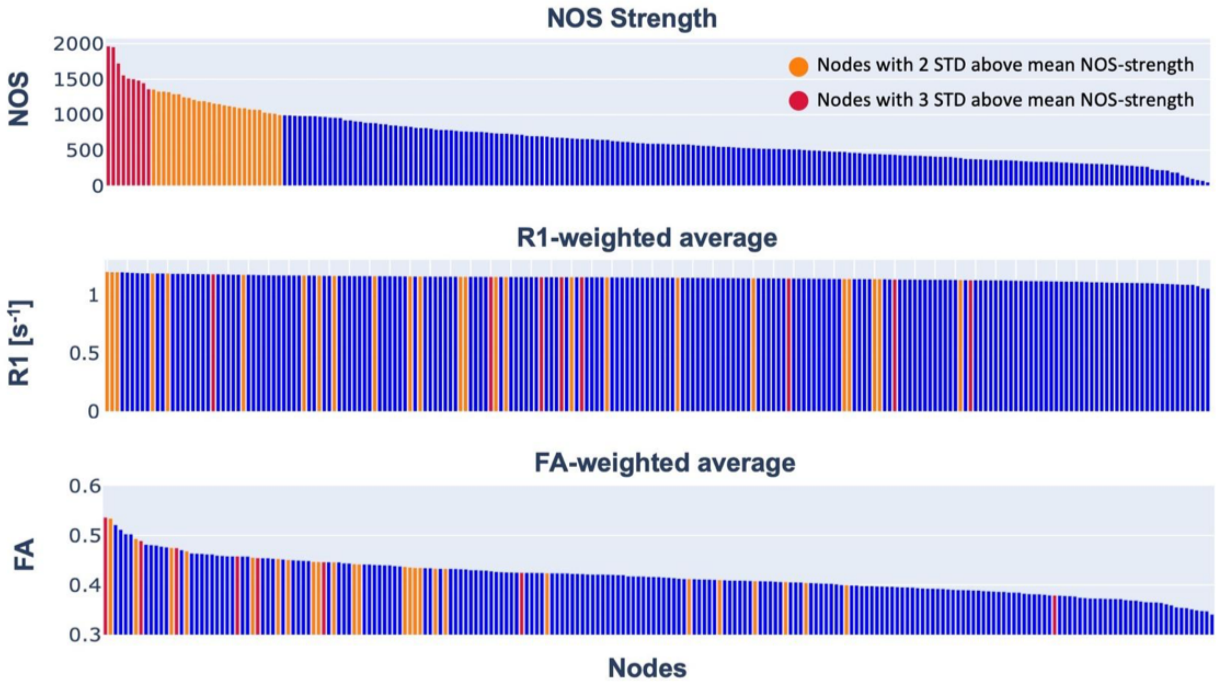

Figure A.6 Strength and weighted average distribution of the group NOS-, FA-, and R1-weighted connectome. In orange are highlighted the nodes that are two standard deviations above the mean NOS-strength, while in red are highlighted the nodes that are three standard deviations above the NOS-strength

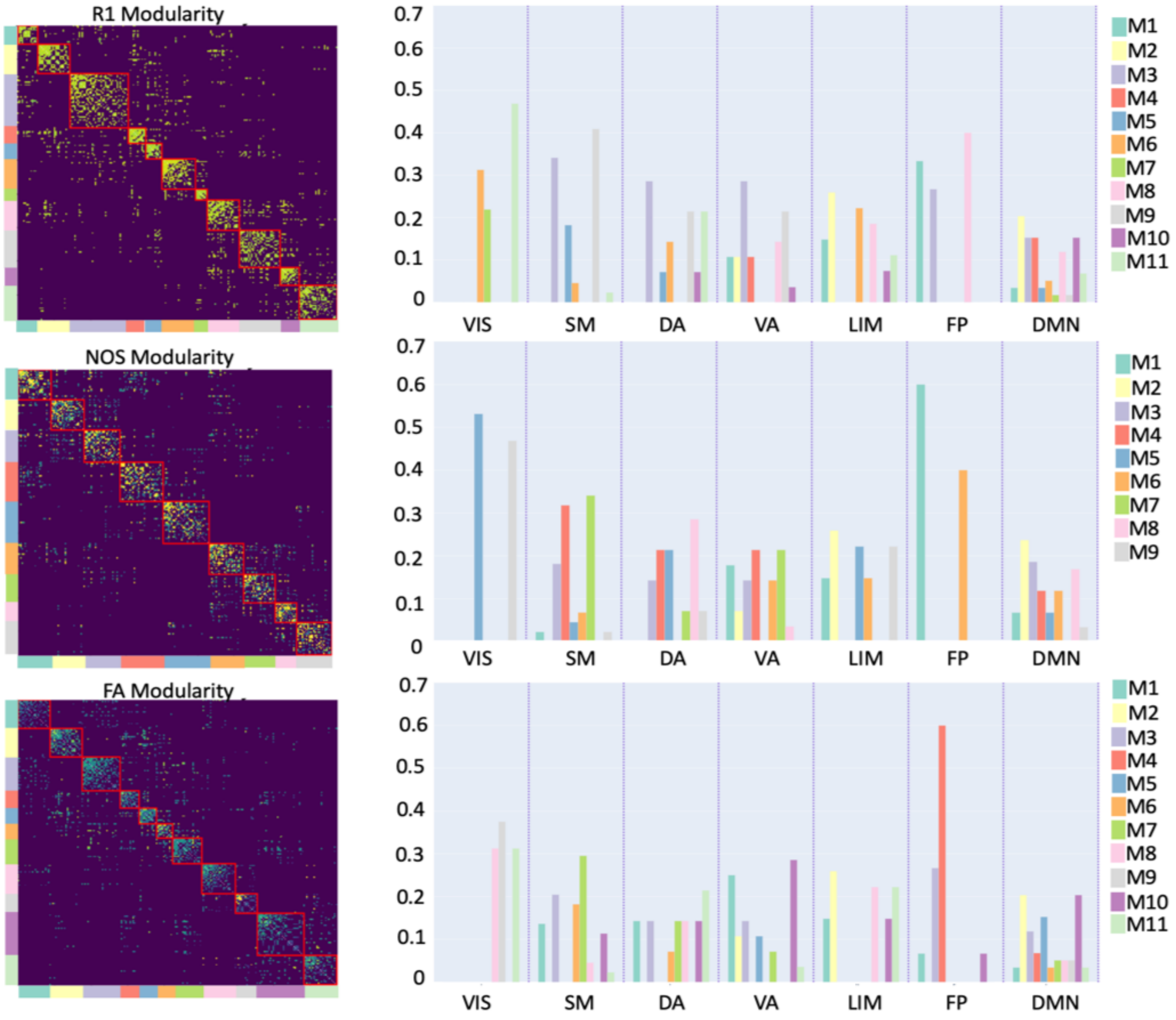

Figure A.7 Community structure of the R1-, FA-, and NOS-weighted connectomes. The selected resolution parameter was 2.8 for the R1-weighted connectome, 2.6 for the FA-weighted connectome, and 2 for the NOS-weighted connectome. The bar plots represent the distributions of functional classes, given by Yeo et al., within the modules (denoted as M#) for the R1-, NOS-, and FA-weighted connectomes, respectively. Yeo's functional classes: SM (Somatomotor), VIS (Visual), VA (Ventral Attention), FP (Frontoparietal), LIM (Limbic), DA (Dorsal Attention), DMN (Default Mode Network)

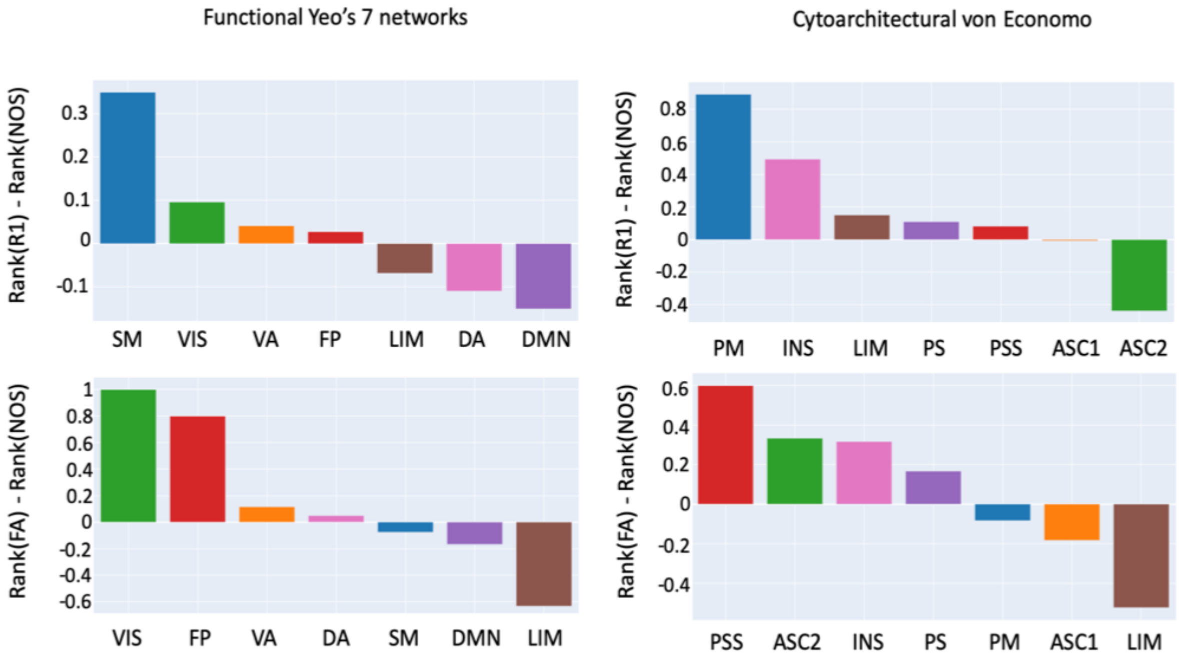

Figure A.8 Gradient of the nodes' rank. The rank for each node was calculated by its strength (for NOS) and weighted average (for R1 and FA). Then the nodes were grouped using a cytoarchitectonic parcellation and functional one. Yeo's functional classes: SM (Somatomotor), VIS (Visual), VA (Ventral Attention), FP (Frontoparietal), LIM (Limbic), DA (Dorsal Attention), DMN (Default Mode Network). Von Economo cytoarchitectonic classes: PM (primary motor), INS (insular), LIM (Limbic), PS (primary sensory), PSS (primary secondary sensory), ASC1 (association cortex), ASC2 (association cortex 2)

### A.2.3 Probabilistic tractography

To further check the robustness of the analyses, a Second-order Integration over Fiber Orientation Distributions (iFOD2) probabilistic tractography algorithm was employed to reconstruct the connectomes.

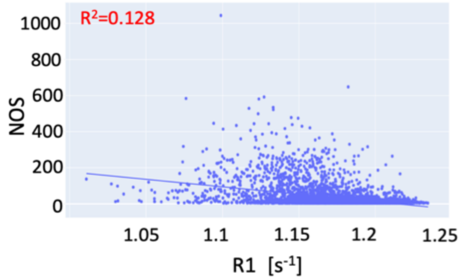

Figure A.9 Relationship between the connection weights in R1-weighted and NOS-weighted (right) reconstructed with probabilistic tractography

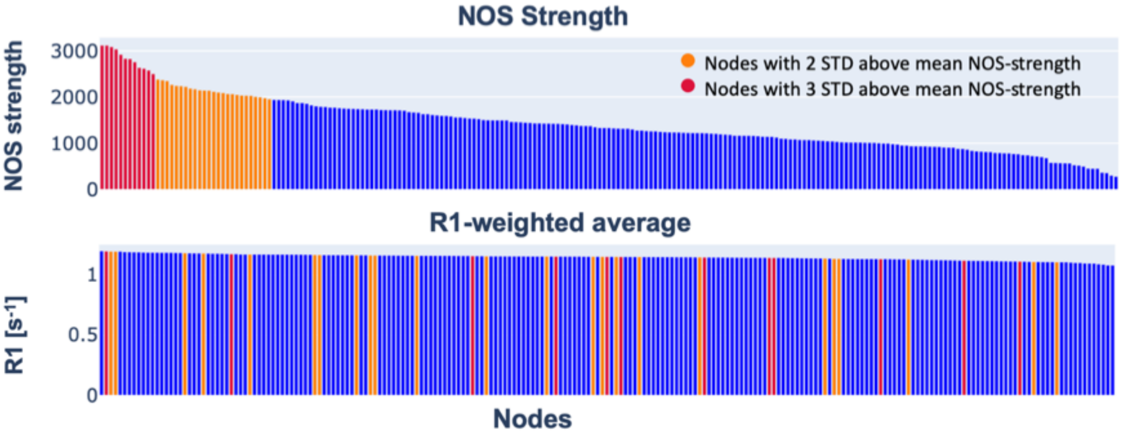

Figure A.10 Strength and weighted average distribution of the group NOS- and R1-weighted connectome reconstructed with probabilistic tractography. In orange are highlighted the nodes that are two standard deviations above the mean NOS-strength, while in red are highlighted the nodes that are three standard deviations above the NOS-strength

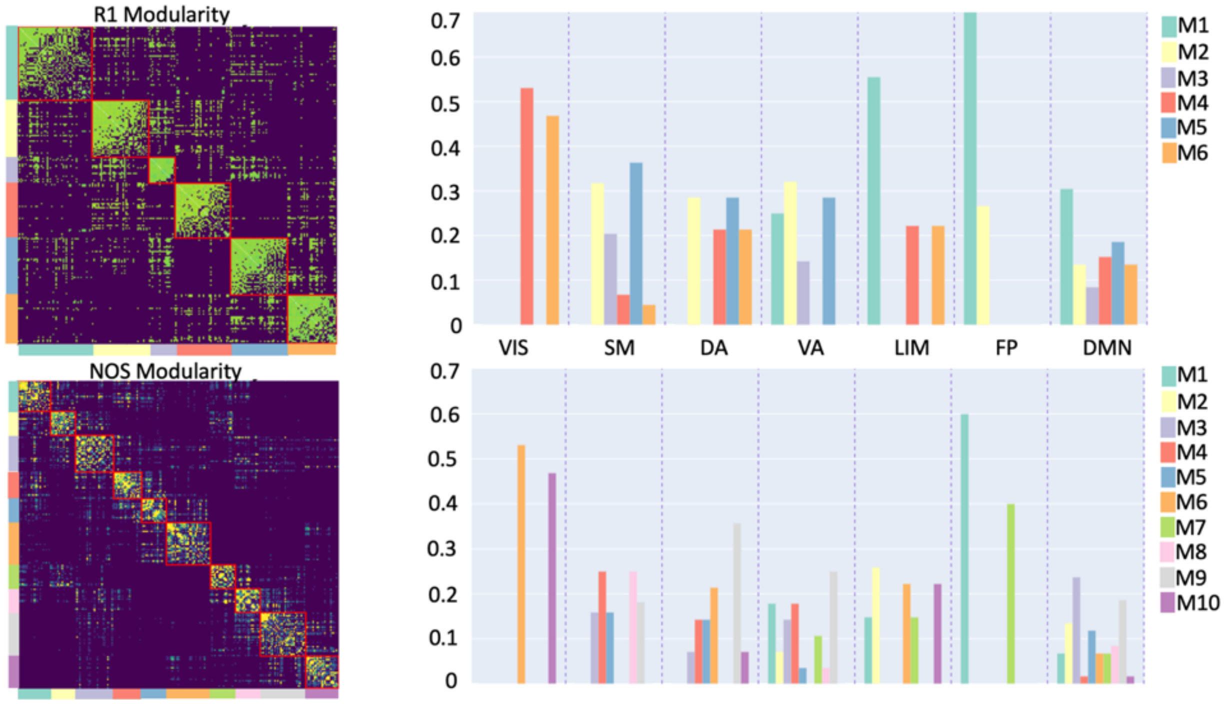

Figure A.11 Community structure of the R1-, and NOS-weighted connectomes reconstructed with probabilistic tractography. The selected resolution parameter was 1.6 for the R1-weighted connectome, and 1.8 for the NOS-weighted connectome. The bar plots represent the distributions of functional classes, given by Yeo et al., within the modules (denoted as M#) for the R1- and NOS-weighted connectomes, respectively. Yeo's functional classes: SM (Somatomotor), VIS (Visual), VA (Ventral Attention), FP (Frontoparietal), LIM (Limbic), DA (Dorsal Attention), DMN (Default Mode Network)

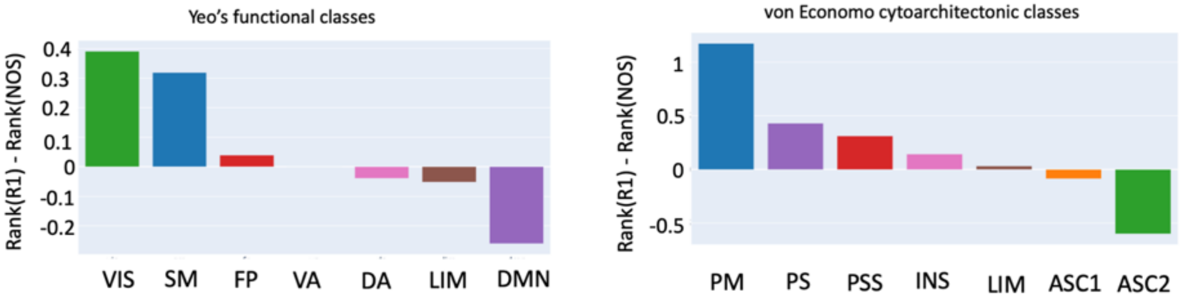

Figure A.12 Gradient of the nodes' rank. The rank for each node was calculated by its strength (for NOS) and weighted average (for R1). Then the nodes were grouped using a cytoarchitectonic parcellation and functional one. Yeo's functional classes: SM (Somatomotor), VIS (Visual), VA (Ventral Attention), FP (Frontoparietal), LIM (Limbic), DA (Dorsal Attention), DMN (Default Mode Network). Von Economo cytoarchitectonic classes: PM (primary motor), INS (insular), LIM (Limbic), PS (primary sensory), PSS (primary secondary sensory), ASC1 (association cortex), ASC2 (association cortex 2)

## A.3 Strength and weighted-average distributions

Table A.1 Strength and weighted average of the NOS-, R1-, and FA-weighted connectome.

| Node name | NOS strength | R1-weighted average | FA-weighted average |
|---|---|---|---|
| caudalmiddlefrontal_3_R | 1966 | 1.15455223 | 0.45481415 |
| superiorfrontal_8_L | 1955.5 | 1.15489756 | 0.5364118 |
| superiorfrontal_5_R | 1725.5 | 1.15657259 | 0.48931146 |
| lateraloccipital_4_R | 1558 | 1.17902009 | 0.37937757 |
| caudalmiddlefrontal_3_L | 1510.5 | 1.1425173 | 0.45794132 |
| precentral_6_R | 1502 | 1.12808163 | 0.47504907 |
| lateraloccipital_1_L | 1484.5 | 1.15372432 | 0.4250611 |
| postcentral_5_R | 1447 | 1.13491831 | 0.44638249 |
| caudalmiddlefrontal_1_L | 1360.5 | 1.15249975 | 0.44708179 |
| superiorfrontal_4_R | 1357.5 | 1.14975925 | 0.44246636 |
| lateraloccipital_2_R | 1330 | 1.18572172 | 0.40010313 |
| superiorparietal_7_R | 1329.5 | 1.18490026 | 0.46868563 |
| superiorfrontal_6_L | 1321 | 1.13927463 | 0.43705957 |
| superiorfrontal_3_R | 1292.5 | 1.19858478 | 0.45097488 |
| inferiorparietal_6_R | 1292.5 | 1.15621096 | 0.42422677 |
| parsopercularis_2_L | 1249.5 | 1.15720478 | 0.44614924 |
| paracentral_2_L | 1241 | 1.13771093 | 0.44208708 |
| rostralmiddlefrontal_2_R | 1214.5 | 1.16733895 | 0.43347641 |
| superiorfrontal_6_R | 1193.5 | 1.15941077 | 0.53443044 |
| precentral_4_R | 1193.5 | 1.13806138 | 0.44677296 |
| superiorparietal_1_R | 1178.5 | 1.16853382 | 0.43314363 |
| superiorfrontal_7_L | 1159 | 1.15768024 | 0.49319574 |
| rostralmiddlefrontal_1_R | 1151 | 1.14500352 | 0.41263682 |
| cuneus_1_L | 1135.5 | 1.13002028 | 0.41040971 |
| precentral_7_L | 1124 | 1.15641855 | 0.43493235 |
| inferiorparietal_4_L | 1111 | 1.16574541 | 0.43595524 |
| lateraloccipital_4_L | 1095 | 1.16091219 | 0.40645647 |
| middletemporal_1_L | 1094 | 1.17478661 | 0.45568292 |

| | | | |
|---|---|---|---|
| middletemporal_1_R | 1077.5 | 1.19980463 | 0.43495825 |
| superiorfrontal_3_L | 1075 | 1.16314845 | 0.45295976 |
| superiorfrontal_9_L | 1071.5 | 1.13961489 | 0.47527627 |
| rostralmiddlefrontal_3_R | 1032 | 1.15389897 | 0.40840144 |
| lateraloccipital_5_R | 1023.5 | 1.19707436 | 0.40468686 |
| inferiorparietal_1_L | 1017 | 1.1632152 | 0.42050431 |
| precentral_5_R | 998 | 1.12466084 | 0.44015975 |
| superiorparietal_2_L | 995.5 | 1.1501535 | 0.42405723 |
| parstriangularis_1_L | 994 | 1.15047862 | 0.41179135 |
| inferiorparietal_5_L | 988 | 1.16492729 | 0.43319758 |
| isthmuscingulate_1_L | 985.5 | 1.15111918 | 0.46342115 |
| superiorparietal_7_L | 983.5 | 1.15835931 | 0.46232216 |
| precentral_3_L | 982.5 | 1.10873801 | 0.45172339 |
| superiorfrontal_7_R | 981 | 1.14491754 | 0.50266414 |
| supramarginal_5_L | 975.5 | 1.15672519 | 0.42411832 |
| parsopercularis_2_R | 971 | 1.15793737 | 0.44405594 |
| postcentral_3_R | 961.5 | 1.14229538 | 0.41660898 |
| rostralmiddlefrontal_2_L | 960 | 1.15095653 | 0.42127552 |
| superiorfrontal_2_R | 957 | 1.15379185 | 0.45018773 |
| paracentral_2_R | 923.5 | 1.13875271 | 0.4811363 |
| superiorfrontal_1_R | 923 | 1.15586281 | 0.44184927 |
| rostralmiddlefrontal_4 _L | 908.5 | 1.16348021 | 0.39311237 |
| superiorfrontal_5_L | 905 | 1.15523623 | 0.45805608 |
| superiorparietal_5_L | 889.5 | 1.16252581 | 0.43204665 |
| superiorfrontal_8_R | 887.5 | 1.14141001 | 0.44379638 |
| caudalmiddlefrontal_1_R | 883 | 1.14609962 | 0.44162341 |
| pericalcarine_1_L | 871 | 1.11404583 | 0.39693474 |
| superiorparietal_4_R | 866.5 | 1.18072143 | 0.42485591 |
| lateraloccipital_1_R | 852 | 1.15844078 | 0.42304646 |
| lateraloccipital_5_L | 849 | 1.13991544 | 0.37970863 |
| superiorfrontal_1_L | 839.5 | 1.17374917 | 0.45768595 |
| supramarginal_4_L | 839 | 1.16224559 | 0.4302635 |
| inferiorparietal_2_L | 832 | 1.16368641 | 0.42498126 |
| inferiortemporal_4_L | 818.5 | 1.15592484 | 0.4324534 |

| | | | |
|---|---|---|---|
| precentral_4_L | 815.5 | 1.10742643 | 0.43777023 |
| cuneus_2_R | 815 | 1.15082102 | 0.44632162 |
| rostralmiddlefrontal_5 _L | 807.5 | 1.17197196 | 0.39257267 |
| rostralmiddlefrontal_1_L | 792.5 | 1.16495753 | 0.42939455 |
| insula_3_L | 790 | 1.10283158 | 0.4169084 |
| isthmuscingulate_1_R | 788.5 | 1.16147066 | 0.45335847 |
| inferiortemporal_4_R | 784.5 | 1.19627428 | 0.421529 |
| parstriangularis_2_R | 776 | 1.15943345 | 0.41145212 |
| precentral_8_L | 768 | 1.13441633 | 0.42563866 |
| superiortemporal_5_R | 767 | 1.14868755 | 0.44976691 |
| superiorparietal_4_L | 763 | 1.16261628 | 0.44885281 |
| inferiorparietal_2_R | 761 | 1.18345119 | 0.41581574 |
| insula_2_R | 760.5 | 1.11639998 | 0.42300816 |
| precentral_2_R | 754.5 | 1.16312108 | 0.44005198 |
| rostralanteriorcingulate_1_L | 745.5 | 1.1462204 | 0.42977588 |
| supramarginal_2_R | 739.5 | 1.19077522 | 0.4249869 |
| precuneus_5_R | 737 | 1.16825677 | 0.46423564 |
| inferiorparietal_1_R | 736.5 | 1.18330042 | 0.43022905 |
| inferiorparietal_3_R | 730.5 | 1.19412587 | 0.43864252 |
| supramarginal_3_R | 724 | 1.17614717 | 0.40946224 |
| posteriorcingulate_1_L | 721.5 | 1.14034405 | 0.44099281 |
| medialorbitofrontal_2_L | 704.5 | 1.12784405 | 0.41264181 |
| precentral_5_L | 699.5 | 1.18694673 | 0.45829026 |
| inferiorparietal_4_R | 699.5 | 1.13859579 | 0.42150329 |
| supramarginal_1_R | 697 | 1.16800185 | 0.42261709 |
| parsopercularis_1_L | 695 | 1.15456888 | 0.4239968 |
| precentral_2_L | 680.5 | 1.11527065 | 0.45777004 |
| rostralanteriorcingulate_1_R | 680 | 1.13511194 | 0.4101604 |
| superiorparietal_3_L | 678 | 1.14502659 | 0.40302768 |
| paracentral_1_L | 674 | 1.13882637 | 0.48018474 |
| insula_3_R | 668.5 | 1.08889984 | 0.39622527 |
| inferiorparietal_5_R | 663 | 1.17867113 | 0.39738851 |
| supramarginal_2_L | 660.5 | 1.15205014 | 0.40175146 |
| rostralmiddlefrontal_4 _R | 660 | 1.15286239 | 0.3900672 |

| | | | |
|---|---|---|---|
| superiorfrontal_2_L | 658.5 | 1.1514495 | 0.44912618 |
| postcentral_5_L | 649.5 | 1.1855542 | 0.38959689 |
| fusiform_3_R | 649.5 | 1.1262997 | 0.38848968 |
| caudalmiddlefrontal_2_L | 647.5 | 1.15461277 | 0.42479 |
| lingual_3_R | 633.5 | 1.15286475 | 0.39020298 |
| middletemporal_3_L | 627 | 1.15709588 | 0.42177641 |
| paracentral_3_R | 619.5 | 1.14703501 | 0.41685414 |
| superiortemporal_3_L | 618.5 | 1.14588912 | 0.39757772 |
| superiorparietal_5_R | 612.5 | 1.18296281 | 0.42387247 |
| precentral_3_R | 604.5 | 1.15056573 | 0.42631798 |
| lateralorbitofrontal_1_L | 602.5 | 1.1397014 | 0.36462349 |
| rostralmiddlefrontal_3_L | 595 | 1.16592398 | 0.40353479 |
| parsopercularis_1_R | 593.5 | 1.15170139 | 0.42685304 |
| lingual_1_L | 593.5 | 1.12772303 | 0.39827912 |
| lateralorbitofrontal_2_R | 592 | 1.11875655 | 0.38789434 |
| medialorbitofrontal_1_R | 590 | 1.14103453 | 0.42591573 |
| rostralmiddlefrontal_5 _R | 586 | 1.15616708 | 0.39314514 |
| precuneus_2_L | 585 | 1.15801093 | 0.44607199 |
| lateraloccipital_3_R | 585 | 1.15698507 | 0.35949723 |
| postcentral_4_L | 584 | 1.10408324 | 0.41106983 |
| postcentral_3_L | 575.5 | 1.11841811 | 0.40030039 |
| precentral_1_L | 569.5 | 1.12317379 | 0.48183509 |
| posteriorcingulate_2_R | 564 | 1.15623144 | 0.42528901 |
| superiorfrontal_4_L | 563 | 1.15482501 | 0.45464763 |
| caudalanteriorcingulate_1_R | 562 | 1.13303653 | 0.42056307 |
| fusiform_4_L | 551.5 | 1.13483781 | 0.43284576 |
| caudalanteriorcingulate_1_L | 551.5 | 1.12405917 | 0.42149176 |
| fusiform_2_L | 551 | 1.14184332 | 0.38525191 |
| pericalcarine_1_R | 544 | 1.13457765 | 0.38293242 |
| fusiform_2_R | 537.5 | 1.17439895 | 0.37263486 |
| precentral_1_R | 534 | 1.14323869 | 0.42110269 |
| supramarginal_4_R | 531 | 1.14736172 | 0.36603971 |
| lateraloccipital_3_L | 529 | 1.14020491 | 0.3774293 |
| superiorparietal_3_R | 526 | 1.18642675 | 0.43409549 |

| | | | |
|---|---|---|---|
| precuneus_4_R | 524 | 1.17751237 | 0.4590447 |
| lingual_1_R | 521.5 | 1.15579823 | 0.37019401 |
| postcentral_7_L | 520.5 | 1.12540779 | 0.37327419 |
| fusiform_1_R | 520 | 1.1691619 | 0.34769522 |
| postcentral_1_L | 517.5 | 1.141686 | 0.47087571 |
| fusiform_1_L | 515.5 | 1.13122178 | 0.34963292 |
| superiorparietal_6_R | 513.5 | 1.1832551 | 0.40556838 |
| parsorbitalis_1_R | 512.5 | 1.14404038 | 0.38672418 |
| precuneus_3_L | 506.5 | 1.16370884 | 0.46374493 |
| superiortemporal_5_L | 501.5 | 1.11135013 | 0.4596908 |
| fusiform_4_R | 500 | 1.16894616 | 0.40645676 |
| middletemporal_2_L | 495.5 | 1.17035314 | 0.45461105 |
| middletemporal_4_R | 489 | 1.16885257 | 0.41759972 |
| rostralmiddlefrontal_6_L | 485 | 1.17903179 | 0.40397749 |
| cuneus_1_R | 481.5 | 1.15410335 | 0.38543692 |
| inferiorparietal_3_L | 481 | 1.14867184 | 0.40587203 |
| lateralorbitofrontal_2_L | 478 | 1.12837932 | 0.38516694 |
| medialorbitofrontal_1_L | 468 | 1.15228688 | 0.42814361 |
| superiorparietal_1_L | 466.5 | 1.16181001 | 0.51192899 |
| inferiortemporal_3_L | 463.5 | 1.12694042 | 0.41518689 |
| paracentral_1_R | 452 | 1.14627292 | 0.46229125 |
| rostralmiddlefrontal_6_R | 451 | 1.15557603 | 0.38230397 |
| superiortemporal_1_L | 450.5 | 1.15113884 | 0.40836503 |
| precuneus_1_L | 448.5 | 1.16877606 | 0.50295654 |
| precuneus_5_L | 442.5 | 1.13045906 | 0.39570302 |
| postcentral_2_R | 442 | 1.14496349 | 0.39419567 |
| lateralorbitofrontal_4_L | 439 | 1.16620957 | 0.41169347 |
| superiortemporal_3_R | 432 | 1.15778882 | 0.38670591 |
| superiorparietal_6_L | 429.5 | 1.13243551 | 0.38101755 |
| lateraloccipital_2_L | 426 | 1.11668654 | 0.37404023 |
| posteriorcingulate_2_L | 425 | 1.12638331 | 0.39814242 |
| posteriorcingulate_1_R | 424.5 | 1.13274037 | 0.41780136 |
| lingual_2_R | 418 | 1.14083757 | 0.34839059 |
| fusiform_3_L | 417 | 1.13187888 | 0.37801114 |

| | | | |
|---|---|---|---|
| inferiortemporal_1_R | 412.5 | 1.15713411 | 0.40578383 |
| supramarginal_3_L | 410.5 | 1.15168448 | 0.4131758 |
| superiortemporal_4_L | 410.5 | 1.1323127 | 0.4079409 |
| superiortemporal_2_R | 407.5 | 1.17260683 | 0.38742364 |
| superiorparietal_2_R | 398 | 1.18109749 | 0.52135756 |
| insula_1_L | 393 | 1.10346004 | 0.3695119 |
| postcentral_1_R | 379 | 1.14983243 | 0.43441182 |
| middletemporal_4_L | 379 | 1.13664358 | 0.37230518 |
| bankssts_1_R | 375 | 1.17994353 | 0.392723 |
| precentral_6_L | 373.5 | 1.10567908 | 0.37237818 |
| lingual_2_L | 369.5 | 1.12052779 | 0.36558653 |
| caudalmiddlefrontal_2_R | 364 | 1.14904611 | 0.4179389 |
| insula_1_R | 363.5 | 1.13455426 | 0.37337997 |
| precuneus_3_R | 363 | 1.16865013 | 0.40939818 |
| precuneus_4_L | 362.5 | 1.15330462 | 0.40953028 |
| superiortemporal_1_R | 360.5 | 1.16366432 | 0.38950814 |
| lateralorbitofrontal_3_L | 357.5 | 1.14780076 | 0.3412609 |
| lingual_4_L | 351 | 1.11990501 | 0.35407521 |
| precuneus_2_R | 346 | 1.16974181 | 0.4330711 |
| supramarginal_1_L | 342.5 | 1.12020763 | 0.354774 |
| insula_2_L | 341 | 1.10332633 | 0.41775601 |
| frontalpole_1_R | 340.5 | 1.17891993 | 0.47641935 |
| parsorbitalis_1_L | 340 | 1.15781349 | 0.37857484 |
| bankssts_1_L | 338 | 1.14517744 | 0.39097622 |
| middletemporal_2_R | 336.5 | 1.18898979 | 0.41242934 |
| middletemporal_3_R | 332.5 | 1.17653929 | 0.40450314 |
| inferiortemporal_2_L | 332 | 1.11673579 | 0.40807257 |
| medialorbitofrontal_2_R | 325 | 1.12000391 | 0.40876957 |
| postcentral_6_L | 319 | 1.12089407 | 0.38173278 |
| inferiortemporal_1_L | 316.5 | 1.1110917 | 0.3982293 |
| lingual_3_L | 314.5 | 1.10730392 | 0.37253977 |
| superiortemporal_2_L | 311.5 | 1.14632003 | 0.39161942 |
| precuneus_1_R | 309.5 | 1.14464919 | 0.39955046 |
| pericalcarine_2_R | 309 | 1.10683551 | 0.36736579 |

| | | | |
|---|---|---|---|
| bankssts_2_L | 303.5 | 1.15361921 | 0.41426406 |
| inferiortemporal_2_R | 303 | 1.14625646 | 0.39568039 |
| postcentral_2_L | 297.5 | 1.09886111 | 0.44066292 |
| lateralorbitofrontal_1_R | 291 | 1.08972515 | 0.39367714 |
| lateralorbitofrontal_3_R | 285 | 1.11050945 | 0.37323283 |
| parahippocampal_1_R | 284.5 | 1.13200874 | 0.37900699 |
| transversetemporal_1_L | 276 | 1.1177173 | 0.3515679 |
| parahippocampal_1_L | 274.5 | 1.09368955 | 0.3970375 |
| frontalpole_1_L | 269.5 | 1.18547491 | 0.47789238 |
| inferiortemporal_3_R | 235 | 1.15869384 | 0.39527496 |
| lateralorbitofrontal_4_R | 224.5 | 1.12652473 | 0.39936488 |
| postcentral_4_R | 221.5 | 1.14408016 | 0.39030834 |
| transversetemporal_1_R | 216 | 1.13834961 | 0.3555768 |
| parstriangularis_1_R | 190 | 1.09673742 | 0.38169027 |
| insula_4_L | 185.5 | 1.07750943 | 0.3689944 |
| medialorbitofrontal_3_R | 147.5 | 1.08856092 | 0.3654355 |
| temporalpole_1_L | 122 | 1.09801082 | 0.40922319 |
| superiortemporal_4_R | 101 | 1.055135 | 0.374883 |
| entorhinal_1_L | 82.5 | 1.05744297 | 0.40704466 |
| entorhinal_1_R | 71.5 | 1.09199238 | 0.40333935 |
| temporalpole_1_R | 49 | 1.10473714 | 0.361872 |

# APPENDIX B SUPPLEMENTARY MATERIALS FOR ARTICLE 2

## B.1 PLS Analysis

The partial least squares (PLS) analysis is a multivariate statistical technique that tries to identify a linear combination of connections that maximally covary with an experimental desing or behavioral/clinical scores. For each pair (HC vs. PD ; HC vs. PDnonRBD; HC vs. PDRBD), the two sets of variables were defined as $\mathbf{X_{nxp}}$ and $\mathbf{Y_{nx1}}$. $\mathbf{X_{nxp}}$ corresponds to the non-zero connections shared between the groups, while $\mathbf{Y_{nx1}}$ is a matrix that corresponds to the experiment design, where n corresponds to number of subjects, *p* corresponds to number of unique connections. The resulting sizes for the two sets of variables for each pair of groups was HC vs. PD: $\mathbf{X_{116x1360}}$ and $\mathbf{Y_{116x1}}$; HC vs PDnonRBD: $\mathbf{X_{81x1360}}$ and $\mathbf{Y_{81x1}}$; HC vs PDRBD: $\mathbf{X_{57x1349}}$ and $\mathbf{Y_{57x1}}$. Because the connectivity matrices are symmetric, we extracted the elements of the upper triangle that correspond to unique non-zero connections that are shared between the groups. We then stacked the unique connections on top of each other, i.e., each row of $\mathbf{X}$ corresponds to the unique connections of the subjects (both HC and PD group, HC and PDnonRBD, and HC and PDRBD), while $\mathbf{Y}$ contains the experimental design. For each pair of groups, a mean-centered matrix $\mathbf{M^{dev}_{2xp}}$, was then computed from X and Y, by removing the grand mean from $\mathbf{X}$ for each group as defined in $\mathbf{Y}$, reflecting the covariation of each connection with the experimental design. For the behavioural PLS, we aimed to identify the connections that maximally covaried with the MDS-UPDRS III score. The only difference from the mean-centing PLS is that the $\mathbf{Y_{nx1}}$ contains the MDS-UPDRS III scores for each subject and the $\mathbf{M^{dev}_{2xp}} = \mathbf{Y'X}$. Afterwards, a singular value decomposition (SVD) was applied to the $\mathbf{M^{dev}_{2xp}}$ matrix which resulted in a set of 2 mutually orthogonal latent variables (LVs):

$$SVD(\mathbf{M^{dev}_{2xp}}) = \mathbf{U_{px2}\Delta_{2x2}V'_{2x2}} \tag{B.1}$$

where $\mathbf{U}$ and $\mathbf{V}$ are the left and right singular vectors, and $\mathbf{\Delta}$ is a diagonal matrix with singular values along the diagonal. Each latent variable is composed of left and right singular vectors and a singular value. For example the first latent variable is composed of the left and right singular vectors (first column of $\mathbf{U}$ and $\mathbf{V}$) reflecting the contribution of and the singular value (first element of the diagonal matrix $\mathbf{\Delta}$). In our case the left singular vector provides the contribution of each connection to its respective LV, while the right singular vector reflects the contribution of the design variable to its respective LV and can be seen as a contrast. Furthermore, the singular value reflects the covariance between the two sets.

## B.2 Mean-centered PLS

Table B.1 Multivariate connectivity pattern from the mean-centered PLS analysis between HC and PD Group. The reported labels correspond to the labels as defined in the Desikan-Killiany atlas.

| Node name | Node name |
|---|---|
| SubstantiaNigra | postcentral_l |
| SubstantiaNigra | precentral_l |
| SubstantiaNigra | precuneus_l |
| SubstantiaNigra | superiorfrontal_l |
| SubstantiaNigra | superiorparietal_l |
| SubstantiaNigra | Caudate |
| SubstantiaNigra | precentral_r |
| SubstantiaNigra | precuneus_r |
| SubstantiaNigra | superiorfrontal_r |
| SubstantiaNigra | Midbrain |
| SubstantiaNigra | Pons |
| SubstantiaNigra | Medulla |
| ThalamusProper | LocusCoeruleus |
| Hippocampus | Amygdala |
| LocusCoeruleus | Midbrain |

Table B.2 Multivariate connectivity pattern from the mean-centered PLS analysis between HC and PDnon-RBD group. The reported labels correspond to the labels as defined in the Desikan-Killiany atlas.

| Node name | Node name |
|---|---|
| SubstantiaNigra | postcentral_l |
| SubstantiaNigra | precentral_l |
| SubstantiaNigra | precuneus_l |
| SubstantiaNigra | superiorfrontal_l |

| | |
|---|---|
| SubstantiaNigra | superiorparietal_l |
| SubstantiaNigra | Caudate |
| SubstantiaNigra | postcentral_r |
| SubstantiaNigra | precentral_r |
| SubstantiaNigra | precuneus_r |
| SubstantiaNigra | superiorfrontal_r |
| SubstantiaNigra | Midbrain |
| SubstantiaNigra | Pons |
| SubstantiaNigra | Medulla |
| ThalamusProper | Amygdala |
| ThalamusProper | LocusCoeruleus |
| ThalamusProper | NucleusBasalis |
| Hippocampus | Amygdala |
| LocusCoeruleus | Midbrain |
| LocusCoeruleus | Pallidum |

Table B.3 Multivariate connectivity pattern from the mean-centered PLS analysis between HC and PDRBD group. The reported labels correspond to the labels as defined in the Desikan-Killiany atlas.

| Node name | Node name |
|---|---|
| SubstantiaNigra | precuneus_l |
| SubstantiaNigra | isthmuscingulate_l |
| SubstantiaNigra | lateraloccipital_l |
| SubstantiaNigra | superiorfrontal_l |
| SubstantiaNigra | superiorparietal_l |
| SubstantiaNigra | Caudate |
| SubstantiaNigra | postcentral_r |
| SubstantiaNigra | precentral_r |
| SubstantiaNigra | precuneus_r |
| SubstantiaNigra | superiorfrontal_r |
| SubstantiaNigra | Midbrain |
| SubstantiaNigra | Pons |
| SubstantiaNigra | Medulla |

| | |
|---|---|
| ThalamusProper | NucleusBasalis |
| ThalamusProper | Amygdala |
| Hippocampus | postcentral_l |
| Hippocampus | Amygdala |
| Putamen | AccumbensArea |
| Midbrain | parsopercularis_r |